# Electronic Phenomena In Graphene Based Van Der Waals Heterostructures

Thompson, Joshua

*Award date:*
2019

*Awarding institution:*
University of Bath

# Electronic phenomena in graphene-based van der Waals heterostructures

**Joshua John Paul Thompson**

A thesis presented for the degree of
Doctor of Philosophy

University of Bath

Department of Physics

July 2019

*To Jeanne Thompson*

## Declaration of any previous submission of the work

As a result of collaborative work, some of the material presented here for examination for the award of a higher degree by D. J. Leech for the degree of Doctor of Philosophy. In particular, this entails some of the results presented in Chapters 6 and 7. The level of contribution and details of this previous submission are presented at the start of each chapter.

## Declaration of authorship

I am the author of this thesis, however some of the work presented in Chapters 4-7 was done in collaboration with others. We provide details on the relative contributions at the start of each chapter. Furthermore, parts of this thesis (including figures) have been published in original publications:

- *Negative Differential Resistance in van der Waals Heterostructures Due to Moiré-Induced Spectral Reconstruction*, D.J Leech, **J.J.P.Thompson**, M.Mucha-Kruczyński, Phys. Rev. Appl. **10**, 034014 (2018) [1].
- *Valley-polarized tunnelling currents in bilayer graphene tunnelling transistors*, **J.J.P.Thompson**, D.J. Leech, M.Mucha-Kruczyński, Phys. Rev. B **99**, 085420 (2019) [2].

These are included with permission from the American Physical Society.

**Abstract**

In this thesis, we model the electronic and optical properties of stacked structures of two-dimensional materials involving graphene. In particular, we discuss how the interplay between the type and alignment of these stacked two-dimensional crystals affects the observed physical properties.

Tuning the misalignment between two graphene layers leads to stark modification to the resulting electronic band structure. By employing electronic Raman scattering, we show that it is theoretically possible to accurately determine the twist angle in twisted bilayer graphene samples close to the magic-angle.

We propose a new parameterisation for the interlayer coupling between twisted graphene layers, and demonstrate that twisted trilayer graphene is the simplest system in which the coupling in aligned and misaligned graphene bilayer can be probed. By comparison to experimental photoemission data, we demonstrate the validity and self-consistency of our model.

We discuss the tunnelling current across two van der Waals tunnelling transistors. In the first, one or both of the electrodes are made of two crystals forming a moiré superlattice at their interface. We investigate structures containing either aligned graphene/hexagonal boron nitride heterostructure, twisted bilayer graphene or aligned graphene on $\alpha - In_2Te_2$ and show negative differential resistance is possible in such transistors. In the second case we propose a tunnelling junction in an external magnetic field perpendicular to the layers, where the source and drain electrode are comprised of bilayer and monolayer graphene respectively. We show that, due to the effective difference in tunnelling barrier width for electrons on the two layers of bilayer graphene and the valley-dependent wave function distribution between these layers, the valley polarisation of the current can be electrically tuned. We demonstrate that strong valley polarisation can be obtained in the clean limit, where strong-momentum conserving tunnelling dominates, and in lower quality devices where this constraint is lifted.

# Acknowledgements

First, I'd like to thank my supervisor, Marcin, for his guidance, patience and humour over the past four years. The passion he has for his work is truly an inspiration and it has been a privilege to be a member of his research group. Furthermore, through working in this research group, I have made hopefully lifelong friends. To Damien, I thank you for being a great friend and mentor, and working with you has been a pleasure. To Aitor, never change man, your bizarre sense of humour and passion for physics have made the past 3 years living and working with you a memorable experience.

Most importantly, I have met the love of my life in this research group. To Surani, you are an amazing person with a personality that is truly one of a kind. You have made the last 18 months the happiest of my life, and I know that this is just the beginning of something incredible.

I'd also like to thank other members of 3W 4.5 who have made the past four years fantastic. Thanks Ed and Tom for surviving sitting next to me for three years, thanks Tsimbae for being an amazing friend and thanks Matt and Matt-indifferent for putting up with Surani and I rambling on.

Finally, I'd like to thank my family. To Thomas and Harvey, it is growing up with you guys that made me the person I am today and have given me a bizarre compendium of references to draw on in any situation. To Issy, you have so much potential. You are so clever and hardworking and I know that you can do anything.

To my parents, I thank you for instilling a love of science and mathematics in me. Paps, you are my role model, your encouragement and love has shown me how to be a man. You have helped me gain the confidence to battle and overcome my stammer, so I am eternally grateful. Mama, thanks for everything. Thanks for struggling through god knows much unpleasantness and trauma and still putting me and my siblings first. Thanks for giving me my passion for Maths, and always encouraging and helping me to do better. I hope I can show even a fraction of love you showed me every day to others.

# List of Abbreviations

**2D** Two-dimensional

**ARPES** Angle-resolved photoemision spectroscopy

**BLG** Bilayer graphene

**BZ** Brillouin zone

**CB** Conduction band

**ERS** Electronic Raman spectrum

**hBN** Hexagonal boron nitride

**mBZ** Magnetic Brillouin zone

**MLG** Monolayer graphene

**NDR** Negative differential resistance

**sBZ** Superlattice Brillouin zone

**tBLG** Twisted bilayer graphene

**TMD** Transition metal dichalcogenide

**tTLG** Twisted trilayer graphene

**VB** Valence band

**vdW** van der Waals

**VHS** Van Hove singularity

# Contents

**1 Introduction** **6**
1.1 van der Waals heterostructures . . . . . 7
1.2 Outline . . . . . 9

**2 Theoretical model of monolayer and bilayer graphene** **12**
2.1 Geometry of monolayer graphene . . . . . 13
2.2 Tight-binding model for monolayer graphene . . . . . 14
2.3 Tight-binding model for Bernal bilayer graphene . . . . . 18
2.3.1 Effective two-band model in Bernal bilayer graphene . . . 21
2.4 Graphene in a magnetic field . . . . . 23
2.4.1 Landau levels in monolayer graphene . . . . . 24
2.4.2 Landau levels in bilayer graphene . . . . . 25

**3 Moiré patterns in two-dimensional crystals** **27**
3.1 Geometry of moiré superlattices . . . . . 28
3.2 Twisted bilayer graphene . . . . . 29
3.3 Graphene-based van der Waals heterostructures . . . . . 36
3.3.1 Graphene on hBN . . . . . 36
3.3.2 Graphene on $\alpha - In_2Te_2$ . . . . . 40
3.4 Hofstadter's butterfly in graphene/hBN heterostructures . . . . . 42
3.4.1 Moiré perturbation of Landau levels . . . . . 43
3.4.2 Hofstadter's butterfly on a graphene/hbN superlattice . . . 44
3.A Continuum model on graphene/hBN heterostructures . . . . . 48
3.B Hexagonal coordinates: useful expressions . . . . . 49

**4 Electronic Raman scattering in twisted bilayer graphene around magic-angle twists** **51**
4.1 Introduction . . . . . 52
4.2 Theoretical description of electronic Raman scattering . . . . . 53
4.2.1 Numerical model of twisted bilayer graphene . . . . . 54

4.2.2 Current vertex calculation . . . . . 55
4.2.3 The two-step process . . . . . 55
4.3 Results . . . . . 57
4.4 Summary . . . . . 61

**5 Determination of interatomic coupling in twisted graphene using angle-resolved photoemission 63**
5.1 Introduction . . . . . 64
5.2 Theoretical model of ARPES . . . . . 64
5.3 Twisted trilayer graphene . . . . . 68
5.4 Comparison to experiment . . . . . 72
5.5 Summary . . . . . 79
5.A ARPES in twisted bilayer . . . . . 79

**6 Negative differential resistance in van der Waals heterostructures 82**
6.1 Introduction . . . . . 83
6.2 Vertical tunnelling in two-dimensional heterostructures . . . . . 86
6.2.1 hBN as a tunnel barrier . . . . . 88
6.3 Electrostatic model for van der Waals tunnelling transistors . . . 89
6.4 Graphene on hBN . . . . . 91
6.5 Twisted bilayer graphene . . . . . 94
6.6 Graphene on $\alpha - In_2Te_2$ . . . . . 95
6.7 Summary . . . . . 96

**7 Valley-polarised tunnelling currents in bilayer graphene tunnelling transistors 99**
7.1 Introduction . . . . . 100
7.2 Device description and tunnelling matrix element . . . . . 101
7.3 Momentum-conserving tunnelling . . . . . 109
7.3.1 Total tunnelling current at $B = 1$ T . . . . . 109
7.3.2 Valley polarisation at $B = 1$ T . . . . . 114
7.3.3 Tunnelling at $B = 4$ T . . . . . 116
7.4 Tunnelling with strong momentum scattering . . . . . 117
7.5 Summary . . . . . 119
7.A Changing the decay constant of graphene . . . . . 120

**8 Summary 122**
8.1 Future work . . . . . 124

**9 Bibliography** **127**

# Chapter 1

# Introduction

The ancient Greek philosopher Democritus posited that there must exist a smallest, indivisible building block of matter [3] which he named "the atom", originating from the greek "*atomos*" for un-cuttable. According to Democritus, after cutting a material many times there will eventually exist a smallest entity which cannot be cut. Following this principle, we can imagine peeling away layer after layer from a bulk material until only the thinnest possible layer exists. This was achieved at Manchester University in 2004 where, due to the weak interlayer bonds, a graphite slab was peeled down layer by layer using the famous "Scotch tape method" until eventually only single layers remained. This lead to the first experimental isolation of graphene by K. Novoselov and A. Geim in 2004 [4] sending shockwaves through the scientific community.

At the time, it was theorised that truly two-dimensional atomic crystals would be thermodynamically unstable, hence theoretical research into the electronic properties of these isolated monolayers was limited [5]. However, not only is graphene stable at room temperature, but it also possesses remarkable electronic, mechanical and optical properties leading to a surge in interest in this material within the experimental and theoretical condensed matter communities. For example, graphene has a remarkably high conductivity [6] due to its conical electronic band structure and zero band-gap. The chirality of the charge carriers in graphene leads to unique transport phenomena such as Klein tunnelling [7] and weak antilocalisation [8, 9]. In addition, graphene has a remarkably high opacity for a monolayer [10] such that optical based probes are readily deployed in order to understand the underlying physics [11]. The strong $sp^2$-bonding in graphene leads to its characteristic honeycomb structure and ultra-high tensile strength, $\sim$ 130GPa [12]. The strength and flexibility of graphene combined with its excellent electron mobility suggests applications in flexible electronics.

Since this first mechanical exfoliation, more scalable production techniques have been developed in order to isolate graphene, including chemical vapour deposition [13, 14] and molecular beam epitaxy [15]. The fabrication of higher quality graphene flakes using cheaper and more scalable methods will, over time, lead to more practical applications and as such a firm theoretical understanding of these materials is crucial.

## 1.1 van der Waals heterostructures

In only 15 years, the family of two-dimensional atomic crystals has grown rapidly. Despite often having similar crystallographic structures, the electronic

and optical properties of these materials differ significantly. Hexagonal boron nitride (hBN), for example, is a wide band gap insulator [16] and has uses as a substrate for graphene devices [17] due to the flat interface formed between the hBN and graphene layers. Transition metal dichalcogenides (TMDs) are another species of two-dimensional atomic crystal. Depending on the choice of transition metal and chalcogen, the electronic properties of the TMD will vary. For example, $MoSe_2$ is a direct bandgap semiconductor [18] while $TaSe_2$, where molybdenum is replaced with tantalum, is metallic [19]. These materials have been shown to demonstrate correlated electronic properties, including charge density waves [20, 21] and, at large carrier concentrations, superconductivity [22].

These two-dimensional (2D) materials can be stacked on top of each other. By virtue of being two-dimensional, the "bulk" of the 2D material is in close proximity to adjacent layers, different to three dimensional bulk materials. The most common example of this is Bernal (AB) bilayer graphene, where the conical band structure of monolayer graphene becomes parabolic as a result of interlayer coupling between the two stacked graphene layers [23]. Monolayer graphene, despite its remarkable electronic properties, was never considered a replacement for silicon in circuit transistors. The so-called "band-gap problem" of monolayer graphene, referring to the lack of a band gap in its low energy band-structure, prevents an ON and OFF state from being clearly defined [24]. By applying a perpendicular electric field to a Bernal stacked bilayer a tuneable energy gap opens at the neutrality point [25], creating a semiconducting material, enabling a wider array of applications.

In most cases, the interlayer interactions between these two-dimensional atomic crystals are governed by weak van der Waals forces [26, 27]. As a result, the crystallographic alignment of these multilayered devices is not fixed and instead the relative translational and rotational offset between the two layers becomes an additional degree of freedom in their fabrication. Recently, it has been observed that the stark spectral transformation of the bilayer graphene band structure as a result of this misalignment angle [28] leads to unexpected strongly-correlated physics including superconductivity [29, 30]. The resulting material, known as twisted bilayer graphene, is the first purely carbon superconductor when the twist is reduced to the so-called magic-angle. The exact mechanism resulting in the onset of superconductivity in this material is unknown and is an area of significant interest in the condensed matter community, not least because it could help explain the superconductivity in high-$T_c$ superconductors. This is because, although the superconducting transition temperature of this material is low, $T_c \approx 1$ K, the relatively low charge density suggests that the superconducting order parameter

is relatively large.

Previous experimental studies have shown that dramatic spectral modification is observed when graphene is placed on a host of almost commensurate two-dimensional materials [31, 32, 33, 34, 35, 36]. Furthermore, the beating of these two similar periodicities leads to a new large scale superlattice, with a unit cell on the scale of $\sim 10$ nm. This moiré pattern has been shown to lead to Hofstadter's butterfly in graphene on hbN superlattices [37, 38] as well as in twisted bilayer graphene [39]. As a result, high temperature quantum fluctuations have been observed in such a system due to Brown-Zak oscillations, where, in a quantizing magnetic field, charge carriers behave as if they were moving in the absence of such a field [40].

The large number of degrees of freedom that are exploitable during the fabrication of these heterostructures offers physicists a vast playground within which to explore unique physics and novel applications.

## 1.2 Outline

In this thesis, we seek to describe the electronic and optical properties of various graphene-based van der Waals heterostructures. We begin by introducing the theoretical models describing the electronic band structures of 2D materials. Starting with monolayer graphene we derive an expression for the electronic band structure based on the tight-binding model before an effective low-energy description around the Brillouin zone corners is formulated. By stacking two aligned monolayers, we demonstrate that the resulting band structure is parabolic and susceptible to an applied perpendicular electric field. We then derive an effective low-energy model for the lowest energy bands in this bilayer graphene. Moreover, we calculate the Landau level spectrum and wavefunctions for monolayer and bilayer graphene, arising as a result of a strong magnetic field applied perpendicularly to the layer plane.

We then move on to discuss the origin of moiré patterns and superlattices in van der Waals heterostructures in Chapter 3. We introduce the continuum model for twisted bilayer graphene as a way to describe the interlayer coupling, even for incommensurate structures. Then, the general perturbation Hamiltonian for graphene on an almost commensurate substrate, in this case hBN, is derived phenomenologically. We extend this to a system with graphene on an almost commensurate $\sqrt{3} \times \sqrt{3}$ lattice. We demonstrate that under application of a large perpendicular magnetic field, the Landau level spectrum of a closely-aligned

graphene-hBN heterostructure is strongly modified leading to a fractal spectra known as Hofstadter's butterfly.

In Chapter 4, we focus on twisted bilayer graphene around the magic-angle. In particular we demonstrate that, in theory, the electronic Raman spectrum of twisted bilayer graphene acts as a probe of the misalignment angle. We show that individual features in the electronic Raman spectrum can be attributed to specific electron-hole excitations and that by noting the position and spectral profile of these peaks, the misalignment angle can be inferred. The position of these peaks, in the context of the overall Raman spectrum, suggests that the desired features will not have to compete with known phonon-mode peaks, and that the electronic Raman amplitude is larger than that theorised and previously measured in monolayer graphene.

In Chapter 5, we introduce a theoretical model for angle-resolved photoemission spectroscopy (ARPES) before comparing theoretical and experimental results for twisted trilayer graphene, a three-layer structure where a monolayer is stacked misaligned on top of a Bernal stacked bilayer. Uniquely for such a trilayer structure, the presence of both aligned and misaligned configurations allows us to compare descriptions in both real and reciprocal spaces and extract information about the interatomic coupling. We demonstrate good agreement between the experimental ARPES data and our theoretical ARPES model and coupling parameterisation for two twist angles. We show that our parametrisation, self-consistently describes the coupling in both aligned and twisted bilayer graphene, marrying the tight-binding and continuum models typically employed to describe these systems. Furthermore, in order to compare experimental and theoretical ARPES data, we successfully model the substrate doping effect observed in experiment, resulting in different on-site energies of the graphene layers.

From Chapter 6 onwards, we shift our attention to van der Waals tunnelling transistors. Here we discuss theoretically electron transport in a van der Waals tunnelling transistor in which one or both of the electrodes are made of two crystals forming a moiré superlattice at their interface. As a proof of concept, we investigate structures containing either an aligned graphene/hexagonal boron nitride heterostructure or twisted-bilayer graphene and show that negative differential resistance is possible in such transistors and that this arises as a consequence of the superlattice-induced changes in the electronic density of states and without the need for momentum conserving tunnelling present in high-quality exfoliated devices. We extend this concept to a device with electrodes consisting of aligned graphene on $\alpha - In_2Te_2$ and demonstrate negative-differential-resistance peak-to-valley ratios of approximately 10.

In Chapter 7, we study theoretically the electron current across a monolayer graphene/hexagonal boron nitride/bilayer graphene tunnelling junction in an external magnetic field perpendicular to the layers. Since, in bilayer graphene, the Landau level wave functions are not equally distributed amongst the layers, and that this distribution is reversed between the two valleys, the change in effective tunnelling barrier width for electrons on different graphene layers leads to valley polarisation of the tunnelling current. We estimate that valley polarisation $\sim 80\%$ can be achieved in high quality devices at $B = 1$ T. Moreover, we demonstrate that strong valley polarisation can be obtained both in the limit of strong-momentum conserving tunnelling and in lower quality devices where this constraint is lifted.

Finally, we summarise the results presented in this thesis in Chapter 8 before introducing some avenues for future work.

# Chapter 2

# Theoretical model of monolayer and bilayer graphene

## 2.1 Geometry of monolayer graphene

Monolayer graphene (MLG) is a two-dimensional isomer of carbon arranged in a honeycomb structure [41, 42], as shown in Fig. 2.1 (a) and (b). In particular, MLG can be described as a triangular Bravais lattice with a two atom unit cell. These two carbon atoms, typically labelled $A$ and $B$, are symmetrically non-equivalent and are known as the sublattice basis of MLG. The typical carbon-carbon spacing between adjacent $A$ and $B$ atoms is roughly $a_0 = 1.46$ Å[41, 43, 44] and this defines the carbon-carbon distance. The primitive Bravais lattice vectors of graphene, shown in red in Fig. 2.1 (a), are written as

$$\boldsymbol{a_1} = a\left(\frac{1}{2}, \frac{\sqrt{3}}{2}\right), \quad \boldsymbol{a_2} = a\left(-\frac{1}{2}, \frac{\sqrt{3}}{2}\right), \tag{2.1}$$

where $a = \sqrt{3}a_0 = 2.46$ Åis the graphene lattice constant. We note that no linear combination of primitive lattice vectors, $\boldsymbol{R} = m\boldsymbol{a_1} + n\boldsymbol{a_2}$, where $m, n \in \mathbb{Z}$, will connect the A and B sublattices. Instead it is necessary to define a new set of vectors which connect an A atom to its three nearest B sublattice neighbours, shown in green in Fig. 2.1 (a)

$$\boldsymbol{\delta_j} = \hat{\boldsymbol{R}}_{\frac{2\pi(j-1)}{3}}(0, a_0), \tag{2.2}$$

$$\hat{\boldsymbol{R}}_\theta = \begin{pmatrix} \cos\theta & -\sin\theta \\ \sin\theta & \cos\theta \end{pmatrix}, \tag{2.3}$$

where $\hat{\boldsymbol{R}}_\theta$ defines the anticlockwise rotation operator by angle $\theta$. The reciprocal lattice vectors associated with the Bravais lattice vectors of graphene are expressed as

$$\boldsymbol{G_1} = \left(\frac{2\pi}{a}, \frac{2\pi}{\sqrt{3}a}\right), \quad \boldsymbol{G_2} = \left(-\frac{2\pi}{a}, \frac{2\pi}{\sqrt{3}a}\right). \tag{2.4}$$

The first Brillouin zone (BZ) associated with these reciprocal lattice vectors is hexagonal as demonstrated in Fig. 2.1 (c). Due to the hexagonal nature of the Brillouin zone, opposite corners, indexed by $\xi = \pm 1$, $\boldsymbol{K_\xi} = \left(\xi\frac{4\pi}{3a}, 0\right)$ cannot be connected by reciprocal lattice vectors. These inequivalent points are known as valleys and it is around these points where most of the low-energy physics in graphene is described.

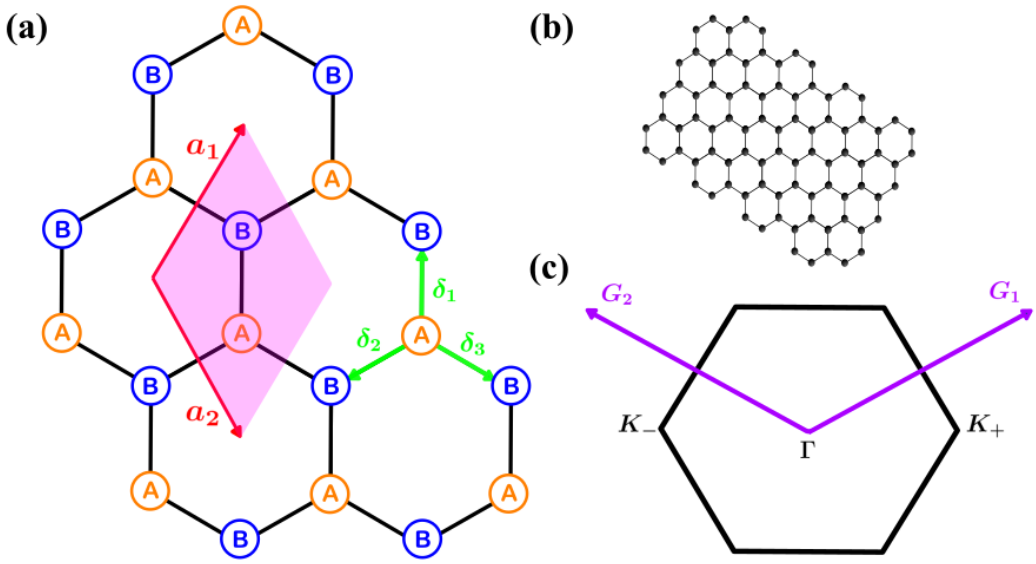


**Figure 2.1:** (a) Lattice structure of monolayer graphene with sublattice labels A and B shown in orange and blue respectively. The red lattice vectors, $\boldsymbol{a}_1$ and $\boldsymbol{a}_2$, define the unit cell shown in pink. The green vectors $\boldsymbol{\delta}_i$ $(i = 1, 2, 3)$ connect nearest neighbours on different sublattices. (b) Crystal structure in (a) extended to include more unit cells. (c) Brillouin zone (black hexagon) with high symmetry points labelled. The reciprocal lattice vectors $\boldsymbol{G_1}$ and $\boldsymbol{G_2}$ are shown in purple.

## 2.2 Tight-binding model for monolayer graphene

In this section we introduce the commonly used tight-binding model for monolayer graphene, first proposed by Wallace [41], which has been shown to describe most low-energy single-particle electronic properties. The model's validity rests on the assumption that the electronic wavefunctions in graphene can be entirely described using the atomic orbitals of the constituent carbon atoms, or in other words, the electrons are "tightly-bound" to the carbon atoms.

Carbon is a group IV element and hence provides 4 outer shell electrons occupying the $2p$ and $2s$ orbitals [41, 44, 45, 46, 47] (plus two core electrons in $1s$ orbital). In other carbon allotropes such as diamond, the electrons are shared between all $2s$ and $p$ orbitals forming four $sp^3$- hybrids. This is responsible for the tetrahedral crystal structure in diamond. In graphene, however, the electrons redistribute forming three $sp^2$-hybrid orbitals [42]. In particular, the $2s$, $2p_x$ and $2p_y$ form strong in-plane covalent bonds with neighbouring orbitals forming the characteristic honeycomb structure of MLG. The remaining $2p_z$ orbitals project out of plane and form weak $\pi$-bonds with neighbouring $2p_z$ orbitals and it is

these which are responsible for the low-energy physics in MLG. Therefore, the wave function of MLG can be constructed from Bloch states composed of $2p_z$ orbitals. For a given wave vector $\boldsymbol{k}$ and position $\boldsymbol{r}$, the electronic wave function of the $j$th energy level, $\Psi_j(\boldsymbol{r},\boldsymbol{k})$, in the tight-binding model is described as a linear superposition of $n$ distinct Wannier functions, $\psi_m$ [42, 44, 47],

$$|\Psi_j(\boldsymbol{r},\boldsymbol{k})\rangle = \frac{1}{\sqrt{N}}\sum_{m}^{n}\sum_{l}^{N} e^{i\boldsymbol{k}\boldsymbol{R}_{l,m}} c_{m,j}\,|\psi_m(\boldsymbol{r}-\boldsymbol{R}_{l,m})\rangle\,. \tag{2.5}$$

We define $\boldsymbol{R}_{l,m} = \boldsymbol{R}_l + \boldsymbol{\tau}_m$ as the position of the $m$th orbital in the $l$th unit cell while $c_{m,j}$ represent the relative magnitudes of the $m$th orbital in the $j$th wave function in the superposition. In the case of graphene there are $n = 2$ orbitals per unit cell, A and B. For a Hamiltonian, $\mathcal{H}$, the transfer integral, $H_j(\boldsymbol{k})$, and overlap integral, $S_j(\boldsymbol{k})$, can be expressed as

$$H_j(\boldsymbol{k}) = \langle\Psi_j(\boldsymbol{r},\boldsymbol{k})|\,\mathcal{H}\,|\Psi_j(\boldsymbol{r},\boldsymbol{k})\rangle\,, \quad S_j(\boldsymbol{k}) = \langle\Psi_j(\boldsymbol{r},\boldsymbol{k})|\Psi_j(\boldsymbol{r},\boldsymbol{k})\rangle\,. \tag{2.6}$$

From these, the energy of the $j$th band can be derived

$$E_j(\boldsymbol{k}) = \frac{H_j(\boldsymbol{k})}{S_j(\boldsymbol{k})}. \tag{2.7}$$

Using Eq. (2.7) and minimising with respect to the coefficients of the linear superposition we can obtain the equation

$$\frac{1}{N}\sum_{l,l'=1}^{N}\sum_{m,m'=A,B} c_{m,j}e^{i\boldsymbol{k}(\boldsymbol{R}_{l,m}-\boldsymbol{R}_{l',m'})}H^{l,l'}_{m,m'} = \frac{E_j}{N}\sum_{l,l'=1}^{N}\sum_{m,m'=A,B} c_{m,j}e^{i\boldsymbol{k}(\boldsymbol{R}_{l,m}-\boldsymbol{R}_{l',m'})}S^{l,l'}_{m,m'}, \tag{2.8}$$

where the matrix elements are defined as

$$\begin{aligned} H^{l,l'}_{m,m'}(\boldsymbol{k}) &= \langle\psi_{m'}(\boldsymbol{r}-\boldsymbol{R}_{l',m'})|\,\mathcal{H}\,|\psi_m(\boldsymbol{r}-\boldsymbol{R}_{l,m})\rangle\,, \\ S^{l,l'}_{m,m'} &= \langle\psi_{m'}(\boldsymbol{r}-\boldsymbol{R}_{l',m'})|\psi_m(\boldsymbol{r}-\boldsymbol{R}_{l,m})\rangle\,. \end{aligned} \tag{2.9}$$

From this eigenvalue equation it is possible to find the value of the $j$th band by using the secular equation $\det(H - E_jS) = 0$. The above expression can be expressed as a $2\times 2$ matrix on the AB sublattice space of monolayer graphene

$$\begin{pmatrix} H_{AA} & H_{AB} \\ H_{BA} & H_{BB} \end{pmatrix}\begin{pmatrix} c_{A,j} \\ c_{B,j} \end{pmatrix} = E_j\begin{pmatrix} S_{AA} & S_{AB} \\ S_{BA} & S_{BB} \end{pmatrix}\begin{pmatrix} c_{A,j} \\ c_{B,j} \end{pmatrix}, \tag{2.10}$$

where the summations are absorbed into the matrix elements. The term $H_{AA}(H_{BB})$ represents electron transfer between equivalent sublattices while $H_{AB}(H_{BA})$ represents transfer between different sublattices. The coupling element $H_{AA}$ becomes

$$H_{AA} = \frac{1}{N}\sum_{l,l'=1}^{N} e^{i\boldsymbol{k}(\boldsymbol{R}_{l,A}-\boldsymbol{R}_{l',A})} \left\langle \psi_A(\boldsymbol{r}-\boldsymbol{R}_{l,A})\right| \mathcal{H} \left|\psi_A(\boldsymbol{r}-\boldsymbol{R}_{l',A})\right\rangle . \tag{2.11}$$

The sum over $N$ unit cells is large and introduces multiple combinations including transfer between orbitals with large spatial separation. As such, under the tight-binding assumption, it is possible to restrict the sum to only include terms where $l = l'$ resulting in

$$H_{AA} \simeq \frac{1}{N}\sum_{l=1}^{N} \left\langle \psi_A(\boldsymbol{r}-\boldsymbol{R}_{l,A})\right| \mathcal{H} \left|\psi_A(\boldsymbol{r}-\boldsymbol{R}_{l,A})\right\rangle = E_0, \tag{2.12}$$

where $E_0$ describes the on-site potential of the $2p_z$ orbital and, due to symmetry arguments, $H_{BB} = H_{AA}$. Following the same reasoning, the summation in $H_{AB}$ can be truncated to only include the three nearest-neighbour hoppings

$$\begin{aligned} H_{AB} &\simeq \frac{1}{N}\sum_{l'=1}^{3}\sum_{l=1}^{N} e^{i\boldsymbol{k}\cdot\boldsymbol{\delta}_{l'}} \left\langle \psi_A(\boldsymbol{r}-\boldsymbol{R}_{l,A})\right| \mathcal{H} \left|\psi_A(\boldsymbol{r}-\boldsymbol{R}_{l',B})\right\rangle = \gamma_0 f(\boldsymbol{k}), \\ f(\boldsymbol{k}) &= \sum_{l'=1}^{3} e^{i\boldsymbol{k}\cdot\boldsymbol{\delta}_{l'}}, \end{aligned} \tag{2.13}$$

where $\gamma_0$ is the nearest neighbour hopping parameter in graphene and is estimated to be equal to $\gamma_0 = -3.1$eV [41]. Different values of this parameter have been obtained from experiment [11], density functional theory [48] and the Slonczewski-Weiss-McClure model [45] within the range of $-2.7 \to -3.2$ eV. By virtue of the reversed sign of $\boldsymbol{\delta}_j$ when hopping from B to A, $H_{AB} = H_{BA}^{\dagger}$ thus ensuring our Hamiltonian is Hermitian

$$\hat{\boldsymbol{H}}_{\mathrm{MLG}} = \begin{pmatrix} E_0 & \gamma_0 f(\boldsymbol{k}) \\ \gamma_0 f^*(\boldsymbol{k}) & E_0 \end{pmatrix}. \tag{2.14}$$

Applying the same constraints to the overlap integral matrix $S$, one finds

$$\begin{aligned} S_{AA} &= S_{BB} = 1 \\ S_{AB} &= S_{BA}^{\dagger} = s_0 f(\boldsymbol{k}), \end{aligned} \tag{2.15}$$

where $s_0 = 0.129$ [41]. In the entirety of this thesis, energy is measured relative

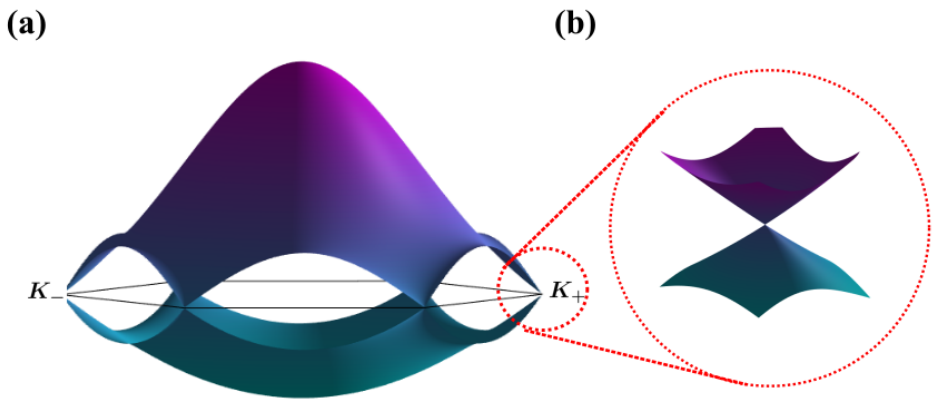


**Figure 2.2:** (a) Electronic band structure of monolayer graphene. The Brillouin zone is shown by a black hexagon. (b) Low-energy band structure close to the Brillouin zone corner or valley $\boldsymbol{K}_+$ shown in (a).

to the on-site energy, $E_0$, which is therefore set to 0 for simplicity. The energy bands of monolayer graphene can thus be obtained using Eqs. (2.10), (2.14) and (2.15) and are presented in Fig. 2.2 (a). As touched on in the previous section, the low-energy physics of graphene is described in the vicinity of the Brillouin zone corners ("valleys"). Therefore, performing a Taylor expansion of $f(\boldsymbol{k})$ for small $\boldsymbol{p}/\hbar$ around the valley $\boldsymbol{K}_\xi$ we obtain, to first order,

$$f(\boldsymbol{k}) \to f(\boldsymbol{K}_\xi) + \boldsymbol{p} \cdot \frac{1}{\hbar} \boldsymbol{\nabla} f(\boldsymbol{K}_\xi) + ... \tag{2.16}$$

$$\simeq -\frac{a\sqrt{3}}{2\hbar}(\xi p_x - i p_y). \tag{2.17}$$

The term $v = -\dfrac{\gamma_0 a\sqrt{3}}{2\hbar}$ is defined as the Fermi velocity of electrons in graphene. Therefore continuing from Eq. (2.10), we obtain an expression for the effective low-energy Hamiltonian

$$\hat{\boldsymbol{\mathcal{H}}}_{\mathrm{MLG}} = v \begin{pmatrix} 0 & \xi p_x - i p_y \\ \xi p_x + i p_y & 0 \end{pmatrix}. \tag{2.18}$$

The resulting low-energy linear band structure, in the vicinity of the $\boldsymbol{K}_+$ is shown in Fig. 2.2 (b) where we find that the energy spectrum is linear and gapless, forming a so-called "Dirac-cone", whose gradient is defined by the Fermi velocity, $v$.

As such, we find the resulting energy level and eigenstate in monolayer graphene

$$E = sv|\boldsymbol{p}|, \quad \psi_s = \begin{pmatrix} 1 \\ si\xi e^{i\xi\theta} \end{pmatrix}, \tag{2.19}$$

where $\theta$ is the polar angle of $\boldsymbol{p} = |\boldsymbol{p}|(\cos\theta, \sin\theta)$ and $s$ is the band index. The coupled momentum direction $\theta$ and sublattice index, $\{A, B\}$, is referred to as chirality, and this is responsible for some of the interesting transport behaviour in graphene such as Klein tunnelling [7].

## 2.3 Tight-binding model for Bernal bilayer graphene

Bilayer graphene (BLG) is composed of two vertically-stacked layers of monolayer graphene. There are a few different types of stacking in Bilayer graphene, these include: AA, where A (B) sublattices are directly over each other; Bernal (AB), where the A atoms in the top layer are directly above B atoms in the bottom layer; and twisted bilayer, where the graphene monolayers are stacked with arbitrary in-plane misalignment. The most commonly observed stacking in exfoliated samples is Bernal as it is the most energetically favourable [49, 50, 51]. This thesis will focus on Bernal and twisted bilayer.

The unit cell in Bernal-stacked bilayer graphene, is the same size as in MLG (as shown in Fig. 2.3 (a)), however it now contains 4 carbon $p_z$ orbitals. We label these $A1$, $B1$ in the bottom layer and $A2$, $B2$ in the top layer such that $B1$ lies directly below $A2$. Restricting the sum to nearest neighbours, the tight-binding coupling element between $B1$ and $A2$ is

$$H_{A2,B1} \simeq \frac{1}{N}\sum_{l=1}^{N} \langle\psi_{A2}(\boldsymbol{r} - \boldsymbol{R}_{l,A})|\, \mathcal{H}\, |\psi_{B1}(\boldsymbol{r} - \boldsymbol{R}_{l,B1})\rangle = \gamma_1, \tag{2.20}$$

where $\gamma_1 = 0.39$eV [50] and describes the strongest interlayer hopping in bilayer graphene. For completeness, it is necessary to include the skew-interlayer hop-

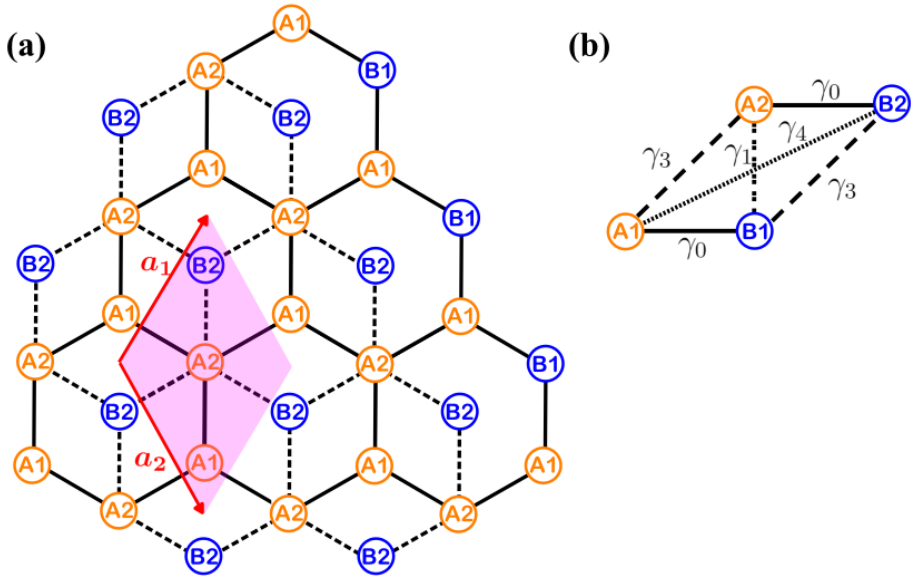


**Figure 2.3:** (a) Crystal structure of Bernal-stacked bilayer graphene, with A and B sublattices labelled in orange and blue respectively, while 1 and 2 refer to the bottom and top layer respectively. The solid (dashed) hexagons belong to the bottom (top) monolayer graphene layer. The lattice vectors are shown in red and the unit cell is shown in pink. (b) Side-on view of the 4 atom Bernal bilayer graphene unit cell.The coupling constants between these atoms are indicated by adjoining lines.

pings $A1 \leftrightarrow A2$, $B1 \leftrightarrow B2$ and $A1 \leftrightarrow B2$

$$
\begin{aligned}
H_{A1,A2} &\simeq \frac{1}{N}\sum_{l'=1}^{3}\sum_{l=1}^{N} e^{i\boldsymbol{k}\cdot\boldsymbol{\delta}_{l'}} \left\langle \psi_{A1}(\boldsymbol{r}-\boldsymbol{R}_{l,A1})\right| \mathcal{H} \left|\psi_{A2}(\boldsymbol{r}-\boldsymbol{R}_{l',A2})\right\rangle = \gamma_3 f(\boldsymbol{k}),\\
H_{B1,B2} &\simeq \frac{1}{N}\sum_{l'=1}^{3}\sum_{l=1}^{N} e^{i\boldsymbol{k}\cdot\boldsymbol{\delta}_{l'}} \left\langle \psi_{B1}(\boldsymbol{r}-\boldsymbol{R}_{l,B1})\right| \mathcal{H} \left|\psi_{B2}(\boldsymbol{r}-\boldsymbol{R}_{l',B2})\right\rangle = \gamma_3 f(\boldsymbol{k}),\\
H_{A1,B2} &\simeq \frac{1}{N}\sum_{l'=1}^{3}\sum_{l=1}^{N} e^{i\boldsymbol{k}\cdot\boldsymbol{\delta}_{l'}} \left\langle \psi_{A1}(\boldsymbol{r}-\boldsymbol{R}_{l,A1})\right| \mathcal{H} \left|\psi_{B2}(\boldsymbol{r}-\boldsymbol{R}_{l',B2})\right\rangle = \gamma_4 f^*(\boldsymbol{k}),
\end{aligned}
\tag{2.21}
$$

where the skew interlayer coupling strengths, $\gamma_3$ and $\gamma_4$, vary between experiment and theory [11, 50]. The sites connected by $\gamma_1$ are referred to as "dimer" sites. Although the separations defining $\gamma_3$ and $\gamma_4$ are the same, the local environment of dimer and non-dimer atoms are different, hence $\gamma_3$ and $\gamma_4$ are defined separately [45, 50]. These coupling parameters are shown schematically in Fig. 2.3 (b). Using these coupling parameters, we can extend the tight-binding model for

monolayer graphene to a two layer case

$$\hat{\boldsymbol{H}}_{\mathrm{BLG}} = \begin{pmatrix} 0 & \gamma_0 f(\boldsymbol{k}) & \gamma_4 f(\boldsymbol{k}) & \gamma_3 f^*(\boldsymbol{k}) \\ \gamma_0 f^*(\boldsymbol{k}) & 0 & \gamma_1 & \gamma_4 f(\boldsymbol{k}) \\ \gamma_4 f^*(\boldsymbol{k}) & \gamma_1 & 0 & \gamma_0 f(\boldsymbol{k}) \\ \gamma_3 f(\boldsymbol{k}) & \gamma_4 f^*(\boldsymbol{k}) & \gamma_0 f^*(\boldsymbol{k}) & 0 \end{pmatrix}. \tag{2.22}$$

Similarly to monolayer graphene, the band structure in bilayer graphene has conduction-band-minima and valence-band-maxima at the $\boldsymbol{K}$ points, however the low-energy dispersion is approximately parabolic. The low energy band structure

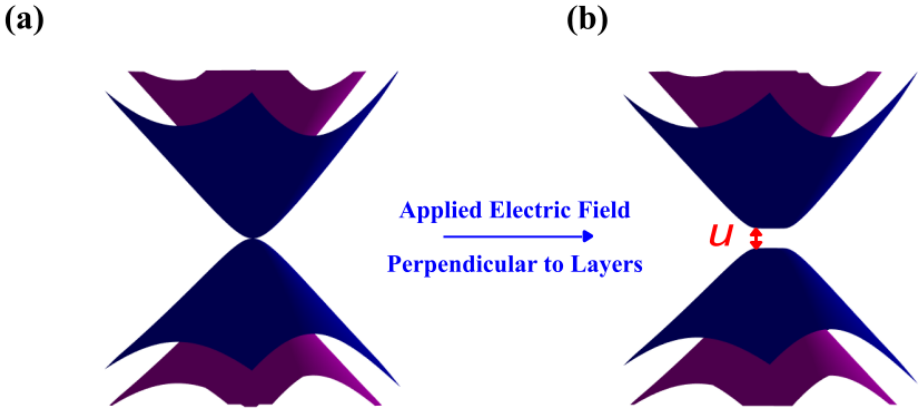


**Figure 2.4:** (a) Low energy electronic band structure of Bernal bilayer graphene in the vicinity of the $\boldsymbol{K}_+$ valley. (b) An applied perpendicular electric field leads to a non-zero band gap, $u$, shown in red, at the neutrality point. We set $\gamma_3 = \gamma_4 = 0$ for simplicity.

in the vicinity of the $\boldsymbol{K}_+$ valley is shown in Fig. 2.4 (a) where there exist additional bands approximately $\gamma_1$ above and below the neutrality point, as compared to MLG. Due to the interlayer separation in BLG it is relatively easy to generate an on-site energy difference, $u$, between the top and bottom layer by means of a perpendicular electric field

$$\hat{\boldsymbol{H}}_{\mathrm{BLG}}(u) = \begin{pmatrix} \frac{u}{2} & \gamma_0 f(\boldsymbol{k}) & \gamma_4 f(\boldsymbol{k}) & \gamma_3 f^*(\boldsymbol{k}) \\ \gamma_0 f^*(\boldsymbol{k}) & \frac{u}{2} & \gamma_1 & \gamma_4 f(\boldsymbol{k}) \\ \gamma_4 f^*(\boldsymbol{k}) & \gamma_1 & -\frac{u}{2} & \gamma_0 f(\boldsymbol{k}) \\ \gamma_3 f(\boldsymbol{k}) & \gamma_4 f^*(\boldsymbol{k}) & \gamma_0 f^*(\boldsymbol{k}) & -\frac{u}{2} \end{pmatrix}. \tag{2.23}$$

In Bernal bilayer graphene, this leads to a band gap at the neutrality point as shown in Fig. 2.4 (b). Analogous to MLG, the Hamiltonian can be expanded in

terms of small $\boldsymbol{p}$ around the $K_\xi$ point

$$\hat{\boldsymbol{\mathcal{H}}}_{\mathrm{BLG}}(u) = \begin{pmatrix} \frac{u}{2} & v\pi^\dagger & v_4\pi^\dagger & v_3\pi \\ v\pi & \frac{u}{2} & \gamma_1 & v_4\pi^\dagger \\ v_4\pi & \gamma_1 & -\frac{u}{2} & v\pi \\ v_3\pi^\dagger & v_4\pi & v\pi^\dagger & -\frac{u}{2} \end{pmatrix}, \tag{2.24}$$

where $v_3 = -\dfrac{\gamma_3 a\sqrt{3}}{2\hbar}$ and $v_4 = \dfrac{\gamma_4 a\sqrt{3}}{2\hbar}$ are effective velocities and the terms $\pi = \xi p_x + ip_y$ are introduced for clarity.

### 2.3.1 Effective two-band model in Bernal bilayer graphene

After calculating the eigenvalues and eigenstates of the Hamiltonian in Bernal (AB) bilayer, the wavefunctions associated with the low energy bands around the neutrality point are almost entirely distributed on the $A1$ and $B2$ sublattices. Therefore, it follows that the low-energy properties of Bernal bilayer graphene (for energies below $\gamma_1$) can be described using an effective Hamiltonian acting only on the basis of the non-dimer sites $A1$ and $B2$ [25, 50].

The basis of Eq. (2.23) can be written in terms of dimer and non-dimer parts, $\psi_D = (\psi_{A2}, \psi_{B1})^T$ and $\psi_N = (\psi_{A1}, \psi_{B2})^T$, respectively such that the eigenvalue equation becomes

$$\begin{pmatrix} H_N & T \\ T^\dagger & H_D \end{pmatrix} \begin{pmatrix} \psi_N \\ \psi_D \end{pmatrix} = E \begin{pmatrix} \psi_N \\ \psi_D \end{pmatrix}. \tag{2.25}$$

Without making any assumptions about the magnitude of the coupling strengths, we define

$$H_N = \begin{pmatrix} \frac{u}{2} & v_3\pi \\ v_3\pi^\dagger & -\frac{u}{2} \end{pmatrix}, \qquad H_D = \begin{pmatrix} -\frac{u}{2} & \gamma_1 \\ \gamma_1 & \frac{u}{2} \end{pmatrix}, \qquad T = \begin{pmatrix} v_4\pi^\dagger & v\pi^\dagger \\ v\pi & v_4\pi \end{pmatrix}. \tag{2.26}$$

The resulting set of simultaneous equations leads to the relation

$$\left[H_N + T(E - H_D)^{-1}T^\dagger\right]\psi_N = E\psi_N. \tag{2.27}$$

The equation can be simplified using the approximation $\frac{1}{a-x} \approx -\frac{1}{x} - \frac{a}{x^2}$, which

holds when $E < H_D$, true for low-energy electrons

$$\left[H_N - TH_D^{-1}T^\dagger\right]\psi_N = ES\psi_N, \tag{2.28}$$

where $S = 1 + TH_D^{-2}T^\dagger$. This operator acts on the state $\psi_N$ and as such is not normalised. In order to account for this we note that the dimer state can be written in terms of the non-dimer states as $\psi_D = (E - H_D)^{-1}T^\dagger\psi_N$ such that

$$\psi_D^\dagger\psi_D = \psi_N^\dagger T(E - H_D)^{-2}T^\dagger\psi_N \approx \psi_N^\dagger TH_D^{-2}T^\dagger\psi_N. \tag{2.29}$$

Using this relationship and the expression for $S$, it follows that the normalisation is recovered under the transformation $\Phi = S^{1/2}\psi_N$ such that

$$S^{-1/2}\left[H_N - TH_D^{-1}T^\dagger\right]S^{-1/2}\Phi = E\Phi. \tag{2.30}$$

Therefore the effective two-band Hamiltonian can be written as

$$\hat{\boldsymbol{\mathcal{H}}}_{\text{eff,BLG}} = S^{-1/2}\left[H_N - TH_D^{-1}T^\dagger\right]S^{-1/2}. \tag{2.31}$$

Substituting the expressions from Eq. (2.26) allows the approximate low-energy bands around the $\boldsymbol{K_\xi}$ points in bilayer graphene to be found. Further approximations can be made by noting that $|\gamma_0|, |\gamma_1| >> |E|, |\gamma_3|, |\gamma_4|, |u|$ hence only terms that are linear in these smaller parameters are considered. As such, the resulting two-band Hamiltonian is

$$\begin{aligned}
\hat{\boldsymbol{\mathcal{H}}}_{\text{eff,BLG}} &= \hat{\boldsymbol{h}}_0 + \hat{\boldsymbol{h}}_3 + \hat{\boldsymbol{h}}_4 + \hat{\boldsymbol{h}}_u, \\
\hat{\boldsymbol{h}}_0 &= -\frac{1}{2m}\begin{pmatrix} 0 & (\pi^\dagger)^2 \\ \pi^2 & 0 \end{pmatrix}, \\
\hat{\boldsymbol{h}}_3 &= v_3\begin{pmatrix} 0 & \pi^\dagger \\ \pi & 0 \end{pmatrix} - \frac{v_3 a}{4\sqrt{3}\hbar}\begin{pmatrix} 0 & (\pi^\dagger)^2 \\ \pi^2 & 0 \end{pmatrix}, \\
\hat{\boldsymbol{h}}_4 &= \frac{2vv_4}{\gamma_1}\begin{pmatrix} \pi^\dagger\pi & 0 \\ 0 & \pi^\dagger\pi \end{pmatrix}, \\
\hat{\boldsymbol{h}}_u &= \frac{\xi u}{2}\begin{pmatrix} 1 & 0 \\ 0 & -1 \end{pmatrix} + \frac{\xi u v^2}{\gamma_1^2}\begin{pmatrix} \pi^\dagger\pi & 0 \\ 0 & \pi^\dagger\pi \end{pmatrix},
\end{aligned} \tag{2.32}$$

acting on the basis $(c_{A1}, c_{B2})^T$. Throughout this thesis, we neglect all terms involving $\gamma_3$ and $\gamma_4$ as they have much less effect on the electron properties [23, 52] when compared to $\gamma_1$ and $u$. Hence we take $\hat{\boldsymbol{\mathcal{H}}}_{\text{LE,BLG}} = \hat{\boldsymbol{h}}_0 + \hat{\boldsymbol{h}}_u$.

## 2.4 Graphene in a magnetic field

In this section we discuss the effect of a perpendicular magnetic field on the electronic properties of monolayer and bilayer graphene. Due to the Lorentz force, electrons in graphene (or any two-dimensional electronic system) become confined to cyclotron orbits when a magnetic field is applied perpendicularly to the layer plane, as demonstrated in Fig. 2.5 (a).

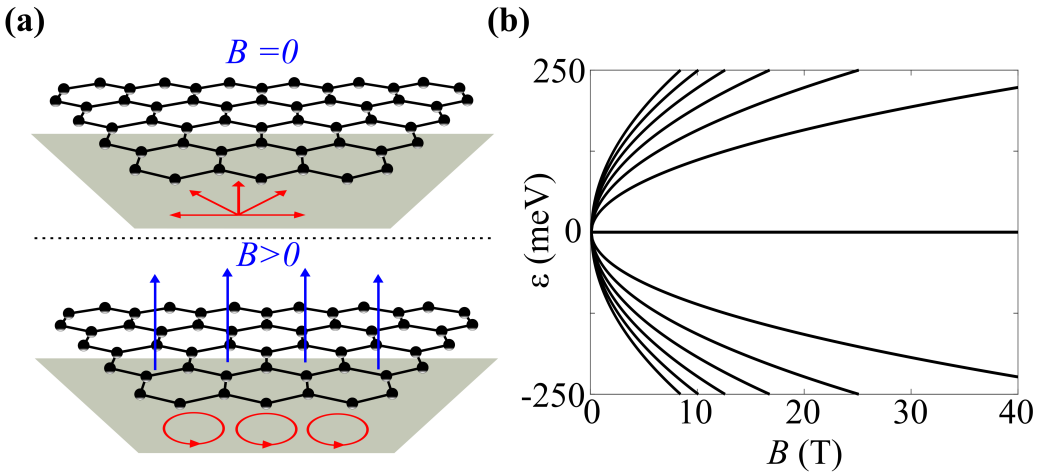


**Figure 2.5:** (a) Top image shows graphene in the absence of a magnetic field, charge transport (red arrows) is allowed in all directions within the layer plane (shown in grey). The bottom image shows graphene with a perpendicular magnetic field (with field lines shown in blue). The electrons become confined to cyclotron orbits (red) due to the Lorentz force. (b) Landau level spectrum of monolayer graphene as a function of applied magnetic field.

A perpendicular magnetic field, $\boldsymbol{B} = |\boldsymbol{B}|\hat{\boldsymbol{e}}_z$, gives rise to a vector potential, $\boldsymbol{A}$, parallel to the layer plane by the equation

$$\boldsymbol{B} = \boldsymbol{\nabla} \times \boldsymbol{A}, \tag{2.33}$$

where $\boldsymbol{\nabla}$ is the gradient operator from vector calculus. The simplest gauge to use is the Landau gauge defined as $\boldsymbol{A} = (0, -Bx, 0)$. For tightly-bound electrons, an electron hopping between atomic sites, positioned $\boldsymbol{R}_i$ and $\boldsymbol{R}_f$, in a vector potential gains a phase factor known as the Peierls phase [53]

$$\Phi = \frac{e}{\hbar} \int_{\boldsymbol{R}_i}^{\boldsymbol{R}_f} \boldsymbol{A} \cdot \boldsymbol{dr}. \tag{2.34}$$

This change in phase can be accounted for by performing the so-called Peierls

transformation, $\boldsymbol{p} \to \boldsymbol{p} + e\boldsymbol{A}$.

### 2.4.1 Landau levels in monolayer graphene

In the presence of a magnetic field the low energy Hamiltonian of monolayer graphene, Eq. (2.18), becomes

$$\hat{\boldsymbol{\mathcal{H}}}_{\mathrm{MLG}} = v \begin{pmatrix} 0 & \hat{\boldsymbol{\pi}}^{\dagger} \\ \hat{\boldsymbol{\pi}} & 0 \end{pmatrix}, \tag{2.35}$$

where $\hat{\boldsymbol{\pi}} = (p_x + eA_x) + i(p_y + eA_y)$, acting on the basis $\{A,\, B\}^T$ for the $\boldsymbol{K}_+$ valley and $\{B,\, -A\}^T$ in the $\boldsymbol{K}_-$ valley. The operators $\hat{\boldsymbol{\pi}}$ and $\hat{\boldsymbol{\pi}}^{\dagger}$ become lowering and raising operators, respectively, for functions built of quantum harmonic oscillator states along the $x$-direction, $\phi_n(x)$, and plane waves along the $y$-direction

$$\begin{aligned}
&\hat{\boldsymbol{\pi}}\phi_n(x)e^{ik_y y} = -i\frac{2\hbar}{\lambda_B}\sqrt{n}\phi_{n-1}(x)e^{ik_y y}, \\
&\hat{\boldsymbol{\pi}}^{\dagger}\phi_n(x)e^{ik_y y} = i\frac{2\hbar}{\lambda_B}\sqrt{n+1}\phi_{n+1}(x)e^{ik_y y}, \\
&\phi_n(x) = A_n \exp\left[-\frac{1}{2\lambda_B^2}(x-X)^2\right] \mathcal{H}_n\left(\frac{1}{\lambda_B}(x-X)\right), \\
&A_n = \frac{1}{\sqrt{2^n n!\sqrt{\pi}\lambda_B L}},
\end{aligned} \tag{2.36}$$

where $\lambda_B = \sqrt{\hbar/eB}$ is the magnetic length, $\mathcal{H}_m(x)$ is a Hermite polynomial of order $m$, $L$ is the dimension of the flake along the $y$-direction and $X = \lambda_B^2 k_y$ is the position of the centre of cyclotron orbit of an electron with wave vector $k_y$. The resulting energy levels in MLG are

$$\begin{aligned}
&\varepsilon_0 = 0, \\
&\varepsilon_{n,s'} = s'\left(\sqrt{2}v\hbar/\lambda_B\right)\sqrt{n}, \qquad\qquad n \geq 1,
\end{aligned} \tag{2.37}$$

where $s' = \pm 1$ is the conduction/valence band index in MLG, defined when $n \geq 1$. The magnetic field dependence of these Landau levels is shown in Fig. 2.5 (b). The wave function corresponding to the $n$-th Landau level in MLG can be written

as

$$\psi_0 = \begin{pmatrix} \phi_0 \\ 0 \end{pmatrix} e^{ik_y y},$$
$$\psi_{n,s'} = \frac{1}{\sqrt{2}} \begin{pmatrix} \phi_n \\ -s' i \phi_{n-1} \end{pmatrix} e^{ik_y \cdot y}, \qquad n \geq 1. \tag{2.38}$$

In MLG, all the Landau levels have an additional four-fold degeneracy due to spin and valley. Moreover, the $n = 0$ Landau level is positioned at the Dirac point and its energy does not depend on the magnetic field.

### 2.4.2 Landau levels in bilayer graphene

In the presence of a perpendicular magnetic field, the low-energy effective two band model for Bernal bilayer graphene, Eq. (2.32), becomes

$$\hat{\boldsymbol{\mathcal{H}}}_{\text{eff,BLG}} = -\frac{v^2}{\gamma_1} \begin{pmatrix} 0 & (\hat{\boldsymbol{\pi}}^\dagger)^2 \\ \hat{\boldsymbol{\pi}}^2 & 0 \end{pmatrix} + \hat{\boldsymbol{h}}_u, \tag{2.39}$$
$$\hat{\boldsymbol{h}}_u = \frac{\xi u}{2} \begin{pmatrix} 1 & 0 \\ 0 & -1 \end{pmatrix} + \frac{\xi u v^2}{\gamma_1^2} \begin{pmatrix} \hat{\boldsymbol{\pi}}^\dagger \hat{\boldsymbol{\pi}} & 0 \\ 0 & \hat{\boldsymbol{\pi}} \hat{\boldsymbol{\pi}}^\dagger \end{pmatrix},$$

written in the basis $\{A1,\, B2\}^T$ in $\boldsymbol{K}_+$ and $\{B2,\, A1\}^T$ in $\boldsymbol{K}_-$ [23]. The square dependence on the raising and lowering operators in Eq. (2.39) means that the resulting energy levels scale differently in Landau level index than in monolayer graphene. Using Eq. (2.36), the energies of the BLG Landau levels, can be expressed as [23]

$$\varepsilon_{0,\xi} = \frac{\xi u}{2},$$
$$\varepsilon_{1,\xi} = \frac{\xi u}{2} - \xi \eta^2 u, \tag{2.40}$$
$$\varepsilon_{m,s,\xi} = -\frac{\eta^2 \xi u}{2} + s\sqrt{(\varepsilon_m^0)^2 + \frac{1}{4}u^2}, \qquad m \geq 2,$$

where $\eta = \sqrt{2} v\hbar/\lambda_B \gamma_1$, $\varepsilon_m^0 = \gamma_1 \eta^2 \sqrt{m(m-1)}$ and $s = \pm 1$ is the conduction/valence band index in BLG, defined when $m \geq 2$. In Fig. 2.6, we present the Landau level spectra in Bernal bilayer graphene, where $u = 0$ meV (a) and $u = 100$ meV (b), as a function of the applied magnetic field. The corresponding

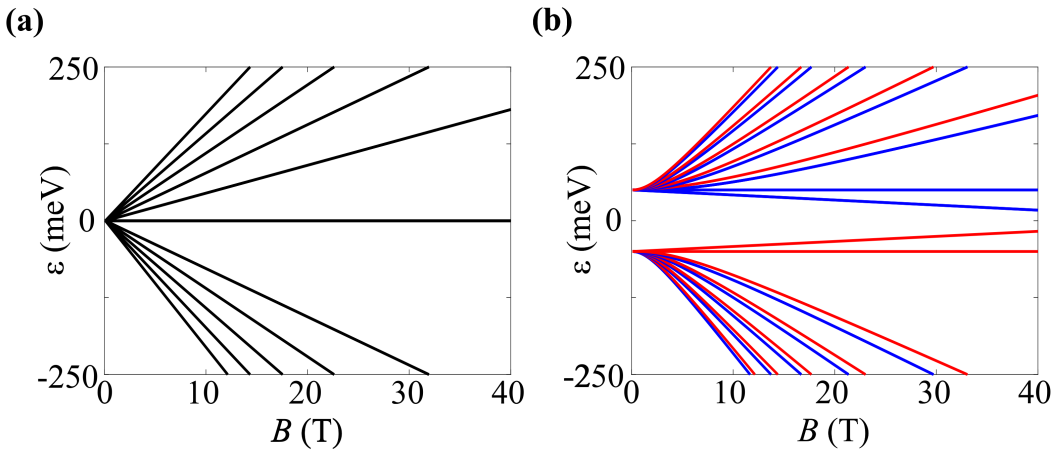


**Figure 2.6:** (a) Landau level spectrum of Bernal bilayer graphene as a function of applied magnetic field. (b) Landau level spectrum of Bernal bilayer graphene as a function of applied magnetic field in the presence of a perpendicular electric field, leading to an on-site energy difference of $u = 100$ meV. This non-zero $u$ leads to the lifting of valley degeneracy with $\boldsymbol{K}_+$( $\boldsymbol{K}_-$) shown in blue (red).

wave functions are

$$\begin{aligned}
\psi_0 &= \begin{pmatrix} \phi_0 \\ 0 \end{pmatrix} e^{ik_y y}, \\
\psi_1 &= \begin{pmatrix} \phi_1 \\ 0 \end{pmatrix} e^{ik_y y}, \\
\psi^{\xi}_{m,s} &= \frac{1}{\sqrt{2C}} \begin{pmatrix} C_1 \phi_m \\ C_2 \phi_{m-2} \end{pmatrix} e^{ik_y y}, \qquad m \geq 2, \\
C_1 &= \varepsilon^0_m, \quad C_2 = \left[ \varepsilon_{m,s,\xi} - \xi \frac{u}{2} + \xi u m \eta^2 \right],
\end{aligned} \tag{2.41}$$

where $C = C_1^2 + C_2^2$ is the normalisation constant. In BLG, for $u = 0$, in addition to the valley and spin degeneracies of each level, both the $m = 0$ and $m = 1$ Landau levels sit at the neutrality point, leading to an unusual eight-fold degenerate zero-energy state. Non-zero $u$ lifts both the $m = 0, 1$ and valley degeneracies, as shown in Fig. 2.6 (b).

# Chapter 3

# Moiré patterns in two-dimensional crystals

## 3.1 Geometry of moiré superlattices

The stacking of two-dimensional crystals with the same Bravais lattice structure can lead to a new large scale periodicity [54, 55, 56]. In particular, if the layers are misaligned or if the lattice constants differ, the periodic beating of the two small-scale unit cells can give rise to a larger scale periodicity known as a supercell. The resulting crystalline structure is known as a moiré superlattice. In this chapter, we seek to derive the electronic properties of three graphene-based moiré superlattices: twisted bilayer graphene, graphene on hBN and graphene on $\alpha - In_2Te_2$.

The $i$th lattice vector, $\boldsymbol{a_i}$ and $\boldsymbol{a_i'}$, in the top and bottom layers respectively, are related by

$$\boldsymbol{a_i'} = (1+\delta)\hat{\boldsymbol{R}}_\theta \boldsymbol{a_i}, \tag{3.1}$$

where $\delta$ is the difference between the lattice constants in the two materials and $\hat{\boldsymbol{R}}_\theta$ is the anticlockwise rotation operator about the $z$-axis by misalignment angle, $\theta$. The size of this large scale periodicity is obvious if the two materials are commensurate, or in other words, $\exists n, m \in \mathbb{Z}^* : n\boldsymbol{a_i'} = m\boldsymbol{a_i}$. Unfortunately, as with many constants in nature, it is unlikely that $\delta$ and $\hat{\boldsymbol{R}}_\theta$ are rational. Therefore it is necessary to approximate most of these supercells as "almost-commensurate" which relies on the observation that at small deviations away from a commensurate structure, the physics should not be significantly different [57], allowing an approximate periodicity to be defined (note that the models we use do not actually require commensuration). In a similar way to Eq. (3.1), we can relate the reciprocal lattice vectors,

$$\boldsymbol{G_i'} = \frac{1}{1+\delta}\hat{\boldsymbol{R}}_\theta \boldsymbol{G_i}. \tag{3.2}$$

The superlattice reciprocal lattice vector is smaller than the normal reciprocal lattice vector as the real-space superlattice cell is larger. By considering the relative beating of these periodicities, the reciprocal superlattice vectors can be written as [57]

$$\boldsymbol{G_i^M} = \boldsymbol{G_i} - \boldsymbol{G_i'} = \left(1 - \frac{1}{1+\delta}\hat{\boldsymbol{R}}_\theta\right)\boldsymbol{G_i}, \tag{3.3}$$

which define a new effective Brillouin zone, known as the superlattice Brillouin zone (sBZ). From this, an approximate real space superlattice vector, $\boldsymbol{a_m}$, is

defined in the usual way, however the length $|\boldsymbol{a_m}|$ is not equivalent to the true superlattice vector which describes exact translational symmetry in the crystal (which may or may not exist, depending on whether the system is commensurate or not).

In the rest of the chapter we do not make any assumptions as to whether or not the modelled stucture is commensurate, as the derivation of these models does not actually require exact commensuration[1] (or the perturbation from one). As a result, the twist angle and lattice constant mismatch become variables that can be continuously varied without having to change any other input parameters.

## 3.2 Twisted bilayer graphene

Bilayer graphene, in the typical Bernal stacking, was discussed in Section 2.3. However, through advancement in fabrication techniques, it is now possible to stack graphene layers at arbitrary twist angles to one another, as shown in Fig. 3.1, into what is known as twisted bilayer graphene (tBLG) [28, 58, 59, 60, 61, 62, 63, 64, 65].

These tBLG structures belong to one of two families, commensurate and incommensurate, depending on the rotation angle. Many theoretical works discuss the electronic properties of tBLG at commensurate angles [66, 67, 68, 69, 70], as there is true translational invariance which allows a tight-binding model, similar to those discussed in the previous sections, to be formulated. Unfortunately, this subset of angles is much smaller than for incommensurate angles. Furthermore the vastly increased size of the superlattice unit cell (Fig. 3.1 (a)) means that the number of atoms becomes unmanageably large for real-space calculations. Instead, this section will focus on deriving a tBLG Hamiltonian for arbitrary incommensurate angles [71].

The interlayer interaction between twisted graphene layers at arbitrary twist angles can be described using the continuum model. The continuum model, although derived rigorously in this chapter, can be understood in a qualitative way. When two graphene layers are misaligned and placed on top of each other, a rough, pseudo-periodicity can be observed. In particular, regions of close alignment can be seen, where over several graphene unit cells, certain sublattices are approximately on top of each other forming areas of $AB$, $BA$ and $AA$ stacking.

[1] Note that, in the models for hBN and $In_2Te_2$, changing the lattice constants away from more commensurate structures would diminish the effect of the moiré pattern as expected, however the theory holds for a range of lattice constants and angles, irrespective how close to a commensurate structure they are.

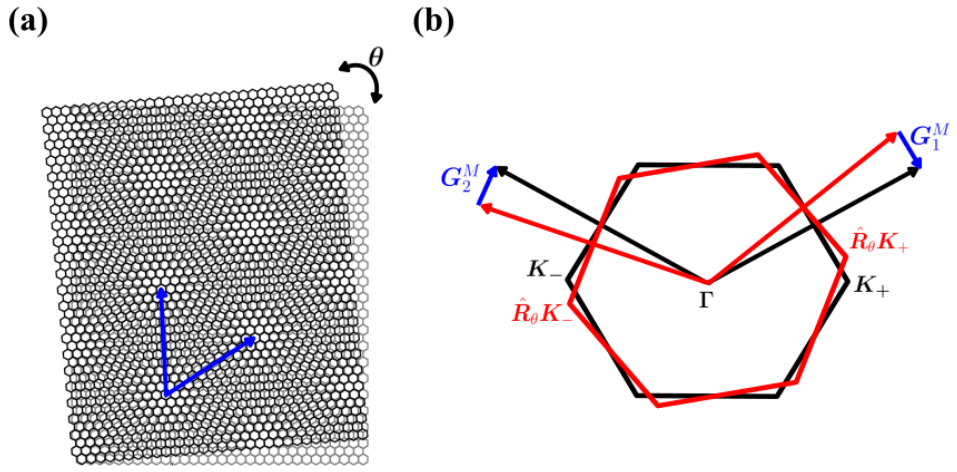


**Figure 3.1:** (a) Crystal structure of two stacked monolayer graphene sheets misaligned by angle $\theta$. The resulting moiré pattern has a new large scale periodicity, marked by blue arrows. (b) The corresponding relative Brillouin zone rotation as a result of real space misalignment shown with black (reference layer) and red (rotated layer) hexagons. The corresponding reciprocal lattice vectors are shown with black and red arrows respectively, while the blue arrows represent the reciprocal superlattice vectors, $\boldsymbol{G}_1^M$ and $\boldsymbol{G}_2^M$.

Across these regions the interlayer couplings can be approximately described using those typically utilised to model $AB$, $BA$ and $AA$ bilayers. However, in the areas between these regions, we approximate using a smooth continuous function to indicate the smoothly varying coupling between the $AB$, $BA$ and $AA$ regions. This assumed continuum, in the description of this coupling, gives rise to the name continuum model.

In the notation outlined in the the previous section, the moiré reciprocal superlattice vector in twisted bilayer graphene, shown in Fig. 3.1 (b), is

$$\boldsymbol{G_i^M} = (\hat{\boldsymbol{R}}_{-\frac{\theta}{2}} - \hat{\boldsymbol{R}}_{\frac{\theta}{2}})\boldsymbol{G_i}, \tag{3.4}$$

where $\delta$ has been set to zero and the misalignment by angle $\theta$ is accounted for by opposite $\frac{\theta}{2}$ rotations to both layers. Although not representing true periodicity, we can use these superlattice vectors to construct a superlattice Brillouin zone (sBZ). The relative rotational misalignment of the graphene sheets leads to an identical rotation in the BZs of the respective layers about the Γ-point. This rotation leads to a non-zero offset between equivalent valleys in the layers, $\boldsymbol{q_\xi} = (\hat{\boldsymbol{R}}_{-\frac{\theta}{2}} - \hat{\boldsymbol{R}}_{\frac{\theta}{2}})\boldsymbol{K_\xi}$. The hexagonal sBZ is positioned such that it contains exactly one valley point

from both layers.

Similarly to Bernal bilayer graphene, twisted bilayer can be described in terms of intralayer and interlayer interactions

$$\hat{\boldsymbol{H}}_{\mathrm{tBLG}}(\theta) = \begin{pmatrix} \hat{\boldsymbol{H}}_{\mathrm{MLG}}\left(\frac{-\theta}{2}\right) & \hat{\boldsymbol{T}}(\theta) \\ \hat{\boldsymbol{T}}^{\dagger}(\theta) & \hat{\boldsymbol{H}}_{\mathrm{MLG}}\left(\frac{\theta}{2}\right) \end{pmatrix}. \tag{3.5}$$

The intralayer part, $\hat{\boldsymbol{H}}_{\mathrm{MLG}}(\phi)$, is the typical monolayer graphene Hamiltonian, Eq. (2.14), with the centre of coordinates reference rotated by angle $\phi$. Although the effective linear dispersion, $\hat{\boldsymbol{\mathcal{H}}}_{\mathrm{MLG}}$ could be utilised here, at large angles the Dirac cones become significantly displaced such that the true band structure becomes non-linear where important features occur. The interlayer part, $\hat{\boldsymbol{T}}(\theta)$, describes hopping between the graphene monolayers and therefore should conserve momentum in both layers. For momentum $\boldsymbol{k}$ and $\overline{\boldsymbol{k}}$ on layers 1 and 2 of tBLG respectively, this conservation can be expressed as

$$\boldsymbol{G} + \boldsymbol{k} = \overline{\boldsymbol{G}} + \overline{\boldsymbol{k}}, \tag{3.6}$$

where $\boldsymbol{G} = m_1\boldsymbol{G_1} + m_2\boldsymbol{G_2}$ and $\overline{\boldsymbol{G}} = \overline{m_1}\overline{\boldsymbol{G}}_{\boldsymbol{1}} + \overline{m_2}\overline{\boldsymbol{G}}_{\boldsymbol{2}}$ are the reciprocal lattice vectors on layers 1 and 2 respectively. This expression follows from the Bloch nature of states on the two layers. The positions of the $l$th and $m$th sublattices in layer 1 and 2 respectively can be expressed as

$$\begin{aligned} \boldsymbol{R}_l &= n_1\boldsymbol{a_1} + n_2\boldsymbol{a_2} + \boldsymbol{\tau}_l, \\ \overline{\boldsymbol{R}}_m &= \overline{n}_1\hat{\boldsymbol{R}}_{\boldsymbol{\theta}}\boldsymbol{a_1} + \overline{n}_2\hat{\boldsymbol{R}}_{\boldsymbol{\theta}}\boldsymbol{a_2} + \overline{\boldsymbol{\tau}}_m, \end{aligned} \tag{3.7}$$

where $n_1, n_2, \overline{n}_1, \overline{n}_2 \in \mathbb{Z}$ and $\boldsymbol{\tau}_l$ ($\overline{\boldsymbol{\tau}}_m$) represents the vector from the real space origin in the unit cell to the nearest orbital $l(m)$ in the bottom (top) layer. The definition of these vectors depends on the centre of coordinates, here defined as an A atom on the top layer and a B atom on the bottom layer. This ensures that under zero rotation between the two graphene sheets, Bernal bilayer graphene is recovered. Hence, $\boldsymbol{\tau}_l$ and $\overline{\boldsymbol{\tau}}_m$ can be defined as follows

$$\begin{aligned} \boldsymbol{\tau}_A &= -\boldsymbol{\delta_1}, \quad \boldsymbol{\tau}_B = 0, \\ \overline{\boldsymbol{\tau}}_A &= 0, \quad \overline{\boldsymbol{\tau}}_B = \boldsymbol{\delta_1}. \end{aligned} \tag{3.8}$$

The interlayer interaction between layers in twisted bilayer can be written as

$$T = \sum_{l,m} t(\overline{\boldsymbol{R}}_m - \boldsymbol{R}_l, d_0) \left|\psi_l(\boldsymbol{r} - \boldsymbol{R}_l)\right\rangle \left\langle\psi_m(\boldsymbol{r} - \overline{\boldsymbol{R}}_m)\right| + h.c., \tag{3.9}$$

where $t(\boldsymbol{R}, d_0)$ describes the interaction between two $p_z$ orbitals separated by in-plane vector $\boldsymbol{R}$ and interlayer distance $d_0$ while $|\psi_j(\boldsymbol{r} - \boldsymbol{R}_j)\rangle$ describes the atomic orbital $j$ at position $\boldsymbol{R}_j$. Unlike in monolayer and Bernal bilayer graphene, where such an interaction term would allow the construction of a simple tight-binding Hamiltonian, the large number of orbitals in the twisted bilayer unit cell encourages an alternative approach [71, 72, 73]. In particular by working in reciprocal space (and thus the much smaller sBZ), we can write the Bloch states of the individual layers as

$$|\boldsymbol{k}, l\rangle = \frac{1}{\sqrt{N}} \sum_{\boldsymbol{R}_l} e^{i\boldsymbol{k}\cdot\boldsymbol{R}_l} \left|\psi_l(\boldsymbol{r} - \boldsymbol{R}_l)\right\rangle, \tag{3.10}$$

$$|\overline{\boldsymbol{k}}, m\rangle = \frac{1}{\sqrt{\overline{N}}} \sum_{\overline{\boldsymbol{R}}_m} e^{i\overline{\boldsymbol{k}}\cdot\overline{\boldsymbol{R}}_m} \left|\psi_m(\boldsymbol{r} - \overline{\boldsymbol{R}}_m)\right\rangle, \tag{3.11}$$

where $N$ and $\overline{N}$ are the number of unit cells of area $A$ and $\overline{A}$ respectively such that $NA = \overline{NA} = A_{\text{tot}}$ is roughly the total area of the twisted bilayer region. Although the two layers need not be commensurate, this normalises the Bloch wavefunctions to a good approximation provided $A_{\text{tot}}$ is large. The interaction between the Bloch states of any two orbitals is therefore

$$\begin{aligned}
\hat{\boldsymbol{T}}_{m,l}(\theta) = \hat{\boldsymbol{T}}_{m,l}(\overline{\boldsymbol{k}}, \boldsymbol{k}) &= \langle\overline{\boldsymbol{k}}, m| \, T \, |\boldsymbol{k}, l\rangle \\
&= \frac{1}{\sqrt{N\overline{N}}} \sum_{\boldsymbol{R}_l, \overline{\boldsymbol{R}}_m} t(\overline{\boldsymbol{R}}_m - \boldsymbol{R}_l, d_0) \, e^{i(\boldsymbol{k}\cdot\boldsymbol{R}_l - \overline{\boldsymbol{k}}\cdot\overline{\boldsymbol{R}}_m)} \\
&= \frac{1}{\sqrt{N\overline{N}}} \sum_{\boldsymbol{R}_l} e^{i(\boldsymbol{k}-\overline{\boldsymbol{k}})\cdot\boldsymbol{R}_l} \sum_{\overline{\boldsymbol{R}}_m} t(\overline{\boldsymbol{R}}_m - \boldsymbol{R}_l, d_0) e^{-i\overline{\boldsymbol{k}}\cdot(\overline{\boldsymbol{R}}_m - \boldsymbol{R}_l)}.
\end{aligned} \tag{3.12}$$

To express this interaction, $t(\boldsymbol{R}_l - \overline{\boldsymbol{R}}_m, d_0)$, in reciprocal space, it is necessary to take the inverse Fourier transform

$$t(\overline{\boldsymbol{R}}_m - \boldsymbol{R}_l, d_0) = \frac{A_{\text{tot}}}{\sqrt{N\overline{N}}} \int \tilde{t}(\boldsymbol{q}, d_0) e^{i\boldsymbol{q}\cdot(\overline{\boldsymbol{R}}_m - \boldsymbol{R}_l)} dq_x dq_y, \tag{3.13}$$

such that $\tilde{t}(\boldsymbol{q}, d_0)$ is the interlayer coupling between orbitals as a function of

$\boldsymbol{q} = (q_x, q_y)$. This allows the interaction element to be written as

$$\begin{aligned}\hat{\boldsymbol{T}}_{m,l}(\theta) &= \frac{A_{\text{tot}}}{N\overline{N}} \sum_{\boldsymbol{R}_l} e^{i(\boldsymbol{k}-\overline{\boldsymbol{k}})\cdot\boldsymbol{R}_l} \sum_{\overline{\boldsymbol{R}}_m} \int \tilde{t}(\boldsymbol{q}, d_0) e^{i\boldsymbol{q}\cdot(\overline{\boldsymbol{R}}_m - \boldsymbol{R}_l)} dq_x dq_y e^{-i\overline{\boldsymbol{k}}\cdot(\overline{\boldsymbol{R}}_m - \boldsymbol{R}_l)} \\ &= \sum_{\boldsymbol{G},\overline{\boldsymbol{G}}} \tilde{t}(\boldsymbol{k}+\boldsymbol{G}, d_0) e^{i(\overline{\boldsymbol{G}}\cdot\overline{\boldsymbol{\tau}}_m - \boldsymbol{G}\cdot\boldsymbol{\tau}_l)} \delta_{\boldsymbol{k}+\boldsymbol{G},\overline{\boldsymbol{k}}+\overline{\boldsymbol{G}}}, \end{aligned} \tag{3.14}$$

where, by taking into account the definition of $\overline{\boldsymbol{R}}_m$, the sum over $\overline{\boldsymbol{R}}_m$ was resolved using

$$\sum_{\overline{\boldsymbol{R}}_m} e^{i(\boldsymbol{q}-\overline{\boldsymbol{k}})\cdot\overline{\boldsymbol{R}}_m} = \sum_{n_1,n_2} e^{i(\boldsymbol{q}-\overline{\boldsymbol{k}})\cdot(\overline{n}_1\overline{\boldsymbol{a}}_1 + \overline{n}_2\overline{\boldsymbol{a}}_2)} = \overline{N}\delta_{\boldsymbol{q}-\overline{\boldsymbol{k}},\overline{\boldsymbol{G}}}, \tag{3.15}$$

such that $\delta_{i,j}$ is the Kronecker delta. The same principle was applied to the sum over $\boldsymbol{R}_l$ such that the dependence on $\boldsymbol{q}$ drops out. The interlayer coupling described in Eq. (3.14) can be understood in the following way. Firstly, the Kronecker delta term, $\delta_{\boldsymbol{k}+\boldsymbol{G},\overline{\boldsymbol{k}}+\overline{\boldsymbol{G}}}$, determines the momenta on the bottom and top layers which couple reproducing the relationship in Eq. (3.6). This can also be understood as coupling momenta $\boldsymbol{k}$ and $\overline{\boldsymbol{k}}$ which are offset by a moiré reciprocal lattice vector. The term $e^{i(\overline{\boldsymbol{G}}\cdot\overline{\boldsymbol{\tau}}_m - \boldsymbol{G}\cdot\boldsymbol{\tau}_l)}$ describes the phase factor associated with the coupling of orbitals $l$ and $m$ as a result of translation by reciprocal lattice vector. In the limit of $\theta = 0$, these phases should combine to produce $\gamma_1$ coupling between $\overline{A}$ and $B$ and 0 coupling between other orbitals. Finally, $\tilde{t}(\boldsymbol{k}+\boldsymbol{G}, d_0)$ is the Fourier transform of the real-space interatomic coupling, and depends on the length of reciprocal lattice vector from the Γ-point in layer 1.

A state close to the Dirac point in layer 1 scattered by some reciprocal lattice vector $\boldsymbol{G}$ in layer 1 lands in a different position in the Brillouin zone of layer 2, due to the relative rotation. This can be mapped back onto the first Brillouin zone of layer 2 resulting in a lattice of so-called "Dirac point replicas", each interacting with magnitude $\tilde{t}(\boldsymbol{k}+\boldsymbol{G}, d_0)$. The overall effective Hamiltonian for twisted bilayer graphene can be found by summing over all countably infinite $\boldsymbol{G}$ and $\overline{\boldsymbol{G}}$. However this is both impossible and unnecessary. In fact, due to the exponential decay of $\tilde{t}(\boldsymbol{q}, d_0)$, only nearest neighbours in this lattice of Dirac point replicas interact strongly, while the total number of replicas needed to reach convergence depends on the size of $\boldsymbol{G}^{\boldsymbol{M}}$ [73]. Due to the decay of $\tilde{t}(\boldsymbol{q}, d_0)$, of the seven smallest reciprocal lattice vectors $\boldsymbol{G}$, only 3 interact strongly with the Dirac point in the first Brillouin zone. These vectors are those which connect valleys in the first Brillouin zone of layer 1 such that the distance from the Γ point is approximately equal $|\boldsymbol{K}_{\boldsymbol{\xi}}|$. Therefore we perform the sum for $(m_1, m_2) = \{(0,0), (-1,0), (0,1)\}$,

so that, for an electron with momentum $\boldsymbol{k}+\boldsymbol{K_\xi}$ in layer 1, the interaction with three nearest Dirac cone replicas in layer 2, can be written as

$$\begin{aligned}\hat{\boldsymbol{T}}_{m,l}(\theta) = &\tilde{t}(\boldsymbol{k}+\boldsymbol{K_\xi}, d_0)\delta_{\boldsymbol{k}+\boldsymbol{q_\xi},\boldsymbol{k}} \\ &+ \tilde{t}(\boldsymbol{k}-\boldsymbol{G_1}+\boldsymbol{K_\xi}, d_0)e^{i(-\overline{\boldsymbol{G}}_{\boldsymbol{1}}\cdot\overline{\boldsymbol{\tau}}_m+\boldsymbol{G_1}\cdot\boldsymbol{\tau}_l)}\delta_{\boldsymbol{k}-\boldsymbol{G}_{\boldsymbol{1}}^{\boldsymbol{M}}+\boldsymbol{q_\xi},\boldsymbol{k}} \\ &+ \tilde{t}(\boldsymbol{k}+\boldsymbol{G_2}+\boldsymbol{K_\xi}, d_0)e^{i(\overline{\boldsymbol{G}}_{\boldsymbol{2}}\cdot\overline{\boldsymbol{\tau}}_m-\boldsymbol{G_2}\cdot\boldsymbol{\tau}_l)}\delta_{\boldsymbol{k}+\boldsymbol{G}_{\boldsymbol{2}}^{\boldsymbol{M}}+\boldsymbol{q_\xi},\boldsymbol{k}},\end{aligned} \tag{3.16}$$

which can be written in terms of the basis $\{A, B, \overline{A}, \overline{B}\}$ as

$$\begin{aligned}\hat{\boldsymbol{T}}(\theta) = &\tilde{t}(\boldsymbol{k}+\boldsymbol{K_\xi}, d_0)\begin{pmatrix}1 & 1\\ 1 & 1\end{pmatrix}\delta_{\boldsymbol{k}+\boldsymbol{q_\xi},\boldsymbol{k}} \\ &+ \tilde{t}(\boldsymbol{k}+\boldsymbol{K_\xi}-\boldsymbol{G_1}, d_0)\begin{pmatrix}e^{\frac{2\pi i}{3}} & e^{\frac{-2\pi i}{3}}\\ 1 & e^{\frac{2\pi i}{3}}\end{pmatrix}\delta_{\boldsymbol{k}-\boldsymbol{G}_{\boldsymbol{1}}^{\boldsymbol{M}}+\boldsymbol{q_\xi},\boldsymbol{k}} \\ &+ \tilde{t}(\boldsymbol{k}+\boldsymbol{K_\xi}+\boldsymbol{G_2}, d_0)\begin{pmatrix}e^{\frac{-2\pi i}{3}} & e^{\frac{2\pi i}{3}}\\ 1 & e^{\frac{-2\pi i}{3}}\end{pmatrix}\delta_{\boldsymbol{k}+\boldsymbol{G}_{\boldsymbol{2}}^{\boldsymbol{M}}+\boldsymbol{q_\xi},\boldsymbol{k}}.\end{aligned} \tag{3.17}$$

At low angles, the superlattice Brillouin zone is small hence most electronic behaviour can be described in the vicinity of the $\boldsymbol{K_\xi}$ point. Therefore, the intralayer Hamiltonian can be described in the low-energy limit and since $\boldsymbol{K_\xi} \gg \boldsymbol{k}$ it is reasonable to write $\tilde{t}(\boldsymbol{k}+\boldsymbol{K_\xi}, d_0) = \tilde{t}(\boldsymbol{K_\xi}, d_0) = w = 110$ meV [71, 73]. Therefore, the dominant part of the interlayer component of Eq. (3.5) becomes

$$\begin{aligned}\hat{\boldsymbol{T}}(\theta) \approx &\, w\begin{pmatrix}1 & 1\\ 1 & 1\end{pmatrix}\delta_{\boldsymbol{k}+\boldsymbol{q_\xi},\boldsymbol{k}} + w\begin{pmatrix}e^{\frac{2\pi i}{3}} & e^{\frac{-2\pi i}{3}}\\ 1 & e^{\frac{2\pi i}{3}}\end{pmatrix}\delta_{\boldsymbol{k}-\boldsymbol{G}_{\boldsymbol{1}}^{\boldsymbol{M}}+\boldsymbol{q_\xi},\boldsymbol{k}} \\ &+ w\begin{pmatrix}e^{\frac{-2\pi i}{3}} & e^{\frac{2\pi i}{3}}\\ 1 & e^{\frac{-2\pi i}{3}}\end{pmatrix}\delta_{\boldsymbol{k}+\boldsymbol{G}_{\boldsymbol{2}}^{\boldsymbol{M}}+\boldsymbol{q_\xi},\boldsymbol{k}},\end{aligned} \tag{3.18}$$

where the $\theta$ dependence is contained in $\boldsymbol{q_\xi}$. This value of $w$ has been estimated from experiment [28, 58]. The resulting band structure is shown in Fig. 3.2 (a) for misalignment angle 2°. Over the first superlattice Brillouin zone, the band structure comprises two Dirac cones, one from each layer, separated by distance $\boldsymbol{q_\xi}$. At the point where the two cones cross, band hybridisation leads to band splitting and repulsion, with separation determined by the size of $w$ (or for larger angles $\tilde{t}(\boldsymbol{k}+\boldsymbol{K_\xi}, d_0)$). As the angle is reduced the cones move closer together such that at a certain angle, commonly referred to as the magic angle [70, 73], the band becomes maximally flat, as shown in Fig. 3.2 (b). This flatness of a band with energy $E$ can be quantised using the effective Fermi velocity, $v = \dfrac{1}{\hbar}\dfrac{\partial E}{\partial \boldsymbol{k}}$, which is a minimum at the magic angle. The first magic angle in our model is approximately

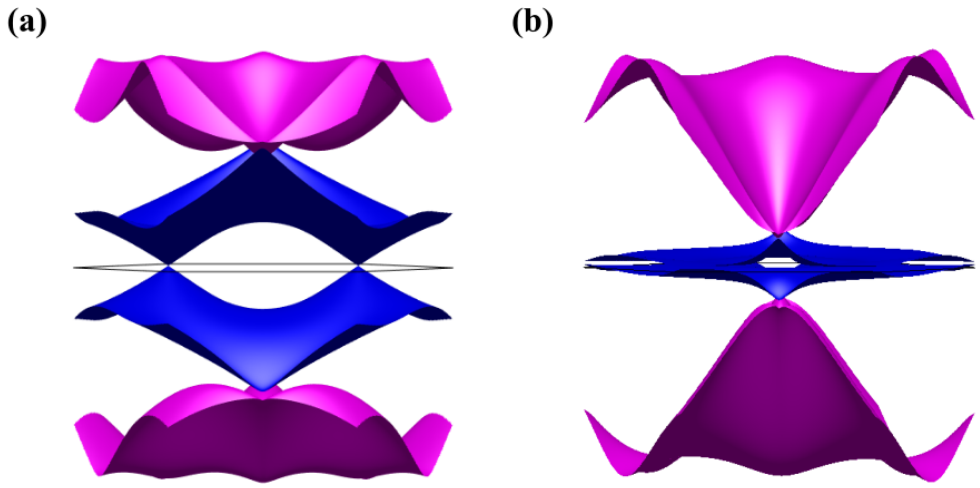


**Figure 3.2:** (a) Electronic band structure of twisted bilayer graphene with misalignment angle 2°. (b) Electronic band structure of twisted bilayer graphene at misalignment angle 1.1°, the magic angle. The superlattice Brillouin zone is shown by a black hexagon. We show only the two lowest energy conduction and valence bands for clarity.

1.1°. Interestingly, as the twist angle is reduced below the magic angle, the flat band begins to broaden again, suggesting the magic angle is particularly unique. This flat band is associated with real-space localisation of electrons to regions of AA type stacking [70] bounded by walls of AB and BA alignment.

An interesting question would be on the validity of the continuum model at zero twist angle, which, in our case, should describe Bernal bilayer graphene. Of course, experimentally, samples with twist angles very close to but not zero are unstable and Bernal bilayer is formed which explains the lack of theoretical and certainly experimental literature on tBLG close to this limit. However, a good test of the continuum model is to ensure that it can reproduce the interlayer coupling in aligned layers. At $\theta = 0$, the sets of Dirac cones originating from both layers lie directly on top of each other and the interaction strength becomes a sum over all $\boldsymbol{G}$. This will be discussed in far more detail in Chapter 5 where we use this limit as a test of our parametrisation.

In a similar way to Bernal bilayer, the application of an electric field perpendicular to the graphene layers leads to an on-site energy difference between the graphene layers, $u$. However, unlike in Bernal bilayer, this on-site energy difference shifts the relative position of the Dirac cones in energy rather than inducing a gap.

Although we briefly refer to the parametrisation of the interlayer coupling

between twisted graphene layers in our definition of $\omega$, the ideal functional form of $t(\boldsymbol{R})$ is widely debated [71, 74, 75, 76].While most works agree on the value of $\omega$, the hopping parameters outlined in Section 2.3 are sometimes not reproduced [71] while the decay rate of $t(\boldsymbol{R})$ varies between parametrisations, which could have particular relevance to ARPES maps on twisted bilayer at a 30° misalignment angle [77]. Furthermore, the rate of decay of $t(\boldsymbol{R})$ effects the value of the interlayer coupling in the zero angle limit. Proposing an accurate parametrisation which describes the interlayer coupling in both aligned and twisted bilayer graphene is the basis of Chapter 5.

## 3.3 Graphene-based van der Waals heterostructures

The advancement of fabrication techniques has enabled the isolation of additional species of two-dimensional crystals other than graphene [26, 27]. Furthermore, due to the stability of these two-dimensional materials, these layers can be stacked in arbitrary order and misalignment [78]. These layers, which interact only through weak van der Waals forces, are known as van der Waals (vdW) heterostructures [26, 27]. Although the van der Waals interactions are weak, the band structures of the constituent layers can be significantly changed due to the proximity of another layer. This property is unique to low dimensional materials as in stacked bulk materials only the surface states are strongly modified by proximity to another material. This section will focus on deriving the electronic band structure of monolayer graphene when placed on top of a) hBN and b) $\alpha$ - $In_2Te_2$, however the models derived are easily extended to other materials with a similar crystallographic structure.

### 3.3.1 Graphene on hBN

Graphene and hexagonal boron nitride (hBN) have very similar crystallographic structures [17, 54, 55, 56, 57]: both form a 2D honeycomb structure defined by a triangular lattice of two atom unit cells, with the lattice constants of both materials differing only by $\delta = 1.8\%$. Despite this, they exhibit strikingly different electronic properties, with hBN being a strong in-plane and out-of-plane insulator with a band gap of $\sim 6$ eV. This insulating property, and the fact that it is atomically flat, singles hBN out as an ideal substrate for graphene materials [17, 79]. In other bulk substrates, such as $SiO_2$, surface roughness leads to the

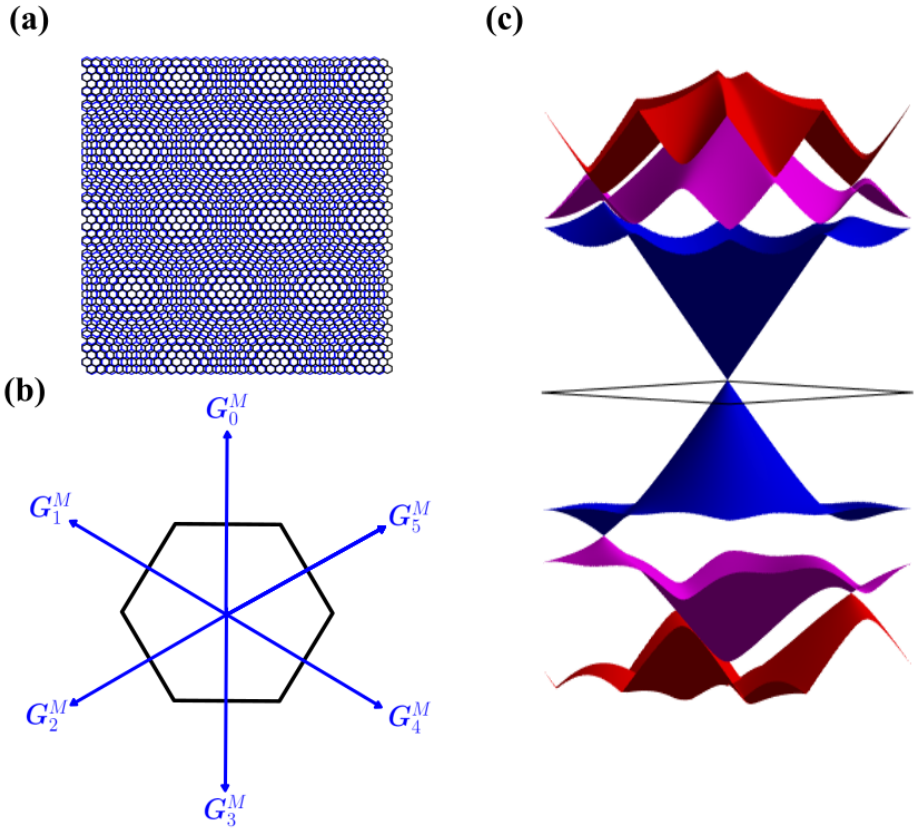


**Figure 3.3:** (a) Moiré pattern arising as a result of aligned graphene and hBN heterostructure. (b) Superlattice Brillouin zone (black hexagon) and first star of reciprocal lattice vectors $\boldsymbol{G}_j^M$ (blue arrows) where $j = \{0, 1, ...5\}$. (c) Resulting band structure of graphene on aligned ($\theta = 0°$) hBN. A rhombic superlattice Brillouin zone (black rhombus) is used to best capture the secondary Dirac point. We show only the three lowest energy conduction and valence bands for clarity.

aggregation of charge pockets, modifying the electronic and transport properties of graphene [80]. In fact, it has been shown that graphene on hBN exhibits charge transport properties more similar to that of suspended graphene than graphene on other substrates such as $SiO_2$ [17].

Large scale moiré patterns ($\sim$ 10 nm) form when graphene is placed on top of closely aligned hBN [54, 55, 56, 57], with the largest superlattice periodicity occurring at perfect alignment [57] as shown in Fig. 3.3 (a). As with twisted bilayer, the Hamiltonian can be described in terms of intralayer and interlayer parts. However, since hBN is an insulator and this thesis focuses on low-energy properties of graphene, it is convenient to treat the effect of hBN as a perturbation [57]. We briefly outline a twisted bilayer type model for graphene on hBN in

Appendix 3.A

To describe the perturbation, it is first necessary to define the eigenstate. Typically, the basis used for the $\boldsymbol{K}_+$ valley is $\{A, B\}$, while in the $\boldsymbol{K}_-$ valley $\{B, -A\}$, hence in valley-sublattice space this can be written as $\{A_+, B_+, B_-, -A_-\}$. The set of Pauli matrices on the sublattice and valley space can be written as $\hat{\boldsymbol{\tau}}_i$ and $\hat{\boldsymbol{\sigma}}_j$ respectively ($i, j \in \{0, x, y, z\}$). In valley sublattice space, these operators can be expressed as a Kronecker product $\hat{\boldsymbol{\tau}}_i \otimes \hat{\boldsymbol{\sigma}}_j$. In principle, the moiré perturbation of graphene by hBN could depend on any one of these operators, however, using symmetry arguments, this can be reduced. Firstly, in an aligned graphene-hBN heterostructure, the reciprocal superlattice vector can be defined using Eq. (3.3)

$$\boldsymbol{G}_{\boldsymbol{j}}^{\boldsymbol{M}} \approx \left(1 - \frac{1}{1+\delta}\right) \boldsymbol{G}_{\boldsymbol{j}}, \tag{3.19}$$

which, for graphene on aligned hBN, is significantly smaller than the intervalley separation in unperturbed monolayer graphene. Furthermore, it has been shown that higher order harmonics (multiple $\boldsymbol{G}_{\boldsymbol{j}}^{\boldsymbol{M}}$) have less effect on the perturbation [57]. The reason for this can be related to the discussion of the two-centre approximation in twisted bilayer, namely that for overlapping $p_z$ orbitals, the Fourier transform of interaction decays exponentially. This results in higher order harmonics being neglected such that only the first star of reciprocal superlattice vectors (Fig. 3.3 (b))

$$\boldsymbol{G}_{\boldsymbol{j}}^{\boldsymbol{M}} = \hat{\boldsymbol{R}}_{\frac{2\pi j}{3}}(0,\ |\boldsymbol{G}^{\boldsymbol{M}}|), \qquad j = \{0, ..., 5\}, \tag{3.20}$$

needs to be considered while valley mixing due to the perturbation of hBN is highly unlikely. The restriction to single harmonics essentially "decouples" the valleys in graphene on hBN. The latter point can be used to immediately cut the set of operators, $\hat{\boldsymbol{\tau}}_i \otimes \hat{\boldsymbol{\sigma}}_j$, in half, as those containing valley mixing terms, $\hat{\boldsymbol{\tau}}_x$ and $\hat{\boldsymbol{\tau}}_y$, can be neglected. The perturbation should also obey time reversal symmetry [81], which can be thought of as valley reversal symmetry $E(\boldsymbol{k}+\boldsymbol{K}_+) \to E(-\boldsymbol{k}+\boldsymbol{K}_-)$. In particular, time reversal symmetry projects a state $\{A_+, B_+, B_-, -A_-\}$ onto $\{-A_-, -B_-, -B_+, A_+\}$ such that for the symmetry operator $\hat{\boldsymbol{X}}$, the generator, t is defined as

$$t = \begin{pmatrix} 0 & 0 & 0 & 1 \\ 0 & 0 & -1 & 0 \\ 0 & -1 & 0 & 0 \\ 1 & 0 & 0 & 0 \end{pmatrix}. \tag{3.21}$$

For an arbitrary symmetry operator, $\hat{\boldsymbol{U}}$, with generator $u$, the symmetry is conserved if the Hamiltonian obeys the relation [82]

$$\hat{\boldsymbol{U}}\hat{\boldsymbol{H}}_{\mathrm{hBN}}(\boldsymbol{r}) = u\hat{\boldsymbol{H}}_{\mathrm{hBN}}(\hat{\boldsymbol{U}}^{-1}\boldsymbol{r})u^{-1} = \hat{\boldsymbol{H}}_{\mathrm{hBN}}(\boldsymbol{r}), \tag{3.22}$$

which for time reversal symmetry can be expressed as

$$\hat{\boldsymbol{X}}\hat{\boldsymbol{H}}_{\mathrm{hBN}}(\boldsymbol{r}) = t\hat{\boldsymbol{H}}^{*}_{\mathrm{hBN}}(\boldsymbol{r})t^{-1} = \hat{\boldsymbol{H}}_{\mathrm{hBN}}(\boldsymbol{r}). \tag{3.23}$$

By neglecting each of the remaining 8 combinations of $\hat{\boldsymbol{\tau}}_i \otimes \hat{\boldsymbol{\sigma}}_j$ which do not obey this symmetry, the remaining terms are $\{\hat{\boldsymbol{\tau}}_0 \otimes \hat{\boldsymbol{\sigma}}_0, \hat{\boldsymbol{\tau}}_z \otimes \hat{\boldsymbol{\sigma}}_z, \hat{\boldsymbol{\tau}}_z \otimes \hat{\boldsymbol{\sigma}}_x, \hat{\boldsymbol{\tau}}_z \otimes \hat{\boldsymbol{\sigma}}_y\}$. The other symmetry present in honeycomb structures is 60° rotational symmetry, characterised by the $\hat{\boldsymbol{C}}_6$ symmetry group, with generator $c_6 = \tau_x \otimes \left(-i\frac{\sqrt{3}}{2} - \frac{1}{2}\sigma_z\right)$. Although the $\boldsymbol{r}$-dependence of the perturbation is not yet known, a set of candidate functions $\{f_j(\boldsymbol{r})\}$, dependent on the simplest harmonics of $\boldsymbol{G^M}$, can be considered such that

$$\hat{\boldsymbol{C}}_6\hat{\boldsymbol{H}}_{\mathrm{hBN}}(r) = c_6\hat{\boldsymbol{H}}_{\mathrm{hBN}}(\hat{\boldsymbol{R}}^{-1}_{\frac{\pi}{3}}\boldsymbol{r})c_6^{-1} = \sum_{i,j}\sum_{l} c_6\hat{\boldsymbol{\tau}}_i \otimes \hat{\boldsymbol{\sigma}}_j f_l(\hat{\boldsymbol{R}}^{-1}_{\frac{\pi}{3}}\boldsymbol{r})c_6^{-1} = \hat{\boldsymbol{H}}_{\mathrm{hBN}}(\boldsymbol{r}), \tag{3.24}$$

where only specific combinations of $i, j, l$ satisfy the above relationship. The final perturbation Hamiltonian for graphene on hBN can therefore be written as,

$$\begin{aligned}\hat{\boldsymbol{H}}_{\mathrm{hBN}}(\boldsymbol{r}) =& V_0(\hat{\boldsymbol{\tau}}_0 \otimes \hat{\boldsymbol{\sigma}}_0)f_1(\boldsymbol{r}) + V_3(\hat{\boldsymbol{\tau}}_z \otimes \hat{\boldsymbol{\sigma}}_z)f_2(\boldsymbol{r}) + \frac{1}{|\boldsymbol{G^M}|}V_1(\hat{\boldsymbol{\tau}}_z \otimes \nabla f_2(\boldsymbol{r}) \cdot \boldsymbol{\sigma}) \\ &+ \frac{1}{|\boldsymbol{G^M}|}V_2(\hat{\boldsymbol{\tau}}_z \otimes [\boldsymbol{l}_z \times \nabla f_2(\boldsymbol{r}) \cdot \boldsymbol{\sigma}]), \end{aligned} \tag{3.25}$$

$$f_1(\boldsymbol{r}) = \sum_{j=0}^{5} e^{i\boldsymbol{G}^{\boldsymbol{M}}_{\boldsymbol{j}}\cdot\boldsymbol{r}}, \qquad f_2(\boldsymbol{r}) = i\sum_{j=0}^{5}(-1)^j e^{i\boldsymbol{G}^{\boldsymbol{M}}_{\boldsymbol{j}}\cdot\boldsymbol{r}}, \tag{3.26}$$

where $\boldsymbol{\sigma} = (\hat{\boldsymbol{\sigma}}_x, \hat{\boldsymbol{\sigma}}_{\boldsymbol{y}}, \hat{\boldsymbol{\sigma}}_{\boldsymbol{z}})$ is the vector of sublattice Pauli matrices, $\boldsymbol{l}_z$ is the unit vector along the z-axis and the set $\{V_0, V_1, V_2, V_3\} = v|\boldsymbol{G_M}|\{u_0, u_1, u_2, u_3\}$ describes the perturbation strength of each term. Since higher order harmonics of $\boldsymbol{G_M}$ are neglected, the sum is restricted to the first star of vectors defined by the set $j = \{0, ..., 5\}$. Experiments [83, 84], as well as other theoretical models [33, 85] predict the set of parameters to be approximately $\{u_0, u_1, u_2, u_3\} = \{0.5, -1, 0, -\frac{\sqrt{3}}{2}\}$ where the term involving $u_2$ can be gauged away using the transformation $\psi \to \psi e^{i\tau_z u_2 f_2}$ [57].

As a result of this perturbation, the conical dispersion close to the $\boldsymbol{K_\xi}$ point

is folded into the superlattice Brillouin zone, forming so-called "minibands", with the valence band undergoing starker spectral changes as presented in Fig. 3.3 (c). In particular, a secondary Dirac point (region of linear dispersion) forms between the first and second valence band which is shifted away from the $\boldsymbol{K_\xi}$ point. Furthermore, a region of constant energy forms close to the bottom of the first valence band such that the corresponding density of states shows a sharp peak, known as a Van Hove singularity (VHS). The formation and manipulation of Van Hove singularities by careful construction of moiré superlattice heterostructures is significant in Chapter 6. Finally, it is important to note the utility of this model, which, although currently used to describe graphene on hBN, can be easily extended to graphene on any other almost commensurate 2D hexagonal crystal by tuning $\delta$ and parameters $\{u_0, u_1, u_3\}$.

### 3.3.2 Graphene on $\alpha - \mathbf{In_2Te_2}$

In this section, the perturbation on the electronic spectrum of graphene due to stacking on $\alpha-\mathrm{In_2Te_2}$ is derived. Similar to hBN, $\alpha-\mathrm{In_2Te_2}$ has a 2D honeycomb structure and is a wide band gap insulator [86, 87], however the lattice constant is approximately $\sqrt{3}$ times larger. As such, $\alpha - \mathrm{In_2Te_2}$ is classed as an almost-commensurate $\sqrt{3} \times \sqrt{3}$ substrate as compared to graphene. The corresponding moiré pattern is shown in Fig. 3.4 (a).

The lattice constant of an almost-commensurate $\sqrt{3}\times\sqrt{3}$ crystal, is written as $a_{\sqrt{3}} = \sqrt{3}(1+\delta)a$ where $|\delta| \ll 1$ [34, 35]. As such, the corresponding superlattice, analogous to Eq. (3.3) has reciprocal lattice vectors of the form

$$\boldsymbol{G_j^M} = \hat{\boldsymbol{R}}_{\frac{2\pi j}{3}} \left[1 - \frac{1}{1+\delta}\hat{\boldsymbol{R}}_\theta\right](0, |\boldsymbol{G}|), \tag{3.27}$$

where much like the hBN case, only the lowest order harmonics are considered and the perturbation Hamiltonian derived for hBN can be utilised, albeit with different perturbation parameters. The corresponding reciprocal superlattice vectors are shown in Fig. 3.4 (b). However, in a graphene - $\sqrt{3} \times \sqrt{3}$ superlattice, there exists another set of shorter reciprocal lattice vectors corresponding to a longer real space periodicity, shown as a blue arrow in Fig. 3.4. Rather than comparing to the true graphene lattice, the $\alpha - \mathrm{In_2Te_2}$ can be compared to the so-called "Kekule" lattice of graphene [88], shown in red in Fig. 3.4 (a) with lattice constant $a_K = \sqrt{3}a$. This leads to reciprocal superlattice vectors between

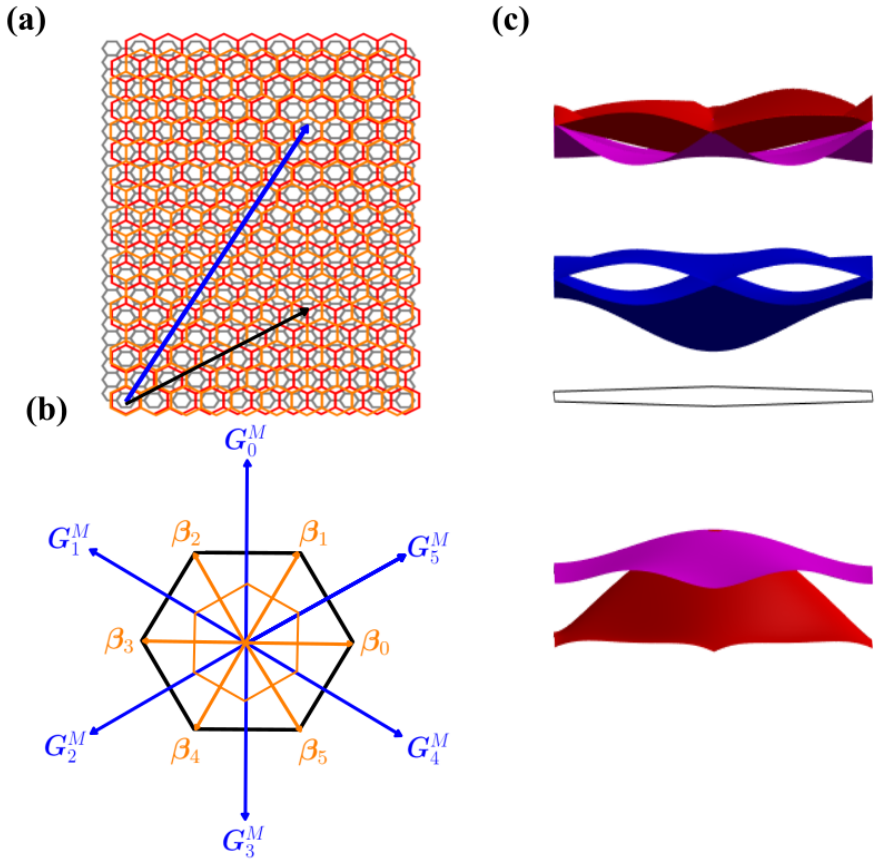


**Figure 3.4:** (a) Moiré pattern arising as a result of aligned graphene (grey) and $\alpha - In_2Te_2$ (orange) heterostructure, with moiré periodicity indicated by the black arrow. The Kekulé lattice of graphene is shown in red with the resulting longer moiré periodicity indicated by the blue arrow. (b) Superlattice Brillouin zone (black hexagon) and first star of reciprocal lattice vectors $\boldsymbol{G}_j^M$ (blue arrows) where $j = \{0, 1, ...5\}$ corresponding to the shorter periodicity (black arrow) in (a). Also shown is the superlattice Brillouin zone (orange hexagon) and first star of shorter reciprocal lattice vectors $\boldsymbol{\beta}_j$ (blue arrows) where $j = \{0, 1, ...5\}$ corresponding to the longer periodicity (blue arrow) in (a). (c) Resulting band structure of graphene on aligned ($\theta = 0$) $\alpha - In_2Te_2$. We show only the two lowest energy conduction and valence bands for clarity.

$\alpha - In_2Te_2$ and the Kekulé lattice of graphene

$$\boldsymbol{\beta_j} = \frac{1}{\sqrt{3}} \hat{\boldsymbol{R}}_{-\frac{\pi}{2}} \boldsymbol{G_j^M}, \tag{3.28}$$

as shown in Fig. 3.4 (b). Because of this shorter periodicity, the model derived in the previous section cannot accurately describe the electronic spectrum of a heterostructure composed of these two materials. Despite this, when deriving the

perturbation Hamiltonian, similar symmetry arguments can be used, albeit with certain caveats. Firstly, the reciprocal lattice vector of an almost commensurate $\sqrt{3} \times \sqrt{3}$ lattice is shorter than that of hBN such that the set $\{\boldsymbol{\beta_i}\}$ connect different valleys. Following the convention of the previous section, this results in the valley-sublattice operators which do not mix valley being neglected (those containing $\hat{\boldsymbol{\tau}}_0$ and $\hat{\boldsymbol{\tau}}_z$). Secondly, the perturbation parameters associated with the set $\{\boldsymbol{\beta_j}\}$ are likely to be different to those originating from the larger period $\{\boldsymbol{G_j^M}\}$. In fact, it has been shown [34] that the dominant effect comes from the shorter periodicity, intervalley terms. Repeating a similar procedure to that in the graphene-on-hBN case, we arrive at the result

$$\begin{aligned}
\hat{\boldsymbol{H}}(\boldsymbol{r}) =& \tilde{V}_0 \hat{\boldsymbol{F}}(\boldsymbol{r}) \otimes \hat{\boldsymbol{\sigma}}_z + \frac{1}{|\boldsymbol{\beta}|} \tilde{V}_1 \left[\boldsymbol{\sigma} \times \boldsymbol{l_z}\right] \odot \nabla \hat{\boldsymbol{F}}(\boldsymbol{r}) + \frac{1}{|\boldsymbol{\beta}|} \tilde{V}_2 \boldsymbol{\sigma} \odot \nabla \hat{\boldsymbol{F}}(\boldsymbol{r}), \\
\hat{\boldsymbol{F}}(\boldsymbol{r}) =& \hat{\boldsymbol{\tau}}_{\boldsymbol{x}} f_1(\boldsymbol{r}) + \hat{\boldsymbol{\tau}}_{\boldsymbol{y}} f_2(\boldsymbol{r}), \\
f_1(\boldsymbol{r}) =& \sum_{j=0}^{5} e^{i\boldsymbol{\beta_j} \cdot \boldsymbol{r}}, \qquad f_2(\boldsymbol{r}) = i \sum_{j=0}^{5} (-1)^j e^{i\boldsymbol{\beta_j} \cdot \boldsymbol{r}},
\end{aligned} \tag{3.29}$$

where the operator $\odot$ is the dot product where the typical multiplication of elements is replaced by the Kronecker product.

Analogous to graphene on hBN, the strength of each perturbation is defined by a constant $\{\tilde{V}_0, \tilde{V}_1, \tilde{V}_2\} = v|\boldsymbol{\beta_j}|\{U_{E'}, V_G, V_{G'}\}$ with labelling convention as used in [34, 35]. The strength of these perturbation parameters depends on the choice of substrate, and in the case of graphene on aligned $\alpha - \mathrm{In_2Te_2}$ ($\theta = 0°$) where $\delta \approx -0.7\%$, we chose $\{U_{E'}, U_G, U_{G'}\} = \{0.1, -0.2, 0\}$ such that the energy of the perturbation strength is comparable to hBN. The perturbation parameter $V_{G'}$ vanishes in the absence of misalignment angle [86, 87]. The intervalley scattering arising as a result of this perturbation leads to the modulation of Fermi velocity, leading to flatter bands as shown in Fig. 3.4 (c). Furthermore significant band gaps open in the linear spectrum leading to the formation of isolated superlattice minibands.

## 3.4 Hofstadter's butterfly in graphene/hBN heterostructures

At sufficiently large perpendicular magnetic fields, the Landau level structure of a material undergoes stark spectral modification. The competition between two characteristic length scales, the magnetic length and the lattice constant of a material, gives rise to a peculiar phenomenon known as Hofstadter's butterfly

[37, 40, 53, 89]. Fractal in nature, this butterfly pattern originates from the splitting of base Landau level energies into many minibands. However, for most materials (including graphene) the lattice constant is significantly smaller than the magnetic length resulting from any man-made magnetic field, and hence this fractal spectrum is not observed. Importantly, however, the much larger periodicities observed in the moiré superlattices discussed so far in this chapter suggest that observing Hofstadter's butterfly experimentally ought to be possible.

### 3.4.1 Moiré perturbation of Landau levels

In Chapter 2, we discussed the effect of an applied magnetic field on the tightly-bound electrons in graphene. In particular, we described how the hopping parameter between neighbouring carbon atoms becomes modified with the addition of the Peierls phase. In monolayer graphene, we therefore modify the hopping between atoms in the A and B sublattices accordingly

$$H_{AB} \to H_{AB} \exp[i\Phi] = H_{AB} \exp\left[i\frac{e}{\hbar}\int_{\boldsymbol{R}_A}^{\boldsymbol{R}_B} \boldsymbol{A}\cdot\boldsymbol{dr}\right], \tag{3.30}$$

where again we take the Landau gauge $\boldsymbol{A} = (0, Bx, 0)$ and this leads to the formation of Landau levels. Following [90], in order to simplify the calculation we introduce a new non-orthogonal hexagonal coordinate system (see Appendix 3.B) such that we rewrite the Landau gauge as

$$\boldsymbol{A} = \frac{Bx_1}{\sqrt{3}}(-\hat{\boldsymbol{x}}_{\boldsymbol{1}} + 2\hat{\boldsymbol{x}}_{\boldsymbol{2}}). \tag{3.31}$$

The resulting Landau level spectra is the same, however the associated wavefunctions become

$$\begin{aligned}
\phi_n(z) =& A_n \exp\left[-\frac{z^2}{2} - \frac{iz^2}{2\sqrt{3}}\right]\mathcal{H}_n(z),\\
z =& \frac{\sqrt{3}x_1}{2\lambda_B} - k_2\lambda_B, \quad A_n = \frac{1}{\sqrt{2^n n!\sqrt{\pi}\lambda_B L}},\\
\psi_0 =& \begin{pmatrix}\phi_0\\ 0\end{pmatrix} e^{ik_2x_2},\\
\psi_{n,s'} =& \frac{1}{\sqrt{2}}\begin{pmatrix}\phi_n\\ -e^{-2\pi i/3}si\phi_{n-1}\end{pmatrix} e^{ik_2.x_2}, \qquad n \geq 1,
\end{aligned} \tag{3.32}$$

derived in a similar manner to in Chapter 2. By placing this graphene monolayer on top of a hBN substrate the resulting superlattice and interlayer interaction

perturbs these Landau level states. Using Eq. (3.32), the matrix element between initial and final Landau levels, $n$ and $l$, under the perturbation of the hBN layer, $\hat{\boldsymbol{H}}_{\mathrm{hBN}}(\boldsymbol{r})$, can be written as

$$M_{k_2,k_2'}^{n,l,s,s'} = \int \psi_{l,s'}^{\dagger} \hat{\boldsymbol{H}}_{\mathrm{hBN}}(\boldsymbol{r}) \psi_{n,s} d^2\boldsymbol{r}. \tag{3.33}$$

### 3.4.2 Hofstadter's butterfly on a graphene/hbN superlattice

In general, the onset of the butterfly depends on the ratio between the magnetic flux in a unit cell $\phi = BA$ and the flux quantum $\phi_0 = h/e$ [53]. Therefore, taking this into account, the matrix element arising from the moiré perturbation of Landau levels depends on the phase factor[2]

$$M_{k_2,k_2'}^{n,l,s,s'} \propto e^{4i\pi \frac{k_2}{|\boldsymbol{G}^M|\sqrt{3}} \frac{q}{p}}, \tag{3.34}$$

where $\frac{p}{q} = \frac{\phi}{\phi_0}$ and $\{p, q \in \mathbb{Z} : \gcd(p,q) = 1\}$. It is clear that this phase factor remains unchanged as we make the translation

$$k_2 \to k_2 + p\frac{\sqrt{3}}{2}|\boldsymbol{G}^M|. \tag{3.35}$$

As a result of this periodicity, we can define discrete regions of $k_2$ (which we previously assumed to run through $[-\infty, \infty]$), suggesting that the theoretical properties can be described on the interval $k_2 \in [-\frac{\sqrt{3}}{4}|\boldsymbol{G}^M|p, \frac{\sqrt{3}}{4}|\boldsymbol{G}^M|p]$. Practically, this leads to a reciprocal space Bloch-like description such that the overall Hamiltonian, $\hat{\boldsymbol{H}} = \hat{\boldsymbol{\mathcal{H}}}_{\mathrm{MLG}} + \hat{\boldsymbol{H}}_{\mathrm{hBN}}$, and eigenstates, $\phi_n^r$, can be decomposed into $N$ blocks, labelled $r \in [-N/2, ..., N/2]$, where $N$ is the number of physically equivalent intervals along $k_2$. Therefore, for a given block in our Hamiltonian corresponding to the Landau level index $n$, we have

$$H_{nn}\varphi_n = \begin{pmatrix} \ddots & \vdots & \vdots & \vdots & \iddots \\ \cdots & H_{nn}^{r-1,r-1} & H_{nn}^{r-1,r} & H_{nn}^{r-1,r+1} & \cdots \\ \cdots & H_{nn}^{r,r-1} & H_{nn}^{r,r} & H_{nn}^{r,r+1} & \cdots \\ \cdots & H_{nn}^{r+1,r-1} & H_{nn}^{r+1,r} & H_{nn}^{r+1,r+1} & \cdots \\ \iddots & \vdots & \vdots & \vdots & \ddots \end{pmatrix} \begin{pmatrix} \vdots \\ \phi_n^{r-1} \\ \phi_n^{r} \\ \phi_n^{r+1} \\ \vdots \end{pmatrix}. \tag{3.36}$$

[2]In fact, this phase factor contains the only $k_2$ dependence in the matrix element.

The perturbation Hamiltonian of hBN on graphene, $\hat{\boldsymbol{H}}_{\text{hBN}}$, depends on only the simplest moiré harmonics, hence all blocks with non-adjacent $r$ can be set to zero, leaving a $3 \times 3$ Hamiltonian satisfying the equation

$$H_{nn}\varphi_n = \begin{pmatrix} H_{nn}^{r-1,r-1} & H_{nn}^{r-1,r} & 0 \\ H_{nn}^{r,r-1} & H_{nn}^{r,r} & H_{nn}^{r,r+1} \\ 0 & H_{nn}^{r+1,r} & H_{nn}^{r+1,r+1} \end{pmatrix} \begin{pmatrix} \phi_n^{r-1} \\ \phi_n^{r} \\ \phi_n^{r+1} \end{pmatrix}. \tag{3.37}$$

Therefore, for the $r$th region of reciprocal space, the Hamiltonian at the $n$th Landau level is reduced to solutions of the eigenproblem

$$H_{nn}^{r,r-1}\phi_n^{r-1} + H_{nn}^{r,r}\phi_n^{r} + H_{nn}^{r,r+1}\phi_n^{r+1} = E_n\phi_n^{r}. \tag{3.38}$$

A change in $r$ corresponds to a change in wavevector $k_2$, hence, analogous to real space tight-binding, we assume the eigenstates acquire a phase, which for the moment is unknown. However this allows the eigenproblem to be expressed as

$$\begin{aligned} H_{nn}^{r,r-1}\phi_n^{r}e^{-i\theta} + H_{nn}^{r,r}\phi_n^{r} + H_{nn}^{r,r+1}\phi_n^{r}e^{i\theta} &= E_n\phi_n^{r}, \\ \left(H_{nn}^{r,r-1}e^{-i\theta} + H_{nn}^{r,r} + H_{nn}^{r,r+1}e^{i\theta}\right)\phi_n^{r} &= E_n\phi_n^{r}, \\ H_{\text{eff}}\phi_n^{r} &= E_n\phi_n^{r}. \end{aligned} \tag{3.39}$$

It is this $H_{\text{eff}}$ that we seek to diagonalise, to obtain the energy spectrum. When translating $k_2$ by $p$ times $b\frac{\sqrt{3}}{2}$ this corresponds to the transformation

$$\psi_n(x_1, x_2, k_2) \to \psi_n(x_1, x_2, k_2 + p|\boldsymbol{G}^M|\sqrt{3}/2) = \psi_n(x_1 + p|\boldsymbol{G}^M|\lambda_B^2, x_2, k_2). \tag{3.40}$$

This suggests that, after this transformation in $k_2$, the effect is the same as a translation on $x_1$ by $p|\boldsymbol{G}^M|\lambda_B^2$. The magnetic translation operator $\Theta_{\boldsymbol{R}}$, of an eigenstate, by some vector $\boldsymbol{R} = (R_1, R_2)$, generates a phase shift [53, 90]

$$\Theta_{\boldsymbol{R}}\psi_n(x_1, x_2, k_2) = e^{ik_{\boldsymbol{R}}\cdot\boldsymbol{R}}\psi_n(x_1, x_2, k_2) = \psi_n(x_1 + R_1, x_2 + R_2, k_2). \tag{3.41}$$

Therefore, we can express the transformation of $k_2$, defined in Eq. (3.40), in terms of a magnetic translation operator by vector $(\beta pb\lambda_B^2, 0, 0)$, leading to

$$\begin{aligned} e^{ik_1 pb\lambda_B^2}\psi_n(x_1, x_2, k_2) &= \psi_n(x_1 + p|\boldsymbol{G}^M|\lambda_B^2, x_2, k_2) \\ &= \psi_n(x_1, x_2, k_2 + p|\boldsymbol{G}^M|\sqrt{3}/2), \end{aligned} \tag{3.42}$$

where the second line follows from (3.40). We note that this translation in $k_2$ is equivalent to going from $\phi_n^r$ to $\phi_n^{r+1}$ in (3.38). As a result, the corresponding phase shift, $e^{i\theta}$, is equal to the phase shift of the magnetic translation

$$\begin{aligned} e^{i\theta} &= e^{ik_1 p|\boldsymbol{G}^M|\lambda_B^2}, \\ \theta &= k_1 p|\boldsymbol{G}^M|\lambda_B^2 = 2\pi\frac{2}{|\boldsymbol{G}^M|\sqrt{3}}qk_1. \end{aligned} \tag{3.43}$$

This suggests a periodicity in $k_1$ allowing the entire line to be expressed in sections of $k_1 \in \left[-\frac{\sqrt{3}|\boldsymbol{G}^M|}{4q}, \frac{\sqrt{3}|\boldsymbol{G}^M|}{4q}\right]$. Due to the hexagonal nature of the reciprocal lattice, it is hard to quantify what the shape of this new reciprocal space region, which we call the magnetic Brillouin zone (mBZ), is, given it is restricted $q$-times in the $k_1$ direction but not in the $k_2$ direction. However, by applying the same scaling to $k_2$ simultaneously, we obtain a hexagonal magnetic Brillouin zone with area $1/q^2$ as large. This immediately adds a $q$-fold degeneracy to the system, which must be taken into account. We therefore parametrise $k_2$ using these smaller magnetic Brillouin zones

$$k_2 \to k_2 + \frac{\sqrt{3}|\boldsymbol{G}^M|}{2}\left[\frac{p}{q}t + pr\right], \tag{3.44}$$

where $t \in [0, ..., q-1]$ is a quantum number representing the $q$-fold degeneracy of the system. One immediate problem with this parametrisation is that there exist points on the entire $k_2$ line which cannot be expressed using the mBZ and integers t and s. Therefore yet another parameter, $j$, is introduced so that the entire $k_2$ axis is spanned by this parametrisation

$$k_2 \to k_2 + \frac{\sqrt{3}|\boldsymbol{G}^M|}{2}\left[\frac{p}{q}t + pr + j\right], \tag{3.45}$$

where $j \in [0, ..., p-1]$ manifests itself in a phase shift and ultimately leads to the splitting of the unperturbed Landau energy spectrum. This partitioning of the $k_2$ line is demonstrated in Fig. 3.5, where it is clear that all three indices, $r$, $t$ and $j$ are required to define the entire $k_2$ line. The different colours of these mBZs correspond to different values of $j$ and hence different values of $M_{k_2,k_2'}^{n,l,s,s'}$. The resulting Wannier function can be written as

$$|\Phi_{n,k}^{j,t}\rangle = \frac{1}{\sqrt{N}}\sum_r e^{i\theta r}\psi_n\left(x_1, x_2, k_2 + \frac{\sqrt{3}}{2}|\boldsymbol{G}^M|\left[\frac{p}{q}t + pr + j\right]\right), \tag{3.46}$$

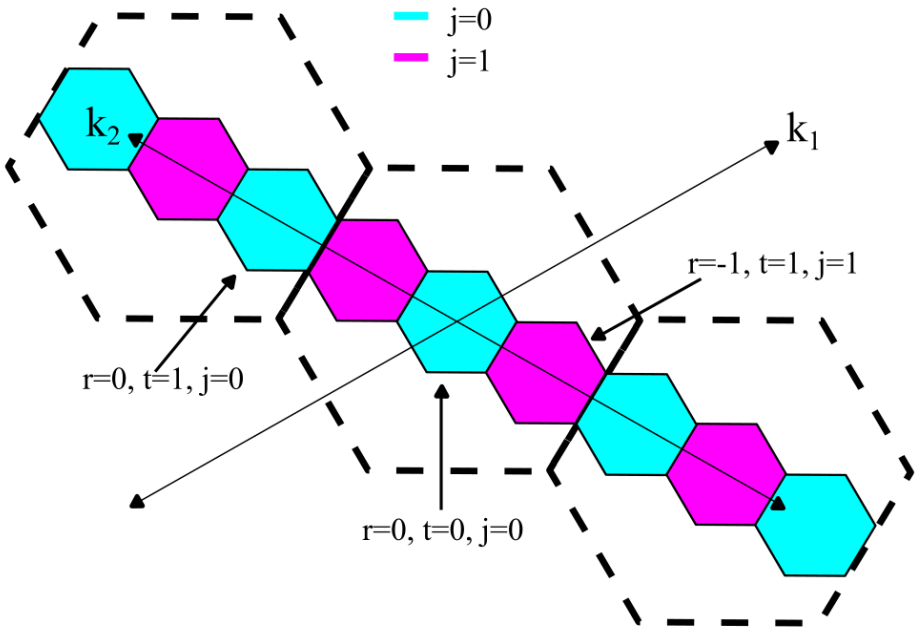


**Figure 3.5:** Parametrisation of the $k_2$ axis at magnetic field $\frac{p}{q} = \frac{2}{3}$. The original superlattice Brillouin zone is represented by the dashed hexagon, while the coloured hexagons represent the new "magnetic Brillouin zones". The blue and magenta hexagons correspond to different values of $j$. We include a few examples of how indices $r$, $t$ and $j$ parameterise these "magnetic Brillouin zones".

such that the calculation of the perturbation element becomes

$$\begin{aligned}\langle \Phi^{j,t}_{n,k} | \, \hat{\boldsymbol{H}}_{\mathrm{hBN}} \, | \Phi^{j',t'}_{n',k'} \rangle &= \sum_{r,r'} e^{-i\theta(r-r')} \\ &\times \psi^*_n \left( x_1, x_2, k_2 + \frac{\sqrt{3}}{2} |\boldsymbol{G}^M| \left[ \frac{p}{q} t + pr + j \right] \right) \\ &\times \hat{\boldsymbol{H}}_{\mathrm{hBN}} \psi_n \left( x_1, x_2, k_2 + \frac{\sqrt{3}}{2} |\boldsymbol{G}^M| \left[ \frac{p}{q} t' + pr' + j' \right] \right), \end{aligned} \tag{3.47}$$

where the sum over $r, r'$ follows from the form of Eq. (3.39). We note that varying $j$ for a given $p$ will lead to inequivalent phase factors when substituted into Eq. (3.34). As such, the value of $j$ will determine the number of levels into which an individual Landau level splits.

We plot the resulting Landau level spectrum of graphene on hBN in Fig. 3.6 (b) as a function of the magnetic field. The fine structure of the resulting fractal pattern appears as the original Landau levels (indicated by the red lines) split into multiple bands, dependent on $p$ and $q$, and as a result of the moiré perturbation.

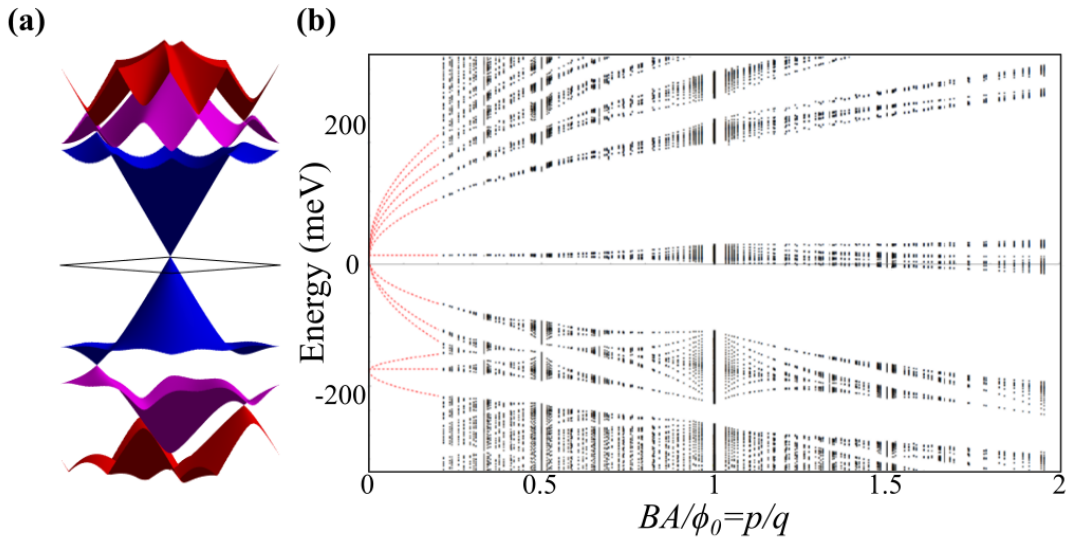


**Figure 3.6:** (a) Electronic band structure of graphene on hBN (equivalent to Fig. 3.3 (c)). (b) Fractal Hofstadter's butterfly spectrum of graphene on hBN as a function of the applied rational magnetic field, $\frac{BA}{\phi_0} = \frac{p}{q}$. The results presented here are calculated following [90]. We do not calculate the spectrum in the low flux limit and instead approximate with unperturbed Landau levels (shown in red).

The second set of Landau levels, emanating from significantly below the neutrality point, arises as a consequence of the strong spectral modification in the graphene on hBN valence bands. In particular, this new set of Landau levels emanates from the secondary Dirac point in the valence band, as shown in Fig. 3.6 (a). The fractal nature of the spectrum can be related to the self-similarity of the set of rational numbers.

## 3.A Continuum model on graphene/hBN heterostructures

In this chapter we derived an expression for the perturbation of the graphene due to a vertically stacked adjacent hBN layer using symmetry arguments. However, it is possible to extend the continuum model description of twisted bilayer graphene to model graphene on hBN [57, 91]. As a result of this, we no longer consider hBN as a perturbation and instead consider the electronic properties of the system as a whole. In a similar way to Bernal bilayer graphene and twisted bilayer graphene, the Hamiltonian can be expressed in terms of interlayer and

intralayer parts

$$\hat{\boldsymbol{H}}_{\text{Gr-hBN}}(\theta) = \begin{pmatrix} \hat{\boldsymbol{H}}_{\text{MLG}}\left(\frac{-\theta}{2}\right) & \hat{\boldsymbol{T}}_{\text{hBN-G}}(\theta) \\ \hat{\boldsymbol{T}}^{\dagger}_{\text{hBN-G}}(\theta) & \hat{\boldsymbol{H}}_{\text{hBN}}\left(\frac{\theta}{2}\right) \end{pmatrix}, \tag{3.48}$$

where $\hat{\boldsymbol{H}}_{\text{MLG}}$ describes the intralayer coupling in monolayer graphene, Eq. (2.14). The intralayer part describing hBN we express as

$$\hat{\boldsymbol{H}}_{\text{hBN}} = \begin{pmatrix} E_0^{\text{B}} & 0 \\ 0 & E_0^{\text{N}} \end{pmatrix}, \tag{3.49}$$

where $E_0^{\text{B}}$ ($E_0^{\text{N}}$) is the onsite energy of boron (nitrogen). These on-site energies are large such that the low-energy eigenstates favour the low-energy states of the graphene monolayer, hence hBN can be effectively considered an insulator. The interlayer coupling, $\hat{\boldsymbol{T}}_{\text{hBN-G}}$, where, assuming Bernal-type stacking in between the graphene and hBN and small twist angle between the graphene and hBN layer

$$\begin{aligned} \hat{\boldsymbol{T}}_{\text{hBN-G}}(\boldsymbol{k}, \overline{\boldsymbol{k}}) = &\begin{pmatrix} t_B & t_N \\ t_B & t_N \end{pmatrix} \delta_{\overline{\boldsymbol{k}},\boldsymbol{k}} + \begin{pmatrix} t_B e^{\frac{2\pi i}{3}} & t_N e^{\frac{-2\pi i}{3}} \\ t_B & t_N e^{\frac{2\pi i}{3}} \end{pmatrix} \delta_{\overline{\boldsymbol{k}}-\boldsymbol{G}_{\boldsymbol{1}}^{\boldsymbol{M}},\boldsymbol{k}} \\ &+ \begin{pmatrix} t_B e^{\frac{-2\pi i}{3}} & t_N e^{\frac{2\pi i}{3}} \\ t_B & t_N e^{\frac{-2\pi i}{3}} \end{pmatrix} \delta_{\overline{\boldsymbol{k}}+\boldsymbol{G}_{\boldsymbol{2}}^{\boldsymbol{M}},\boldsymbol{k}}. \end{aligned} \tag{3.50}$$

Here, analogous to the case of twisted bilayer, the dominant electronic properties are determined by the three shortest reciprocal lattice vectors. By comparison to more thorough numerical methods, such as DFT, this model for graphene on hBN allows the perturbation parameters $\{V_0, V_1, V_2, V_3\}$ to be estimated.

## 3.B Hexagonal coordinates: useful expressions

In this subsection, we include basic details on the hexagonal coordinate system which we utilise in our calculation of the butterfly spectra. The Cartesian and hexagonal coordinate systems are related by the following set of expressions

$$\begin{aligned} \hat{\boldsymbol{x}}_{\boldsymbol{1}} &= \frac{1}{2}\hat{\boldsymbol{x}} + \frac{\sqrt{3}}{2}\hat{\boldsymbol{y}}, \\ \hat{\boldsymbol{x}}_{\boldsymbol{2}} &= -\frac{1}{2}\hat{\boldsymbol{x}} + \frac{\sqrt{3}}{2}\hat{\boldsymbol{y}}, \end{aligned} \tag{3.51}$$

where $\hat{\boldsymbol{x}}_{\mathbf{1}}$ and $\hat{\boldsymbol{x}}_{\mathbf{2}}$ are unit vectors in the hexagonal coordinate system. Note that they are not orthogonal since

$$\hat{\boldsymbol{x}}_{\mathbf{1}} \cdot \hat{\boldsymbol{x}}_{\mathbf{2}} = \frac{1}{2}. \tag{3.52}$$

In the case when $\boldsymbol{r} = x\hat{\boldsymbol{x}} + y\hat{\boldsymbol{y}} = x_1\hat{\boldsymbol{x}}_{\mathbf{1}} + x_2\hat{\boldsymbol{x}}_{\mathbf{2}}$, we must have the following relations

$$\begin{aligned} x_1 &= x + \frac{1}{\sqrt{3}}y, \\ x_2 &= -x + \frac{1}{\sqrt{3}}y. \end{aligned} \tag{3.53}$$

# Chapter 4

# Electronic Raman scattering in twisted bilayer graphene around magic-angle twists

*The work presented in this chapter was done in collaboration with A. Garcia-Ruiz. My contribution was the formulation of the model for twisted bilayer graphene, independent calculation of the electronic Raman scattering amplitude, analysis of the results and debugging of the relevant code. The contribution of A. Garcia-Ruiz consisted of independent calculation of the Raman amplitude as well as the implementation of the twisted bilayer graphene Hamiltonian and numerical integration in to MATLAB in order to calculate the Raman intensity.*

## 4.1 Introduction

The observation of superconductivity in twisted bilayer graphene [29, 30] has revitalised theoretical and experimental interest in graphene materials. Not only is tBLG the first pure carbon superconductor, but it has a phase diagram akin to those of common non-BCS mediated high-$T_C$ superconductors. However, unlike these materials, the carrier concentration required to induce superconductivity can be achieved using gating, meaning that sweeping through voltages and temperature allows the whole phase space to be mapped (this is in contrast to high-$T_C$ superconductors where new samples have to be fabricated [92]).

One key caveat is that the misalignment angle in tBLG has to be close to a specific value. This angle, known as the magic angle (see Chapter 1) lies at approximately 1.1°. Engineering such a system poses a significant challenge, where encapsulation of the device with hBN is required to prevent the graphene layers from deforming into a structure more similar to aligned bilayer graphene.

In previous experiments [29, 30], mechanical exfoliation was used to create two flakes, which were then misaligned to the desired angle by reference to their crystallographic axis. While this technique should allow excellent control over the crystallographic alignment, strain and distortion during fabrication could effect this angle. Furthermore alternative fabrication techniques such as CVD, do not allow control over the twist angle. Therefore, there needs to be a non-invasive way to measure the twist angle in a previously fabricated sample. Around the magic angle, measuring the misalignment is particularly difficult, with ARPES unlikely to provide sufficient resolution, especially if encapsulated by hBN. Furthermore, previous Raman experiments looking at phonon modes [93, 94] attempted to establish a relationship between the twist angle and the behaviour of certain peaks, however the highly sensitive and non-monotonic behaviour suggest such methods would be inappropriate to resolve small differences in the twist angle. Instead, we propose that electronic Raman scattering, which effectively probes

the electronic density of states, can be used to determine the twist angle of the sample.

## 4.2 Theoretical description of electronic Raman scattering

Typically, Raman measurements rely on phonon modes in order to extract information about the system. Graphene, in particular, has characteristic phonon modes, the G and D-peaks [95, 96], which provide information about the quality of the graphene sheet. We focus on electronic Raman scattering, an off-resonant process which probes only the electronic band structure of the target material. An electronic Raman scattering process involves the successive absorption and emission of a photon, in either order [97, 98, 99, 100], with the frequency difference between the photons characterising the energy of the resulting electron-hole pair.

In order to describe a Raman scattering process, we must derive an expression for the interaction between an electron and a photon [97, 98, 99, 100, 101]. Such an interaction can be described by introducing the canonical momentum

$$\boldsymbol{P} = \boldsymbol{k} - \frac{e}{c}\left(\boldsymbol{A}(\boldsymbol{r},t) + \tilde{\boldsymbol{A}}(\boldsymbol{r},t)\right), \tag{4.1}$$

with the vector potentials of the incoming and outgoing photons written as $\boldsymbol{A}$ and $\tilde{\boldsymbol{A}}$ respectively. The spatial and temporal properties of these vector potentials are expressed as [98, 99]

$$\boldsymbol{A}(\boldsymbol{r},t) = \frac{\hbar c}{\sqrt{2\Omega}}\left(\boldsymbol{l}e^{i(\boldsymbol{p}\cdot\boldsymbol{r}-\Omega t)/\hbar}\hat{\boldsymbol{b}}_{\boldsymbol{p},\boldsymbol{l}}, +h.c\right), \tag{4.2}$$

$$\tilde{\boldsymbol{A}}(\boldsymbol{r},t) = \frac{\hbar c}{\sqrt{2\tilde{\Omega}}}\left(\tilde{\boldsymbol{l}}e^{i(\tilde{\boldsymbol{p}}\cdot\boldsymbol{r}-\tilde{\Omega} t)/\hbar}\hat{\boldsymbol{b}}_{\tilde{\boldsymbol{p}},\tilde{\boldsymbol{l}}} + h.c\right), \tag{4.3}$$

where $\hat{\boldsymbol{b}}_{\boldsymbol{p},\boldsymbol{l}}$ describes the annihilation of a photon with momentum $\boldsymbol{p}$ and polarisation $\boldsymbol{l}$. $\Omega$ ($\tilde{\Omega}$) represents the frequency of the interacting photon.

The interaction term between the photon and electron can be described using the current operator, $\hat{\boldsymbol{j}}$,

$$\hat{\boldsymbol{H}}_{\text{Light-Matter}}(\boldsymbol{r},t) = \hat{\boldsymbol{j}}\cdot\left(\boldsymbol{A}(\boldsymbol{r},t) + \tilde{\boldsymbol{A}}(\boldsymbol{r},t)\right) + h.o., \tag{4.4}$$

$$\hat{\boldsymbol{j}} = \left(\frac{\partial\hat{\boldsymbol{H}}}{\partial k_x}, \frac{\partial\hat{\boldsymbol{H}}}{\partial k_y}\right), \tag{4.5}$$

where $\hat{\boldsymbol{H}}$ is the electronic Hamiltonian of the target 2D material (in our case tBLG) such that the higher order terms ($h.o$) are neglected. Since all one-step processes involving both absorption and emission of a photon are higher order, the dominant contribution to Raman comes from two-step processes where an electron in an initial state $|i\rangle$, at time $t$, emits/absorbs a photon, transforming into a virtual state $|v\rangle$, before absorbing/emitting a photon at time $t'$ becoming a final state $|f\rangle$. The difference in energy between the absorbed and emitted photon $\Omega - \tilde{\Omega} = \omega$, is the Raman shift. We represent these two processes in Fig. 4.1.

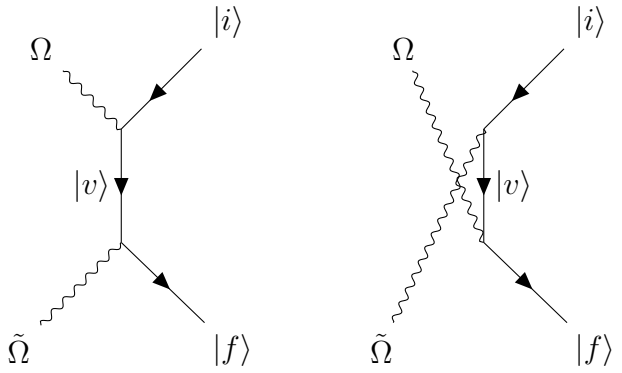


**Figure 4.1:** Feynman diagrams representing the possible two-step processes consisting of absorption of a photon of frequency $\Omega$, followed by emission of a photon, frequency $\tilde{\Omega}$ (Left) and emission followed by absorption (Right).

The light matter interaction can be written as the sum of an absorption and emission part

$$\hat{\boldsymbol{H}}_{\text{Light-Matter}}(\boldsymbol{r}, t) = \hat{\boldsymbol{H}}_{\xi}^{\text{abs}}(\boldsymbol{r}, t) + \hat{\boldsymbol{H}}_{\xi}^{\text{ems}}(\boldsymbol{r}, t), \tag{4.6}$$

where we introduce quantum numbers relevant to the electronic Hamiltonian, in this case the valley index $\xi$.

### 4.2.1 Numerical model of twisted bilayer graphene

In this section we utilise the small-twist angle Hamiltonian for tBLG. As discussed in Chapter 3, the number of Dirac cone replicas, separated by vectors $\boldsymbol{q}_{\boldsymbol{\xi}}$ (Section 3.2), required to reach convergence, depends strongly on the twist angle. Previous numerical estimates for this relationship suggest an angular dependence of $\sim 10\ \theta^{-2}$ on the size of the Hamiltonian to reach convergence [73]. Therefore, around the magic angle, we need at least 10 Dirac cone replicas. In fact, in order to preserve the symmetry of the band structure we consider 72 Dirac cone replicas

leading to a Hamiltonian of size 144.

For an individual Dirac cone replica, with momentum $\boldsymbol{k}$, layer index $\beta$ and valley $\xi$ we write the basis $\hat{\boldsymbol{c}}_{k,\xi} = (\hat{\boldsymbol{c}}^A_{k,\beta,\xi}, \hat{\boldsymbol{c}}^B_{k,\beta,\xi})^T$ such that the basis of the overall Hamiltonian can be written as $\hat{\boldsymbol{C}}_{\boldsymbol{k},\xi} = \bigoplus_{\alpha=0}^{N} \hat{\boldsymbol{c}}_{\boldsymbol{k}+\boldsymbol{q}_\alpha,\xi}$. We can relate the set of basis $\hat{\boldsymbol{C}}_{\boldsymbol{k},\xi}$ to the set of eigenvectors, $\hat{\boldsymbol{\chi}}_{n,\boldsymbol{k}}$, where $n$ labels the corresponding energy levels for a given momenta, $n \in [1, \dim(\hat{\boldsymbol{H}}^{\xi}_{\text{tBLG}})]$. In particular there exists a unitary matrix, $\hat{\boldsymbol{M}}_{\boldsymbol{k},\beta,\xi}$, which relates the eigenvectors and basis

$$\hat{\boldsymbol{C}}_{\boldsymbol{k},\xi} = \hat{\boldsymbol{M}}_{\boldsymbol{k},\beta,\xi}\hat{\boldsymbol{\chi}}_{n,\boldsymbol{k}}. \tag{4.7}$$

### 4.2.2 Current vertex calculation

The vertices of the Feynman diagrams presented in Fig. 4.1, correspond to an interaction between an electron and a photon. Quantitatively we express these vertices as a probability amplitude

$$\hat{\boldsymbol{V}}_{\text{abs}}(t) = \sum_{\alpha} \hat{\boldsymbol{C}}^{\dagger}_{\boldsymbol{k}+\boldsymbol{q}_\alpha,\xi}\hat{\boldsymbol{H}}^{\text{abs}}_{\xi}(\boldsymbol{r},t)\hat{\boldsymbol{C}}_{\boldsymbol{k}+\boldsymbol{q}_\alpha,\xi}, \tag{4.8}$$

where we drop the layer index as it is redundant. In order to discuss the formation of an electron-hole pair, it is necessary to frame the discussion in terms of transitions between energy bands. Using the relationship between basis states and the eigenstates, Eq. (4.7) we can express this in terms of the energy bands

$$\hat{\boldsymbol{V}}^{i\to\nu}_{\text{abs}}(t) = \sum_{\xi,\sigma}\sum_{\alpha,i,v}\sum_{j,j'}[\hat{\boldsymbol{M}}^{j'v}_{\boldsymbol{k}+\boldsymbol{q}_\alpha,\xi}\hat{\boldsymbol{\chi}}_{v,\boldsymbol{k}+\boldsymbol{q}_\alpha}]^{\dagger}\hat{\boldsymbol{H}}^{\text{abs}}_{\xi}(\boldsymbol{r},t)\hat{\boldsymbol{M}}^{j,i}_{\boldsymbol{k}+\boldsymbol{q}_\alpha,\xi}\hat{\boldsymbol{\chi}}_{i,\boldsymbol{k}+\boldsymbol{q}_\alpha}, \tag{4.9}$$

$$\hat{\boldsymbol{V}}^{i\to\nu}_{\text{ems}}(t) = \sum_{\xi,\sigma}\sum_{\alpha,i,v}\sum_{j,j'}[\hat{\boldsymbol{M}}^{j'v}_{\boldsymbol{k}+\boldsymbol{q}_\alpha,\xi}\hat{\boldsymbol{\chi}}_{v,\boldsymbol{k}+\boldsymbol{q}_\alpha}]^{\dagger}\big(\hat{\boldsymbol{H}}^{\text{ems}}_{\xi}(\boldsymbol{r},t)\big)^{*}\hat{\boldsymbol{M}}^{j,i}_{\boldsymbol{k}+\boldsymbol{q}_\alpha,\xi}\hat{\boldsymbol{\chi}}_{i,\boldsymbol{k}+\boldsymbol{q}_\alpha}, \tag{4.10}$$

where superscripts in $\hat{\boldsymbol{M}}^{a,b}_{\boldsymbol{k},\xi}$ are the row and column index.

### 4.2.3 The two-step process

We now wish to calculate the Raman amplitude and probability of two-step processes where, for a resulting electron-hole pair, we consider all intermediate states. For fermionic creation (annihilation) operators in energy band $n$ and momentum $\boldsymbol{k}$, previously defined as $\hat{\boldsymbol{\chi}}^{\dagger}_{n,\boldsymbol{k}}(\hat{\boldsymbol{\chi}}_{n,\boldsymbol{k}})$, we define an excited final state

as

$$|\text{Exc}\rangle = \hat{\boldsymbol{\chi}}^{\dagger}_{n',\boldsymbol{k}}\hat{\boldsymbol{\chi}}_{n,\boldsymbol{k}}\,|\text{GS}\rangle\,. \tag{4.11}$$

Therefore the Raman amplitude between an initial, $i$, and final, $f$, state is

$$\begin{aligned} R_{f\leftarrow i} &= \frac{-1}{\hbar^2}\int_{-\infty}^{\infty} dt' \int_{-\infty}^{t'} dt \left[\hat{\boldsymbol{V}}_{\text{abs}}(t')\hat{\boldsymbol{V}}_{\text{ems}}(t) + \hat{\boldsymbol{V}}_{\text{ems}}(t')\hat{\boldsymbol{V}}_{\text{abs}}(t)\right] \\ &= \sum_v \mathcal{P}_v^{\text{abs-ems}}\mathcal{I}_v^{\text{abs-ems}} + \sum_v \mathcal{P}_v^{\text{ems-abs}}\mathcal{I}_v^{\text{ems-abs}}, \end{aligned} \tag{4.12}$$

where we have performed time ordering and then separated the contributions into those of the time-resolved integral $\mathcal{I}_v$ and polarisation $\mathcal{P}_v$ over all virtual states $v$. We first calculate the time integral

$$\begin{aligned} \mathcal{I}_v^{\text{abs-ems}} &= \frac{-1}{\hbar^2}\int_{-\infty}^{\infty} dt' \int_{-\infty}^{t'} dt e^{i(E_f - E_v + \tilde{\Omega})t} e^{i(E_v - E_i - \Omega - i\delta_+)t'} \\ &= 2\pi i \frac{\delta(E_i - E_f + \Omega - \tilde{\Omega})}{E_i - E_v - \Omega - i\delta_+}, \end{aligned} \tag{4.13}$$

$$\begin{aligned} \mathcal{I}_v^{\text{ems-abs}} &= \frac{-1}{\hbar^2}\int_{-\infty}^{\infty} dt' \int_{-\infty}^{t'} dt f e^{i(E_f - E_v + \Omega)t} e^{i(E_v - E_i - \tilde{\Omega} - i\delta_+)t'} \\ &= 2\pi i \frac{\delta(E_i - E_f + \Omega - \tilde{\Omega})}{E_i - E_v + \tilde{\Omega} - i\delta_+}, \end{aligned} \tag{4.14}$$

where we introduce the small quantity $\delta^+$ to ensure that the integral is well-defined. Noting that $\Omega - \tilde{\Omega} = \omega$ allows us to write

$$\mathcal{I}_v^{\text{abs-ems}} = 2\pi i \frac{1}{E_i - E_v - \Omega}, \tag{4.15}$$

$$\mathcal{I}_v^{\text{ems-abs}} = 2\pi i \frac{1}{E_i - E_v + \Omega - \omega}. \tag{4.16}$$

The polarisation factor $\mathcal{P}_v$ is just the remaining terms following the calculation of the time resolved part and concerns the light polarisation and momentum of

the participating electronic states

$$\begin{aligned}\mathcal{P}_v^{\text{abs-em}} =& \sum_{\xi',\sigma'}\sum_{\alpha',v,f}\sum_{\tilde{j},\tilde{j}'}[\hat{\boldsymbol{M}}^{\tilde{j}'f}_{\boldsymbol{k}+\boldsymbol{q}_{\alpha'},\xi'}\hat{\boldsymbol{\chi}}_{f,\boldsymbol{k}+\boldsymbol{q}_{\alpha'}}]^\dagger\big(\hat{\boldsymbol{H}}^{\text{ems}}_\xi(\boldsymbol{r},0)\big)^*\hat{\boldsymbol{M}}^{\tilde{j},v}_{\boldsymbol{k}+\boldsymbol{q}_{\alpha'},\xi'}\hat{\boldsymbol{\chi}}_{v,\boldsymbol{k}+\boldsymbol{q}_{\alpha'}}\\ &\times\sum_{\xi,\sigma}\sum_{\alpha,i,v}\sum_{j,j'}[\hat{\boldsymbol{M}}^{j'v}_{\boldsymbol{k}+\boldsymbol{q}_\alpha,\xi}\hat{\boldsymbol{\chi}}_{n,\boldsymbol{k}+\boldsymbol{q}_\alpha}]^\dagger\hat{\boldsymbol{H}}^{\text{abs}}_\xi(\boldsymbol{r},0)\hat{\boldsymbol{M}}^{j,i}_{\boldsymbol{k}+\boldsymbol{q}_\alpha,\xi}\hat{\boldsymbol{\chi}}_{i,\boldsymbol{k}+\boldsymbol{q}_\alpha},\\ \mathcal{P}_v^{\text{em-abs}} =& \sum_{\xi',\sigma'}\sum_{\alpha',v,f}\sum_{\tilde{j},\tilde{j}'}[\hat{\boldsymbol{M}}^{\tilde{j}'f}_{\boldsymbol{k}+\boldsymbol{q}_{\alpha'},\xi'}\hat{\boldsymbol{\chi}}_{f,\boldsymbol{k}+\boldsymbol{q}_{\alpha'}}]^\dagger\hat{\boldsymbol{H}}^{\text{abs}}_\xi(\boldsymbol{r},0)\hat{\boldsymbol{M}}^{\tilde{j},v}_{\boldsymbol{k}+\boldsymbol{q}_{\alpha'},\xi'}\hat{\boldsymbol{\chi}}_{v,\boldsymbol{k}+\boldsymbol{q}_{\alpha'}}\\ &\times\sum_{\xi,\sigma}\sum_{\alpha,i,v}\sum_{j,j'}[\hat{\boldsymbol{M}}^{j'v}_{\boldsymbol{k}+\boldsymbol{q}_\alpha,\xi}\hat{\boldsymbol{\chi}}_{n,\boldsymbol{k}+\boldsymbol{q}_\alpha}]^\dagger\big(\hat{\boldsymbol{H}}^{\text{ems}}_\xi(\boldsymbol{r},0)\big)^*\hat{\boldsymbol{M}}^{j,i}_{\boldsymbol{k}+\boldsymbol{q}_\alpha,\xi}\hat{\boldsymbol{\chi}}_{i,\boldsymbol{k}+\boldsymbol{q}_\alpha}.\end{aligned}$$

Although this suggests contributions for all combinations of $i, f$ and $v$ we note that depending on the position of the chemical potential, certain transitions are forbidden where, as fermions, the creation of identical electrons and holes is prohibited by Pauli exclusion. In order to calculate the Raman probability, we integrate over all momenta and act on the Fermi sea, $|\text{GS}\rangle$ (assuming the chemical potential sits at the neutrality point). We thus obtain an expression for the intensity at Raman shift $\omega$

$$W(\omega) = \sum_{\xi,\sigma}\int\frac{\boldsymbol{dk}}{(2\pi\hbar)^3}|\,\langle\text{Exc}|\,R_{f\leftarrow i}\,|\text{GS}\rangle\,|^2. \tag{4.17}$$

## 4.3 Results

We now present the Raman intensity as a function of Raman shift for a range of twist angles close to the magic angle. In Fig. 4.2, we show the Raman intensity at a range of angles around the magic angle. Similar to the case of monolayer [98, 102] and superconducting monolayer graphene [100], the Raman amplitude depends predominantly on the electronic band structure, such that the final electron-hole pairs roughly correspond to the density of states of the conduction (CB) and valence bands (VB). In (a) we show the electronic Raman spectrum (ERS) for twisted bilayer with 2° misalignment angle. The peak seen in the electronic Raman spectrum at about 100 meV originates from final electron-hole states between the first valence and first conduction band, as indicated by the blue peak in the central column of Fig. 4.2 (a). One might assume, therefore, that the peak in the Raman intensity corresponds to electron-hole states between the two Van Hove singularities in the 1$^{\text{st}}$ conduction and valence bands. However, due to the electron-hole asymmetry in the tBLG band structure and

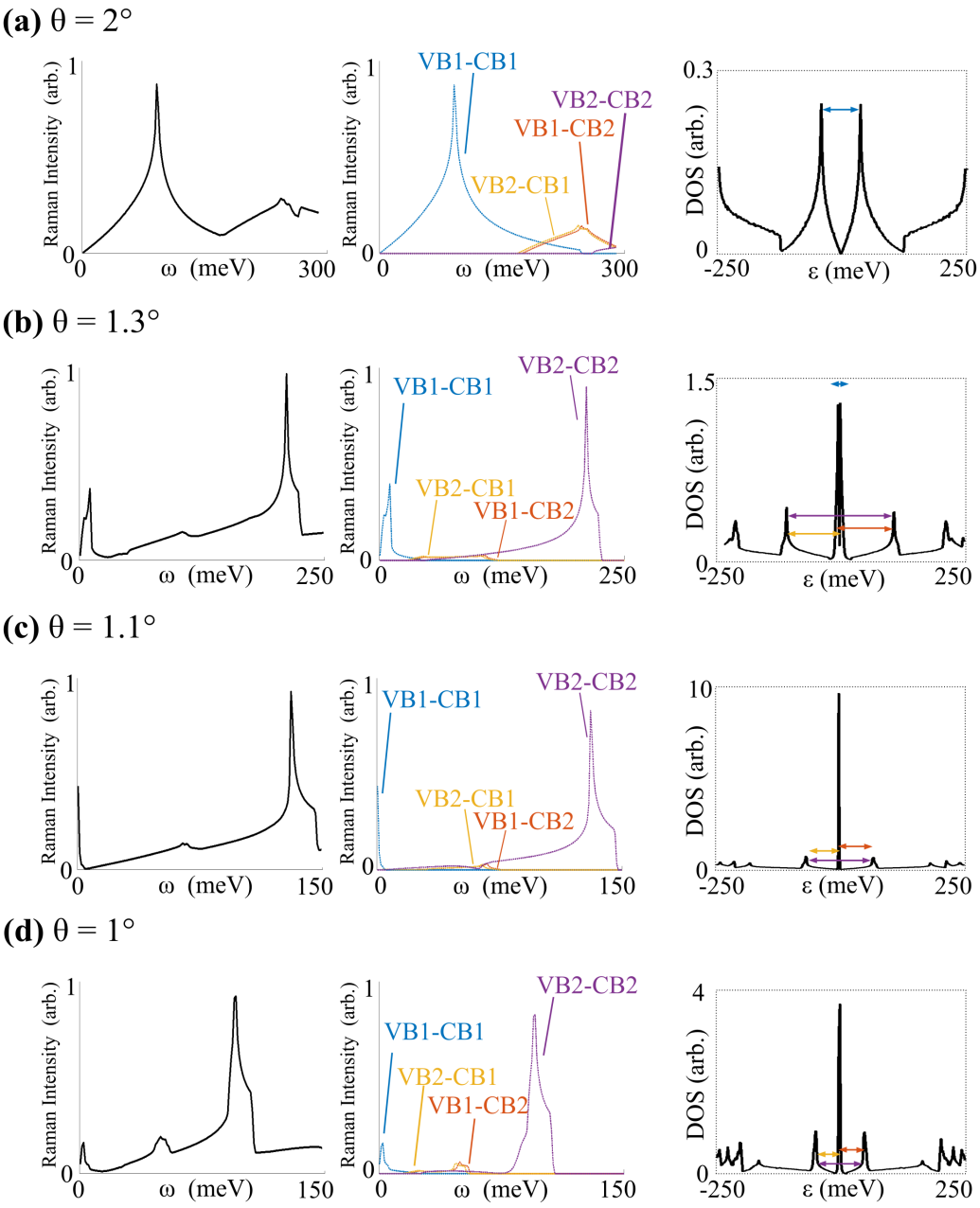


**Figure 4.2:** Left column shows the total calculated electronic Raman spectra of twisted bilayer graphene at misalignment angle (a) 2° (b) 1.3° (c) 1.1° (the magic angle in our model) and (d) 1°. The middle column shows the individual contributions to the total spectra in the left column for each pair of conduction (CB) and valence bands (VB): VB1-CB1 (blue), VB1-CB2 (red), VB2-CB1 (yellow) and VB2-CB2 (purple). In the right column we show the density of states of twisted bilayer graphene at the given angle and indicate the energy separation between Van Hove singularities corresponding to the same peaks in the middle column.

because the incident and outgoing photons impart no lateral momentum on the electron-hole pair, no such states exist. Instead, the peak in intensity corresponds to the regions of almost parallel conduction and valence bands between the Van Hove singularities[1]. This can also be seen from the right column of Fig. 4.2 (a) where the separation between VHS is smaller than energy of the Raman peak in the left and middle columns. In Fig. 4.2 (b) we present the same results for a smaller twist angle, 1.3° (just above the magic angle). Note that as the twist angle is lowered, the Van Hove singularities move closer together as observed in Fig. 4.2 (b). Furthermore, higher energy conduction and valence bands start to move closer together. As a result, the electronic Raman spectrum at 1.3° presented in the left column of Fig. 4.2 (b) has two clear peaks corresponding to different electron-hole excitations, as indicated in the middle column.

At the magic angle, the $1^{st}$ conduction and valence bands are flat, with a minimum in the Fermi velocity and sharp peak in the density of states. In Fig. 4.2 (c) we plot the Raman intensity at the magic angle, with the first peak lying at Raman shift $\omega = 0$ [2].

Furthermore, we observe the onset of two small second peaks corresponding to the transitions between the first valence and second conduction band, and due to symmetry, the second valence and first conduction band. In addition to this, a larger peak is seen at a slightly larger Raman shift, corresponding to a second conduction to second valence band transition. In this case the peak corresponds precisely to excited states between the Van Hove singularities, as, the flattest region of both bands lie at the same momentum. The profile of these peaks gives insight into their origin and when combined with the Raman shift at which these peaks are observed, gives a robust way to determine the twist angle of the twisted bilayer sample.

As the twist angle is lowered below the magic angle, the flat bands observed at the magic angle partially "unflatten", as seen in the density of states plot in the right column of Fig. 4.2 (d). As a result, the corresponding Raman peak shifts away from the origin as seen in the left and central columns of Fig. 4.2 (d), however the Raman peaks corresponding to higher transitions continue to shift towards the origin.

In Fig. 4.3, we show more clearly the variation in position of the $1^{st}$-$1^{st}$

[1]This however still acts a good probe of the twist angle as the peak shifts towards the frequency origin as the twist angle is reduced towards the magic angle.

[2]As the first conduction and valence bands are not completely flat, the Raman peak is slightly above the $\omega = 0$ point, however this wouldn't be resolved. Around $\omega = 0$, the frequency of the incident and outgoing photons are almost the same suggesting the energy separation between the two bands is close to zero.

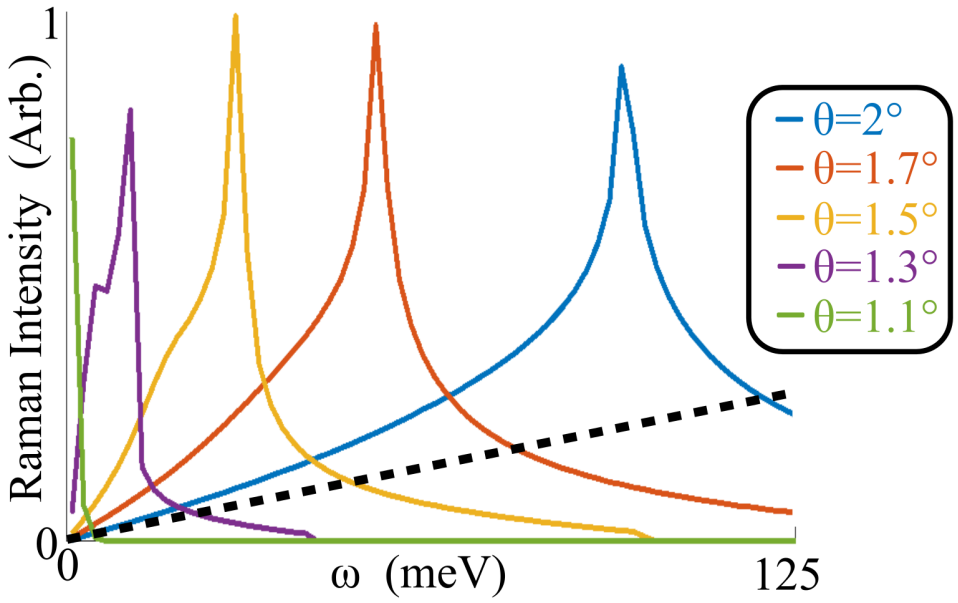


**Figure 4.3:** Electronic Raman intensity corresponding to the 1st valence to 1st conduction excited state plotted for a range of angles from 2° to the magic angle, 1.1°. The dashed black line shows the Raman intensity corresponding to monolayer graphene.

valence-conduction electronic Raman peak as a function of angle. As a comparison we also indicated the ERS for monolayer graphene in Fig. 4.3. The peaks observed in tBLG are significantly larger than in MLG. This suggests that, based on previous experiments [101, 102], the electronic Raman spectrum we obtain should be observable experimentally.

In Fig. 4.4, we present the evolution of the electronic Raman spectrum for decreasing angle below the magic angle. Below the magic angle, although the signal from the 1st-1st valence-conduction transition begins to fade (as seen in the inset in Fig. 4.4), the peak corresponding to the 2nd-2nd valence-conduction transition remains prominent. Similarly to Fig. 4.3, as the angle is decreased, this peak shifts towards the origin suggesting that it could also be used as a probe. Furthermore, the spectral profile of this peak remains relatively constant for changing angle allowing for easier identification.

In practice, the electronic Raman spectra will have to compete with the much larger peaks in the Raman measurement corresponding to phonon modes. However, in general, these occur at much higher frequencies than discussed here [93, 94, 95, 96, 101, 103], suggesting that electronic Raman features should only compete with experimental noise, as observed in monolayer graphene [102]. In

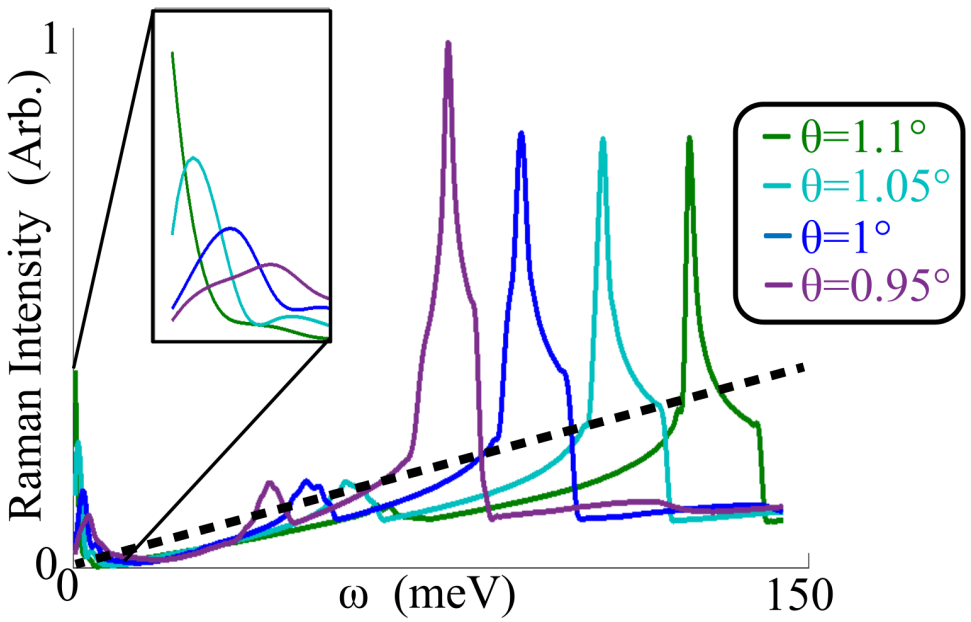


**Figure 4.4:** Total electronic Raman intensity plotted for a range of angles from 1.1°, the magic angle to 0.95°. The inset shows the magnification of the Raman spectra at low energies. The dashed black line shows the Raman intensity corresponding to monolayer graphene.

Fig. 4.5 we plot the position of the two strongest peaks corresponding to the 1$^{st}$ conduction to 1$^{st}$ valence and 2$^{nd}$ conduction to 2$^{nd}$ valence, as a function of twist angle, with solid lines. We compare this peak position to the separation between the VHS of the these bands, shown with dashed lines in Fig. 4.5. The separation between the solid and dashed lines for the1$^{st}$ conduction and valence bands (blue and cyan in Fig. 4.5) highlights the fact that electron-hole pairs between the Van Hove singularities are not responisble for the associated Raman peak. By cross-referencing the positions of the experimentally observed ERS peaks with Fig. 4.5, the twist angle can be read off immediately. Unfortunately, we believe that this technique is inappropriate for large twist angle twisted bilayer as the observed peaks occur at Raman shifts comparable to the much larger phonon modes.

## 4.4 Summary

We have modelled the electronic Raman spectrum of low-angle twisted bilayer. We have demonstrated that as the twist angle is reduced towards the magic angle, the peak in the Raman spectrum corresponding to electron-hole pairs in the first

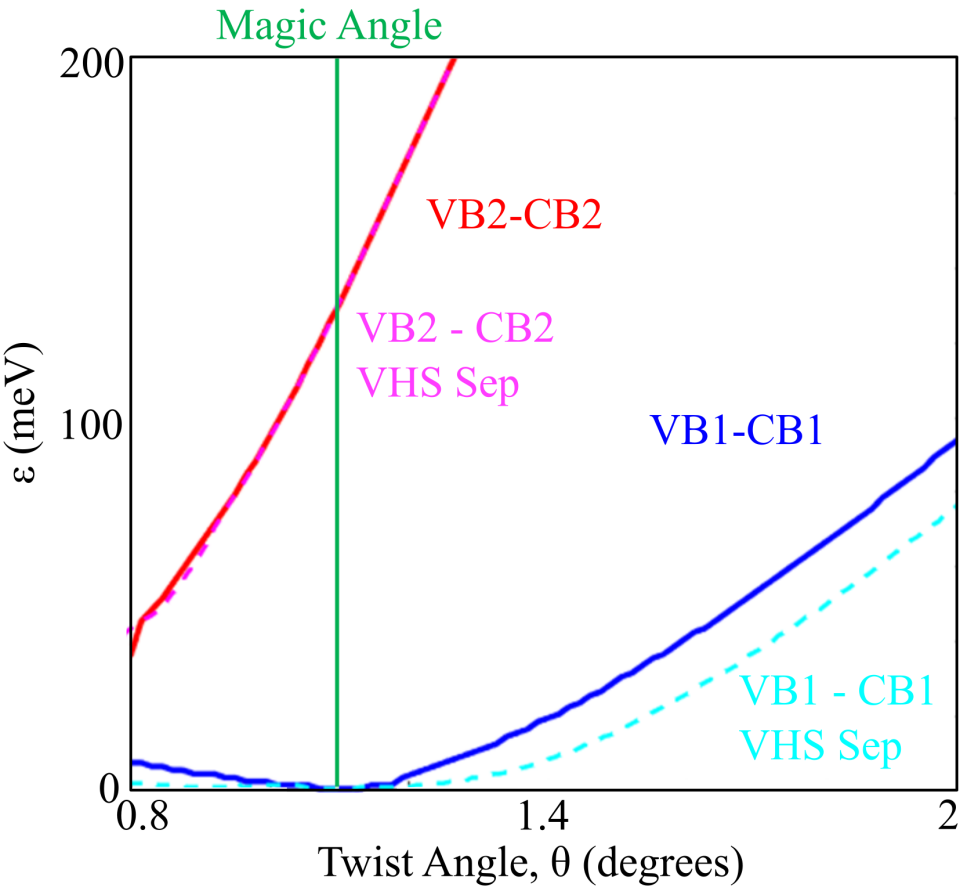


**Figure 4.5:** Position of the 1st Valence to 1st conduction band (blue) and 2nd valence to 2nd conduction band (red) Raman peaks as a function of twist angle. The green vertical line indicates the position of the magic angle. The dashed lines correspond to the separation between the Van Hove singularities of the 1st valence to 1st conduction bands (cyan) and 2nd valence to 2nd conduction bands (magenta).

conduction and valence band moves towards the origin as the bands begin to flatten. Below the magic angle, this peak begins to fade and move away from the origin however peaks corresponding to excited states involving other pairs of bands begin to appear in the low energy Raman shift region. We demonstrate that by examining the spectral profile it is possible to infer the origin of the Raman peaks, which, when compared with the angle-dependence of the peak position allows accurate estimation of the twist angle in bilayer graphene. The observed Raman peaks are more pronounced than in monolayer graphene, which has been observed experimentally, and occur at Raman frequencies away from those of prominent Raman modes in twisted bilayer graphene.

# Chapter 5

# Determination of interatomic coupling in twisted graphene using angle-resolved photoemission

*The work presented in this chapter was done in collaboration with experimental physicists at the Chen group in Oxford, who provided all experimental data. My contribution was all the theoretical modelling and experimental fits.*

## 5.1 Introduction

In order to properly understand the electronic properties of stacks of twisted two-dimensional materials, it is crucial to accurately model the interlayer coupling. The interlayer coupling between two-dimensional materials dictates the value of the magic-angle, at which, twisted graphene demonstrates superconductivity and strongly correlated behaviour [29, 30]. However, current models for the interlayer coupling in twisted graphene layers fail to accurately describe bilayer graphene in the limit of zero misalignment angle. In this chapter, we propose that twisted trilayer graphene (tTLG) is the simplest material within which to compare the interlayer coupling between aligned and misaligned graphene layers. As such, we propose a self-consistent parameter set which describes both these couplings in the context of the continuum model, which we verify by comparison to angle-resolved photoemission spectroscopy measurements.

Experimentally, angle resolved photoemission spectroscopy (ARPES) is a powerful tool used to determine the electronic structure of a material [104, 105, 106]. Based on the photoelectric effect [107], photons incident on the surface of a material excite electrons causing them to be ejected. By measuring the characteristics of the ejected electrons, in particular the electronic momenta perpendicular to the surface, the energy and wave vector of the electron can be used to construct the electronic band structure of the target material.

ARPES has been extensively used to characterise graphene-based materials. This includes simple graphene monolayers and bilayers [108, 109, 110], to graphene on almost commensurate substrates [111] and twisted graphene layers [112, 113]. We demonstrate excellent agreement between experimental ARPES spectra and the theoretical band structure calculated using our proposed self-consistent parameter set. We also discuss the effect of substrate doping on the experimental ARPES spectra, which we take into account in our model.

## 5.2 Theoretical model of ARPES

The term "angle-resolved" originates from the method by which the lateral electronic momenta is probed. The ejected electrons are captured by a hemi-

spherical detector, such that the polar and azimuthal angles of detection, $\phi$ and $\vartheta$, respectively, can be used to determine the momenta [114]

$$\begin{aligned} p_x &= \sqrt{2m_e\varepsilon}\sin\phi\cos\vartheta, \\ p_y &= \sqrt{2m_e\varepsilon}\sin\phi\sin\vartheta, \\ p_\perp &= \sqrt{2m_e\varepsilon}\cos\phi, \end{aligned} \tag{5.1}$$

where $m_e$ is the mass of the emitted electron and $\varepsilon$ is the energy. In Fig. 5.1

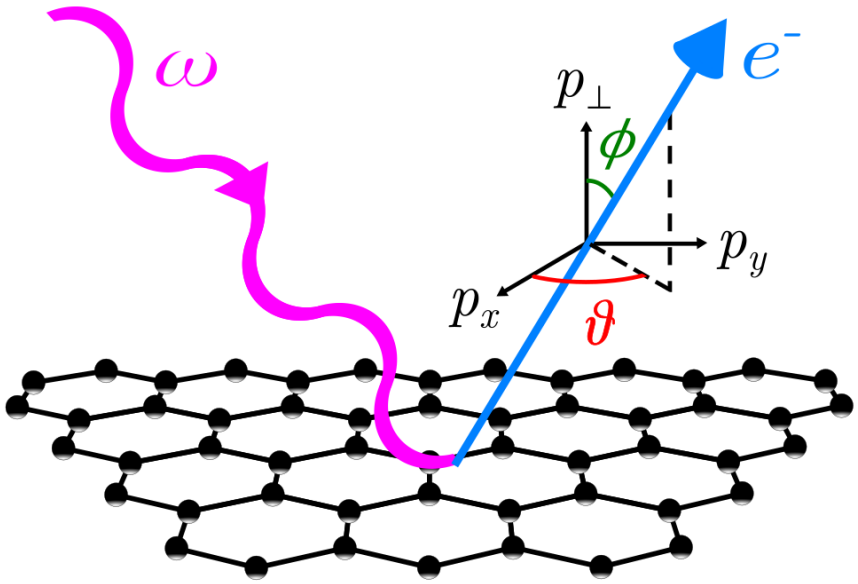


**Figure 5.1:** Diagram of a typical ARPES scattering process, where a photon of frequency $\omega$ (magneta), incident on a graphene surface (black hexagons), leads to the emission of an electron (blue). The electronic momenta (black axes) and the scattering angles, $\phi$ (green) and $\vartheta$ (red) are also included for clarity.

we present a diagram of a typical ARPES process with the electronic momenta and the scattering angles labelled. In bulk materials, extracting the relationship between the momenta and electron energy is difficult due to non-zero out-of-plane momentum [115], however in few-layer materials such as simple van der Waals heterostructures, this is relatively easy as the measured ARPES spectra directly probes a single constant-energy contour. Therefore, a single photon frequency probes the band structure at one energy, meaning that, energy slice by energy slice, the entire electronic dispersion can be constructed. In particular, by utilising the conservation of energy and by assuming that the incident photon does not impart lateral momentum on the electron, Eq. (5.1) can be used to extract information about the band structure. In bulk materials, additional constraints

need to be considered due to photons of a certain energy exciting electrons at a range of perpendicular momenta, $p_\perp$, [115]. The conservation of energy can be described in the following way: for a photon with energy $\omega$ greater than the work function of the material, $W$, the detected energy, $\varepsilon$, and initial energy, $\varepsilon_{\boldsymbol{p}}$, can be related as

$$W + \varepsilon = \omega + \varepsilon_{\boldsymbol{p}}. \tag{5.2}$$

The momentum constraint arises as a result of the Bloch states of the layered material, as demonstrated for graphene in Chapter 2. For a measured momentum, $\boldsymbol{p}_D = (p_x, p_y, p_\perp)$ (see Eq. (5.1)), the lateral component, $\boldsymbol{p}$, is simply

$$|\boldsymbol{p}| = \sqrt{|\boldsymbol{p}_D|^2 - p_\perp^2}. \tag{5.3}$$

For a given energy, the ejected electron, can either have momentum $\hbar\boldsymbol{k}$, where $\boldsymbol{k}$ is the initial momentum state of the electron, or momentum $\hbar(\boldsymbol{k} + \boldsymbol{G})$, where

$$\boldsymbol{G} = c_1\boldsymbol{G}_1 + c_2\boldsymbol{G}_2, \qquad c_1, c_2 \in \mathbb{Z}, \tag{5.4}$$

and we define $\boldsymbol{G}_1, \boldsymbol{G}_2$ as the reciprocal lattice vectors of the target material. In the case of graphene these reciprocal lattice vectors are defined in Eq. (2.4).

The interaction between the incident photon and ejected electron can be described perturbatively using the light-matter interaction [116, 117]

$$\hat{\boldsymbol{\mathcal{H}}}_{\mathrm{LM}} = -\frac{e}{m_e}\hat{\boldsymbol{A}} \cdot \hat{\boldsymbol{p}}, \tag{5.5}$$

where $\hat{\boldsymbol{A}}$ is the vector potential of the incident photon and $\hat{\boldsymbol{p}}$ is the momentum operator. The ejected electron is considered a free particle and can therefore be modelled using a plane wave

$$|\varphi(\boldsymbol{r}, \boldsymbol{k'})\rangle \propto e^{i\boldsymbol{k'}\cdot\boldsymbol{r}}. \tag{5.6}$$

The initial state, an electron in band $j$, is described using a Bloch function of $p_z$ orbitals, $|\Psi_j(\boldsymbol{r}, \boldsymbol{k})\rangle$, as defined in Eq. (2.5). Therefore the matrix element associated with the ejection of an electron in the $j$-th band in the crystal into the vacuum by a photon is

$$M_j \propto -\frac{e}{m_e}\left\langle\varphi(\boldsymbol{r}, \boldsymbol{k'})\right| \hat{\boldsymbol{A}} \cdot \hat{\boldsymbol{p}} \left|\Psi_j(\boldsymbol{r}, \boldsymbol{k})\right\rangle. \tag{5.7}$$

The treatment of the light-matter interaction will vary depending on the required accuracy [116, 117, 118]. We note initially that all information encoding the band structure of the target structure (monolayer, twisted bilayer, etc) originates from the constants $c_{m,j}$, derived from band structure calculations, and that the remainder is likely to encode relative intensities. In this thesis, we focus predominantly on the shape (rather than intensities) of the ARPES spectra. Therefore, setting $\hat{\boldsymbol{A}} \cdot \hat{\boldsymbol{p}}$ as an arbitrary constant and continuing from Eq. (5.7), we can write the matrix element as

$$M_j \propto -\frac{e}{m_e}\frac{1}{\sqrt{N}}\sum_{m}^{n}\sum_{l}^{N} c_{m,j} e^{i(\boldsymbol{k}-\boldsymbol{k'})\cdot\boldsymbol{R}_{l,m}} \left\langle e^{i\boldsymbol{k'}\cdot(\boldsymbol{r}-\boldsymbol{R}_{l,m})} | \psi_m(\boldsymbol{r}-\boldsymbol{R}_{l,m}) \right\rangle . \tag{5.8}$$

The sum over $l$ is reduced trivially to a delta function prescribing in-plane momentum conservation, $\boldsymbol{k}-\boldsymbol{k'} = \boldsymbol{G}$. Furthermore, the inner product can be written as

$$\langle e^{i\boldsymbol{k'}\cdot(\boldsymbol{r}-\boldsymbol{R}_{l,m})} | \psi_m(\boldsymbol{r}-\boldsymbol{R}_{l,m}) \rangle = \int e^{-i\boldsymbol{k'}\cdot(\boldsymbol{r}-\boldsymbol{R}_{l,m})} \psi_m(\boldsymbol{r}-\boldsymbol{R}_{l,m}) dV = \tilde{\psi}_m(\boldsymbol{k'}), \tag{5.9}$$

where $\tilde{\psi}_m(\boldsymbol{k'})$ is the Fourier transform of the $p_z$-orbital, which we approximate as a constant. Again, we note that proper treatment of this Fourier transform is likely to only affect intensities rather than change the shape of measured ARPES spectra [1]. Previous attempts to treat these prefactors more thoroughly have had mixed success [116, 117, 118, 119] offering marginal gains in accuracy when compared to measured intensities. The matrix element associated with the photoemission of an electron is

$$M_j \propto \sum_{m}^{n} c_{m,j} e^{i\boldsymbol{G}\cdot\overline{\boldsymbol{R}}_m}. \tag{5.10}$$

Using Fermi's golden rule [120], the ARPES intensity of the $j$-th band can therefore be expressed as

$$I_j \sim \left| \sum_{m}^{n} c_{m,j} e^{i\boldsymbol{G}\cdot\overline{\boldsymbol{R}}_m} \right|^2 \delta(W + \varepsilon - \omega - \varepsilon_{j,\boldsymbol{p}}), \tag{5.11}$$

where the Dirac delta function is introduced to take into account the energy conservation. In theory, experimental ARPES spectra are broadened [104], dif-

[1] It is also worth pointing out that, in graphene, close to the Brillouin zone corner it can be argued that $\hat{\boldsymbol{A}} \cdot \hat{\boldsymbol{p}}$ and $\tilde{\psi}_m(\boldsymbol{k'})$ are roughly constant [52], which should hold for small twist angles in twisted bilayer graphene.

ferently in energy and momentum. This is dependent on the resolutions of the particular setup, however, for simplicity we model the energy broadening as a Lorentzian

$$\delta(W+\varepsilon-\omega-\varepsilon_{j,\boldsymbol{p}}) \to \frac{1}{\pi}\frac{\gamma}{(W+\varepsilon-\omega-\varepsilon_{j,\boldsymbol{p}})^2-\gamma^2}. \tag{5.12}$$

We extract the half-width-half-maximum, $\gamma$, by comparing to experimental data. The expressions above were derived while neglecting most of the complexities of an APRES process. These include dynamical effects [121, 122], interactions between graphene and the substrate [108] and polarisation of the incident light [119], to name just a few. However, as previously discussed, these should either only alter intensities, or lead to minor deviations in the ARPES spectra, some of which are resolvable in the experiment described here. Moreover, we use an exponential decay, $e^{-\alpha n}$, where $\alpha$ is the decay constant and $n$ is the layer number, in order to roughly estimate the intensity difference between electrons originating from different layers. Electrons on the layer furthest from the detector travel further and risk being scattered by closer layers while the total number of photons incident on the layer further away is also smaller.

## 5.3 Twisted trilayer graphene

In this section we derive a theoretical model for twisted trilayer graphene. We focus on $(\theta-0-0)$ trilayers where the top layer is misaligned compared to the other two layers, which are arranged in the typical Bernal stacking. In a similar way to twisted bilayer, we can define the intralayer and interlayer coupling separately. We treat the intralayer part using the typical monolayer graphene Hamiltonian, Eq. (2.14), modified for the relative twist-angle. We model the interlayer interaction with relative rotation $\theta$ using $\hat{\boldsymbol{T}}(\theta)$ as defined in Eq. (3.5). On the basis $(A1, B1, A2, B2, A3, B3)$, we express the Hamiltonian for $(\theta_1-\theta_2-\theta_3)$ twisted trilayer with arbitrary twist angles as

$$\hat{\boldsymbol{H}}_{\mathrm{tTLG}}(\theta_1,\theta_2,\theta_3) = \begin{pmatrix} \hat{\boldsymbol{H}}_{\mathrm{MLG}}(\theta_1,u_1) & \hat{\boldsymbol{T}}(\theta_1-\theta_2) & \hat{\boldsymbol{V}}(\theta_1-\theta_3) \\ \hat{\boldsymbol{T}}^\dagger(\theta_1-\theta_2) & \hat{\boldsymbol{H}}_{\mathrm{MLG}}(\theta_2,u_2) & \hat{\boldsymbol{T}}(\theta_2-\theta_3) \\ \hat{\boldsymbol{V}}^\dagger(\theta_1-\theta_3) & \hat{\boldsymbol{T}}^\dagger(\theta_2-\theta_3) & \hat{\boldsymbol{H}}_{\mathrm{MLG}}(\theta_3,u_3) \end{pmatrix}, \tag{5.13}$$

where $\hat{\boldsymbol{V}}(\theta)$ describes the interlayer coupling between layer 1 and layer 3 of the trilayer while $\{u_1, u_2, u_3\}$ are the on-site energies of the three layers. As in ABA/ABC trilayer graphene [123, 124], the coupling between the outer layers

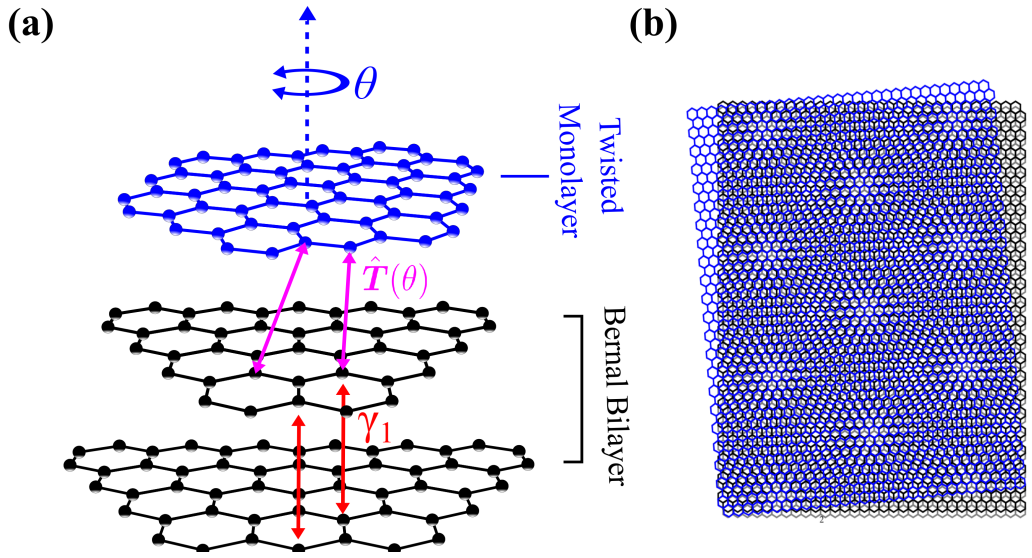


**Figure 5.2:** (a) Twisted trilayer graphene, $(\theta - 0 - 0)$, with the aligned Bernal bilayer shown in black and twisted monolayer in blue with twist angle, $\theta$. Also indicated is the dominant coupling between Bernal bilayers, $\gamma_1$, shown in red, and the coupling between twisted bilayers $\hat{\boldsymbol{T}}(\theta)$, shown in pink. (b) Top-down, long-range crystallographic structure of $(\theta - 0 - 0)$ twisted trilayer graphene. The Bernal-stacked layers, shown in black and grey, lie beneath the rotated blue monolayer.

is much weaker than between adjacent layers. Hence, we neglect $\hat{\boldsymbol{V}}(\theta)$ as it will only induce minor changes in the ARPES spectra, which are most likely undetectable at the resolutions seen in experiment. As we are focusing on twisted $(\theta - 0 - 0)$ trilayers, we set the twist angle between layer 2 and layer 3 as zero. Hence, as $\theta_2, \theta_3 \to 0$, we should obtain the coupling in Bernal bilayer

$$\hat{\boldsymbol{T}}(0) = \begin{pmatrix} 0 & 0 \\ \gamma_1 & 0 \end{pmatrix}, \tag{5.14}$$

such that Eq. (5.13) becomes

$$\hat{\boldsymbol{H}}_{\mathrm{tTLG}}(\theta_1, 0, 0) = \begin{pmatrix} \hat{\boldsymbol{H}}_{\mathrm{MLG}}(\theta_1, u_1) & \hat{\boldsymbol{T}}(\theta_1) & 0 \\ \hat{\boldsymbol{T}}^{\dagger}(\theta_1) & \hat{\boldsymbol{H}}_{\mathrm{MLG}}(0, u_2) & \hat{\boldsymbol{T}}(0) \\ 0 & \hat{\boldsymbol{T}}^{\dagger}(0) & \hat{\boldsymbol{H}}_{\mathrm{MLG}}(0, u_3) \end{pmatrix}. \tag{5.15}$$

The interlayer coupling between the twisted layers in tTLG is described using the continuum model as outlined in Eq. (3.14). The resulting band structure consists of two neutrality points: one Dirac cone from the monolayer part, and one Bernal bilayer dispersion offest from the monolayer cone in reciprocal space

by the vector $\boldsymbol{q}_{\boldsymbol{\xi}} = (\hat{\mathbf{1}} - \hat{\boldsymbol{R}}_{\theta_1})\boldsymbol{K}_{\boldsymbol{\xi}}$ (as defined in Section 3.2). In a similar way to twisted bilayer, where these bands cross, hybridisation occurs resulting in the formation of Van Hove singularities. The additional bands present as a result of the high-energy bands in the Bernal bilayer part mean that there are a total of four band crossings in the simplest electronic dispersion. The application of an on-site energy difference between the Bernal bilayer and misaligned monolayer parts acts in a similar way to that of twisted bilayer moving the neutrality points up and down in energy. In contrast, non-zero $u$ between the two layers of the Bernal bilayer opens a gap in the quadratic dispersion at the neutrality point.

Similarly to twisted bilayer, reducing the twist angle causes the separation between neutrality points $\boldsymbol{q}_{\xi}$ to shrink. As a result, the energy at which band hybridisation is observed is lowered until at about 1.1° where the dispersion becomes completely flat, suggesting that a magic angle exists for twisted trilayer. It is still unclear whether any of the recently discovered many-body phenomenon in tBLG [29, 30] are observable in trilayer samples.

Twisted trilayer graphene is the thinnest single sample which allows the direct comparison of the interlayer coupling between graphene layers at zero and non-zero misalignment. When comparing separate bilayers, one twisted and one Bernal stacked for example, variations in synthesis, quality and detection methods could affect the observed ARPES spectra, changing the parametrisation between samples. This makes twisted trilayer graphene a far more convenient sample to use (in the case of separate bilayer layers, more care needs to be taken). Furthermore the additional band crossing in twisted trilayer provides another reference point which can be used to extra information about the interlayer coupling between twisted layers.

In order to describe the real-space coupling between twisted graphene layers, multiple proposals have been put forward to model the coupling strength between carbon $p_z$ orbitals [71, 74, 75, 76]. Although more complex techniques which take into account all orbitals and the local environment, such as DFT, should theoretically give more accurate results, this is computationally expensive and often does not match experimental observations quantitatively. The simplest description is to take a two-centre approximation [71, 76], where two $p_z$-orbitals, separated by a vector $\boldsymbol{r} = (\boldsymbol{r}_{||}, d_0)$ , interact only with each other, such that $\boldsymbol{r}_{||}$ is the in-plane component

$$t(\boldsymbol{r}) = V_{pp\pi}(\boldsymbol{r})\left(1 - \frac{(\boldsymbol{r}\cdot\boldsymbol{e}_z)^2}{|\boldsymbol{r}|^2}\right) + V_{pp\sigma}(\boldsymbol{r})\left(\frac{\boldsymbol{r}\cdot\boldsymbol{e}_z}{|\boldsymbol{r}|}\right)^2, \tag{5.16}$$

where $V_{pp\sigma}$ and $V_{pp\pi}$ represent $\sigma$ and $\pi$ bonding respectively, with prefactors

taking into account the relative orientation of these orbitals [71, 125]. The ideal functional form of $V_{pp\sigma}(\boldsymbol{r})$ and $V_{pp\pi}(\boldsymbol{r})$ should reproduce $\gamma_0$ and $\gamma_1$ when $\boldsymbol{r} = \delta$ and $\boldsymbol{r} = d_0\boldsymbol{e}_z$ respectively, hence

$$\begin{aligned} V_{pp\sigma}(\boldsymbol{r}) &= \gamma_1 e^{-\dfrac{|\boldsymbol{r}| - d_0}{r_\sigma a}}, \\ V_{pp\pi}(\boldsymbol{r}) &= \gamma_0 e^{-\dfrac{|\boldsymbol{r}| - |\boldsymbol{\delta}|}{r_\pi a}}, \end{aligned} \tag{5.17}$$

where $r_\sigma$ and $r_\pi$ are constants corresponding to the decay of $\sigma$ and $\pi$ bonding respectively. Crucially, taking this functional form reproduces the nearest interlayer coupling in aligned bilayer, $\gamma_1$.

In the continuum model, the interlayer coupling is expressed as the sum of an infinite number of terms, which can be truncated to the three dominant terms. However, we should include all terms in order to be precise, such that, the coupling between each pair of sublattices becomes a convergent sum. Furthermore, following our discussion in Section 3.2, in the limit of zero angle, this sum produces a non-zero term only in the position $\{B, \overline{A}\}$ (equivalent to (A2,B1) in Bernal bilayer) such that expansion of Eq. (3.14) over all $\boldsymbol{G}, \overline{\boldsymbol{G}}$, for zero angle, produces

$$\hat{\boldsymbol{T}}(0) = 3\left[\tilde{t}(\boldsymbol{K_\xi}, d_0) + \tilde{t}(2\boldsymbol{K_\xi}, d_0) + 2\tilde{t}(\sqrt{7}\boldsymbol{K_\xi}, d_0) + ...\right]\begin{pmatrix} 0 & 0 \\ 1 & 0 \end{pmatrix} \approx \begin{pmatrix} 0 & 0 \\ \gamma_1 & 0 \end{pmatrix}. \tag{5.18}$$

This relationship adds another restriction on the model for $t(\boldsymbol{r})$ as $\tilde{t}(\boldsymbol{q}, d_0)$ should decay such that the sum converges to $\gamma_1$. Therefore, ideal parameters for the decay constants are $r_\sigma = 0.06$ and $r_\pi = 0.12$ such that $\tilde{t}(\boldsymbol{K_\xi}, d_0) = 110$ meV, $\tilde{t}(2\boldsymbol{K_\xi}, d_0) = 14$ meV and $\tilde{t}(\sqrt{7}\boldsymbol{K_\xi}, d_0) = 2.5$ meV.

In Fig. 5.3 (a), we plot the interlayer coupling set in real space as a function of interatomic distance, $\boldsymbol{R}$, for the above parameter set which, as expected, decays exponentially. The value of this curve at $\boldsymbol{R} = 0$ indicates the value of $\gamma_1$. The Fourier transform, $\tilde{t}(\boldsymbol{q}, d_0)$, utilised in the continuum model, which represents the interlayer coupling in reciprocal space, is presented Fig. 5.3 (b). We indicate important values such as $\tilde{t}(\boldsymbol{K_\xi}, d_0)$ and $\tilde{t}(2\boldsymbol{K_\xi}, d_0)$ with dashed lines. We note that the exponential decay of this parameter set suggests that, in the infinite expansion appearing in the interlayer coupling, the sum reaches convergence, as shown in Eq. (5.18). Importantly, this parameter set does not depend on the misalignment angle and as such should describe the interlayer coupling between

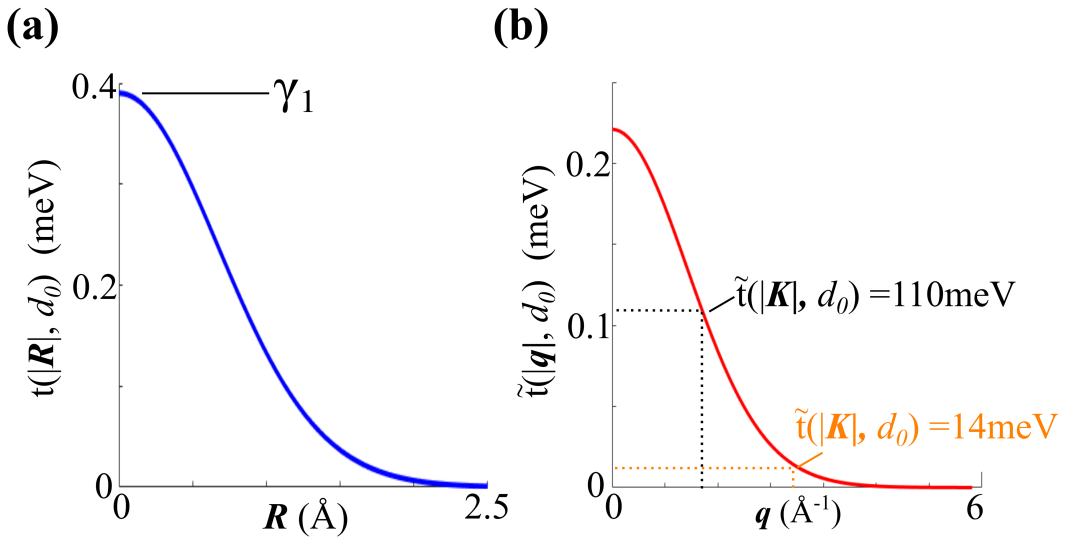


**Figure 5.3:** (a) The real-space interlayer interatomic coupling as a function of the in-plane interatomic distance, $\boldsymbol{R}$ for the parameter set: $\gamma_0 = -2.95$ eV, $\gamma_1 = 0.39$ eV, $d_0 = 3.3$ Å, $r_\sigma = 0.06$ and $r_\pi = 0.12$. (b) The Fourier transform of (a) into reciprocal space. We indicate two important values of $\tilde{t}(\boldsymbol{q}, d_0)$ with dashed lines.

twisted graphene layers with any orientation.

By parametrising the interatomic coupling between twisted graphene layers in this way we have produced a self-consistency loop between the real space coupling and continuum model regimes. First, the interlayer coupling between twisted layers depends on the Fourier transform of the real space coupling, and second, the continuum model describing the interlayer coupling between twisted layers reproduces the real space coupling in the limit of zero-angle. This self-consistency demonstrates the strength of our model and in particular our parametrisation of the interatomic coupling, and we compare to experimental ARPES data in the next section.

## 5.4 Comparison to experiment

In this section, we compare our calculated ARPES spectra for twisted trilayer graphene, with experimental data obtained by collaborators. The samples were grown on copper foil via chemical vapour deposition. Chemical vapour deposition (CVD) is a fabrication technique used to create crystalline samples and previous ARPES measurements on CVD grown graphene crystals have shown good agreement with the theorized electronic band structure [14, 112, 113]. CVD is also preferred over exfoliated graphene as it allows the synthesis of large area

sheets of graphene, necessary to get high reciprocal space resolution in ARPES measurements.

The APRES measurements (microARPES) presented in this chapter were performed at the spectromicroscopy beamline at the Elletra synchrotron in Trieste. Since the samples were grown using chemical vapour deposition they form trilayer graphene with arbitrary twist angles[2]. Despite the range in rotation angles, a few trilayer samples with the required $(\theta - 0 - 0)$ stacking were observed (as seen from ARPES), their formation helped by the fact that Bernal bilayer is an energetically favourable configuration.

In order to perform fits we need to first ascertain the on-site potential difference and misalignment angle from the experimental ARPES spectra. Due to differences in the work functions between graphene and copper substrates, as well as chemical bonds forming between the graphene and copper surface [126], the graphene becomes doped. This can be modelled as follows: let us assume that the work functions of graphene and the copper substrate differ, such that the difference between their neutrality points can be written as $\Delta\rho$, therefore for chemical potentials of $\mu_{\mathrm{Cu}}$ and $\mu_{\mathrm{Gr}}$ we can use Gauss's law to construct the following electrostatic equation.

$$\mu_{\mathrm{Gr}} - \mu_{\mathrm{Cu}} + \Delta\rho = ed|\boldsymbol{E}| \tag{5.19}$$

where $\boldsymbol{E}$ is the perpendicular electric field between the graphene and copper, and $d$ is the spatial separation between them. We note that $\Delta\rho$ is dependent on the initial work functions but also on the interaction between copper and graphene. Furthermore, due to the size and thus electron density of the copper substrate, as compared to graphene, it is unlikely that the chemical potential will vary much away from the neutrality point. The electric field between the graphene and copper layers is proportional to the charge density difference between them, $\Delta n$

$$|\boldsymbol{E}| = \frac{ed}{\epsilon_0}|\Delta n| = \frac{ed}{\epsilon_0}\int_0^{|\mu_{\mathrm{Gr}}-\mu_{\mathrm{Cu}}|} D_{\mathrm{Gr}}(\varepsilon)d\varepsilon, \tag{5.20}$$

where $\epsilon_0$ is the permittivity of free space, and $D_{\mathrm{Gr}}(\varepsilon)$ is the density of states of graphene at energy $\varepsilon$. At low energies, $D_{\mathrm{Gr}}(\varepsilon)$ is approximately linear in $\varepsilon$ such that Eq. (5.19) becomes a quadratic equation that can be solved exactly with fits obtained from experiment. This method can be extended to any number of layers

[2]Both misalignment angles presented in this chapter are around 9 degrees while previous twisted bilayer samples performed by the same group have shown samples ranging from 5° to 23° [113]

by reformulating Eq. (5.19) at each interface. The twist angle can be obtained from the ARPES data by measuring the distance in reciprocal space between the neutrality points and extracting the angle from the expression for $\boldsymbol{q}_\xi$. We compare two samples with relevant data shown in Table (5.1).

**Table 5.1:** Measured twist angle and on-site energies $u_1$, $u_2$ and $u_3$ for samples 1 and 2

| Trilayer Samples | | | | |
|---|---|---|---|---|
| Sample | Twist Angle, $\theta_1$ (°) | $u_1$ (meV) | $u_2$(meV) | $u_3$ (meV) |
| 1 | 9.6 | 0 | -90 | -310 |
| 2 | 9.06 | 0 | 40 | $\approx 40$ |

In Fig. 5.4, we show experimental ARPES maps for sample 1 at a range of energy values in the left column and these are compared with theoretical ARPES maps in the middle column, calculated using the parameters in Table (5.1). Contours of the theoretical band structure are shown in the right hand column. The small differences in theoretical and experimental plots are likely due to dynamical effects not incorporated into our model and give rise to variations in intensity. Part (i) in Fig 5.4 shows the ARPES map and energy contour at photon energy corresponding to the Dirac point originating from the twisted monolayer. At this energy, the contour corresponding to the monolayer part of the spectrum vanishes leaving only a bilayer part, visible due to the non-zero energy offset between the top and middle layers. The ARPES spectra becomes point-like however does not vanish at the Dirac point due to broadening. We note that, although Dirac-cone replicas are observed in the contour plots, these are strongly suppressed in ARPES experiments, hence the additional circles at the top and bottom right of the contour plot in part (ii) are not observed. The next energy slice, displayed in part (ii), occurs at $\varepsilon - \varepsilon_0 = -0.4$ eV. The ARPES maps and contours at this energy expand displaying the expected dispersion in both the monolayer and bilayer parts. Notably, both components display a degree of trigonal warping. At the third energy slice, part (iii), we observe the appearance of the bilayer higher energy band in the experimental ARPES spectrum. This is presented by the blue circle in the contour plot. The energy at which this peak appears is determined by the value of $\gamma_1$ hence this allows direct comparison to our theoretical model. In part (iv), at energy just below the first Van Hove singularity, $\varepsilon - \varepsilon_0 = -0.7$ eV, we observe that the contours corresponding to the monolayer and bilayer parts become connected. This can be seen in the ARPES spectra where the two curved intensity regions cross. Furthermore, at this energy, the higher energy

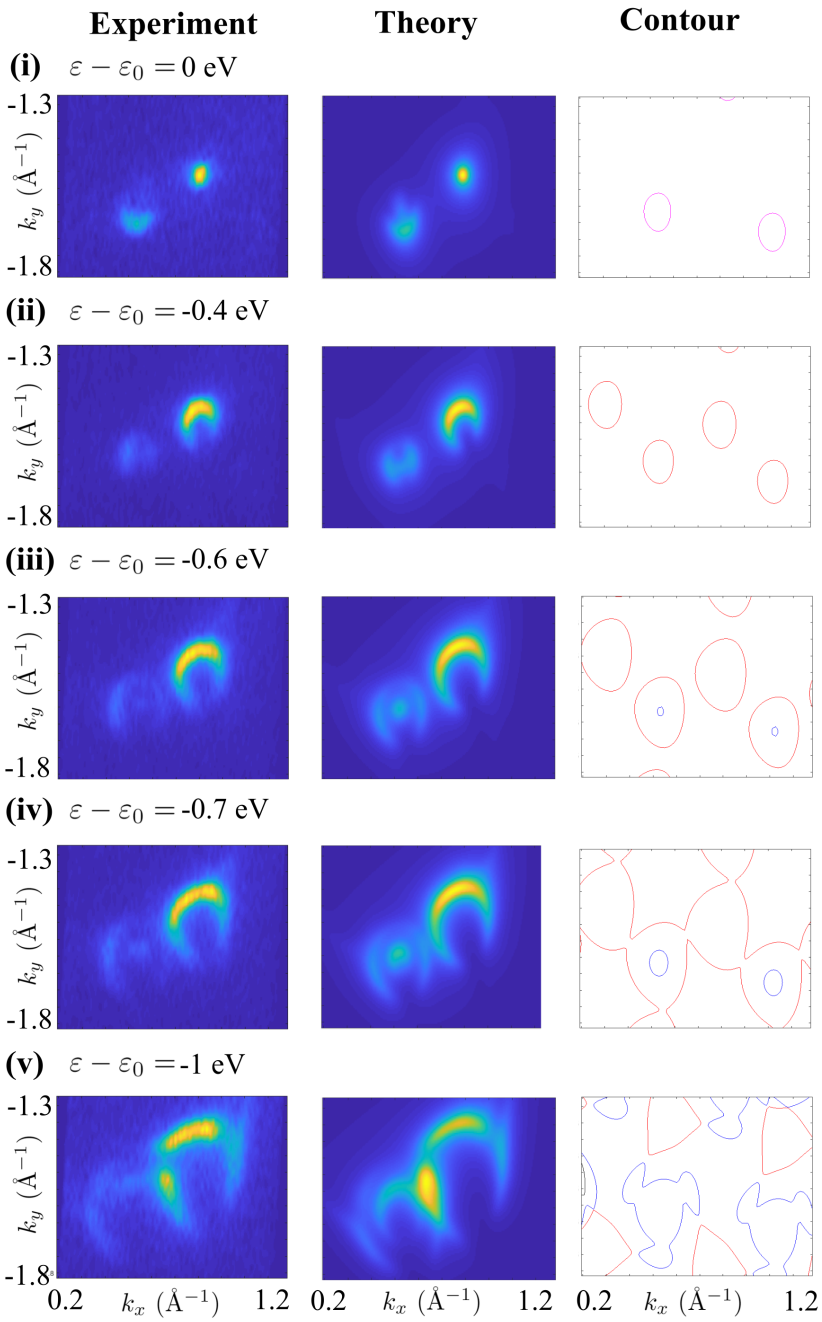


**Figure 5.4:** (Colour Online) The left column shows the experimental ARPES spectra at constant energies for sample 1: (i) $\varepsilon - \varepsilon_0 = 0$ eV, (ii) $\varepsilon - \varepsilon_0 = -0.4$ eV, (iii) $\varepsilon - \varepsilon_0 = -0.6$ eV, (iv) $\varepsilon - \varepsilon_0 = -0.7$ eV and (v) $\varepsilon - \varepsilon_0 = -1$ eV. The intensities are normalised in each row. The middle column shows the corresponding normalised theoretical ARPES spectrum calculated using parameters discussed in Table (5.1), broadening of $\gamma = 0.17$ eV and decay of $\alpha = 0.17$. The right column displays the corresponding constant energy contours obtained from the band structure using the same parameters. Counting downwards, the first, second and third valence bands are shown in red, blue and black respectively.

band originating from the Bernal bilayer part has expanded, as seen in both the ARPES measurements and calculated band structure. Finally, part (v) shows the ARPES spectra for an energy of $\varepsilon - \varepsilon_0 = -1$ eV, positioned just below the third Van Hove singularity, which arises as a result of hybridisation between the higher energy bilayer band and monolayer band.

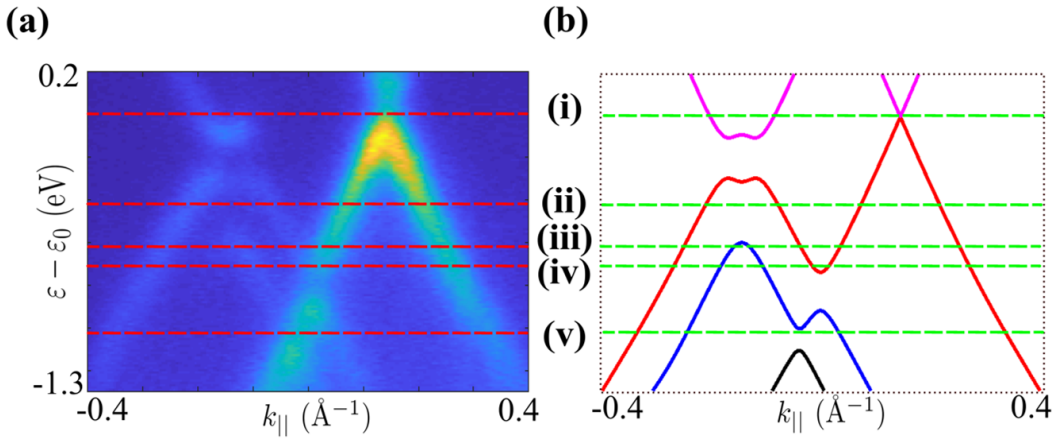


**Figure 5.5:** (Colour Online) (a) Normalised ARPES spectra for sample 1, measured along the vector connecting Dirac points. The red dashed lines, labelled (i) - (v), correspond to the constant energy cuts shown in Fig. (5.4). (b) Calculated band structure along the same vector, using fitting parameters shown in Table (5.1). The dashed lines (shown in green for clarity) correspond to those in (a).

For added clarity we plot ARPES spectra for a range of energies along the vector connecting the two Dirac points, in Fig. 5.5 (a) and compare to the calculated band structure between the same points in (b). In general, excellent agreement is shown between the ARPES spectra and calculated band structure suggesting that firstly, our estimation of the experimental twist angle and on-site energy differences $u_1$ and $u_2$ is sound and secondly, our model of the interlayer coupling element discussed in Section 5.3 reproduces both $\gamma_1$ and $\tilde{t}(\boldsymbol{q}, d_0)$.

Shifting attention now to sample 2, we compare experimental and theoretical ARPES spectra in Fig. 5.6. One notable difference between sample 1 and 2 is that the on-site energy difference is of the opposite sign. This suggests that the copper substrate now acts as a hole-donor [113] which is predicted to arise if the interlayer separation between the graphene and copper substrate is increased [126]. This effect could be due to defects in the growth process of the graphene or alternatively, surface roughness of the copper substrate. This arrangement of bands makes it more difficult to determine the size of the gap as the Dirac point corresponding to the bilayer graphene lies above the chemical potential prohibiting it being probed via ARPES. Despite this we are able to estimate the

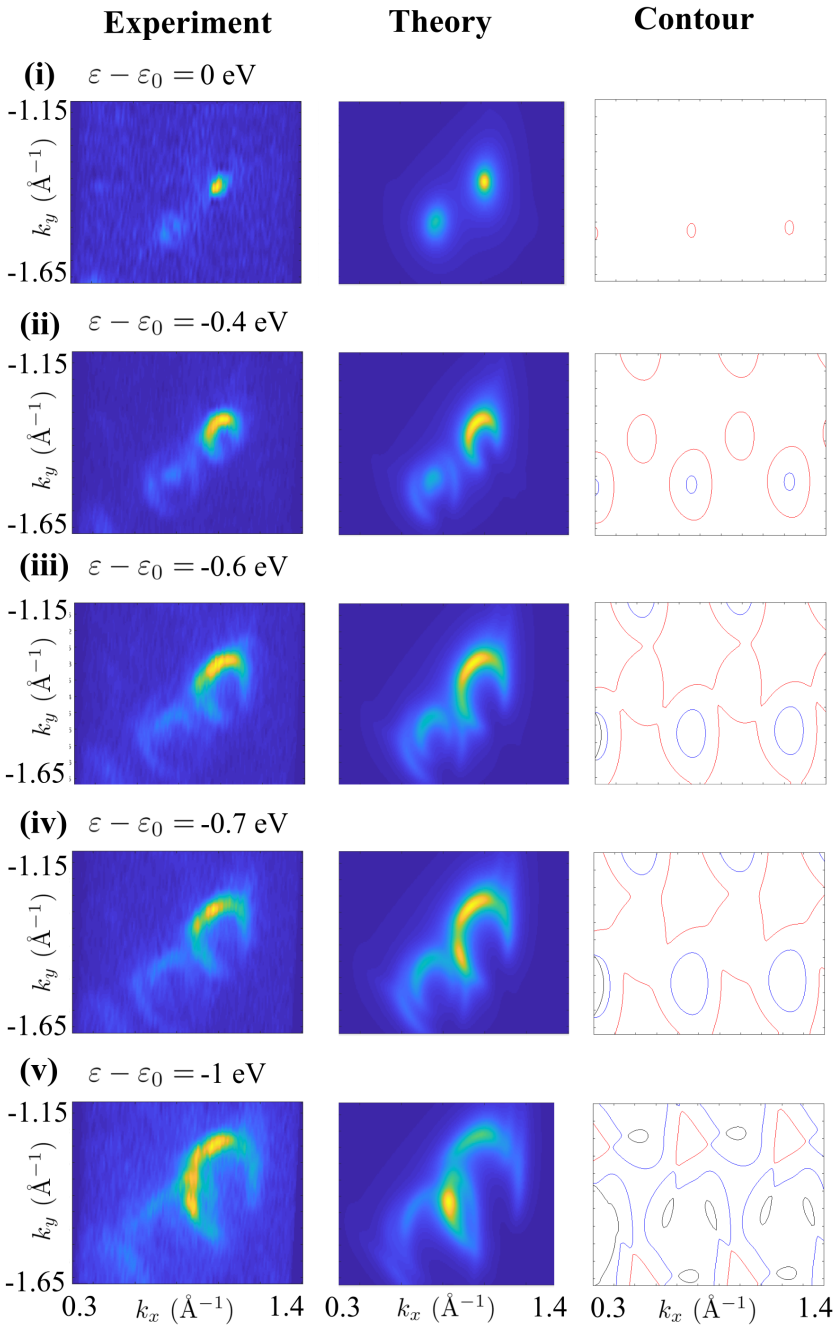


**Figure 5.6:** (Colour Online) The left column shows the experimental ARPES spectra at constant energies for sample 2: (i) $\varepsilon - \varepsilon_0 = 0$ eV, (ii) $\varepsilon - \varepsilon_0 = -0.4$ eV, (iii) $\varepsilon - \varepsilon_0 = -0.6$ eV, (iv) $\varepsilon - \varepsilon_0 = -0.7$ eV and (v) $\varepsilon - \varepsilon_0 = -1$eV. The intensities are normalised in each row. The middle column shows the corresponding normalised theoretical ARPES spectrum calculated using parameters discussed in table 1, broadening of $\gamma = 0.17$ eV and decay of $\alpha = 0.2$. The right column displays the corresponding constant energy contours obtained from the band structure using the same parameters. Counting downwards, the first, second and third valence bands are shown in red, blue and black respectively.

band gap through examination of the low energy features of the parabolic bilayer band.

In Fig 5.6, we plot, with respect to the monolayer neutrality point, the same energy contours as in Fig. 5.4. In part (i), we observe two point-like regions in the ARPES map corresponding to the monolayer Dirac point and slightly below the bilayer neutrality point. Again, the monolayer feature is visible because of broadening in the ARPES spectra, indicated by the fact that the energy contour at the corresponding region of intensity is point-like and thus not visible. In part (ii), at energy $\varepsilon - \varepsilon_0 = -0.4$ eV, we observe the higher energy band in the Bernal-bilayer part indicating that we are probing below $-\gamma_1$. This follows since we assume that $\gamma_1 = 0.39$ eV and that the neutrality point of bilayer lies above $\varepsilon_0$. The intensity at this point is observed in the theoretical model and this is further emphasised by the contour plot. Moreover, we show the energy bands at $-0.6$ eV and $-0.7$ eV in part (iii) and (iv) respectively, with both contours positioned between the split bands as a result of the interlayer coupling. In part (v), we see the emergence of the third valence band (black line in contour plot) seen as a faint ring-like shape between the two Dirac points, which arises as a result of the hybridisation between the graphene Dirac cone and the high energy band in Bernal bilayer.

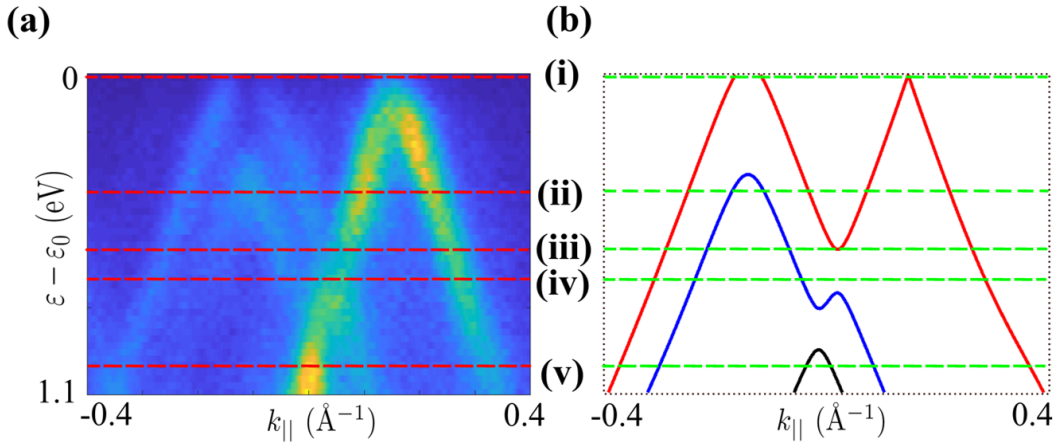


**Figure 5.7:** (Colour Online) (a) Normalised ARPES spectra for sample 2, measured along the vector connecting Dirac points. The red dashed lines, labelled (i) - (v), correspond to the constant energy cuts shown in Fig 5.6. (b) Calculated band structure along the same vector, using fitting parameters shown in Table (5.1). The dashed lines (shown in green for clarity) correspond to those in (a).

Fig. 5.7 (a) shows the ARPES spectrum and band structure along the vector connecting the two Dirac points in sample 2 at a range of energies. The calculated band structure at these points is compared in Fig. 5.7 (b). Similarly to sample 1, good agreement is shown with our model by reproducing both $\gamma_1$ and

$\tilde{t}(\boldsymbol{q}, d_0)$. However, due to the anomalous doping, one should bear in mind that the estimation of $u_1$, $u_2$ and $u_3$ is more difficult and the band structure could potentially be different. Despite this, the uncertainty is likely smaller than is resolvable via ARPES hence our fit serves as a good approximation.

## 5.5 Summary

In conclusion, we have demonstrated that the theoretical model used to describe interlayer coupling can reproduce experimental ARPES spectra. The positioning of the high energy bands originating from bilayer as well as the split bands due to hybridisation suggests our estimations for $\gamma_1$ and $t(\boldsymbol{R})$ are accurate in both samples of trilayer, and that the resulting parameter set $\tilde{t}(\boldsymbol{q}, d_0)$ is applicable for a range of angles. We explained how the self-consistency of this parameter set links the real=space tight-binding and reciprocal space continuum model We discussed the possible reasons for differences between the intensities in the experimental and theoretical ARPES energy maps, and that this was likely due to some dynamical effect. Interestingly, the substrate-doping effect in trilayer appears reversed between the two samples, suggesting that defects present in the growth or surface roughness of the copper substrate plays a role.

## 5.A ARPES in twisted bilayer

In this section, we apply the equations derived in the previous section to model ARPES in twisted bilayer and compare to experimental data provided by collaborators. From Eq. (3.5) we calculate the wavefunction distribution on the sublattice basis $(A1, B1, A2, B2)$ and use these coefficients to calculate the matrix element associated with ARPES. We plot energy slices of the ARPES spectra at 19.1° for a range of photon energies in Fig. 5.8. The ARPES spectra in Fig. 5.8 (a) demonstrates the two points of characteristic linear dispersion close to the Dirac points. The separation in momentum space between these two cones gives information about the twist angle, however at lower energies, further from the neutrality point, band hybridisation as a result of the interlayer coupling leads to modification of these bands. One should also note that the Dirac cones become "trigonally-warped" [47]. This arises as a result of the second order terms in the expansion of $f(\boldsymbol{k})$ in Eq. (2.14) and would not be present if we took the low-energy approximation of the graphene band structure.

Experimental data obtained by collaborators is shown in the left column of Fig. 5.8 and compared to our theoretical model in the right column of Fig. 5.8. Good agreement is shown in terms of the shape particularly at lower energies. At large energies deviation is observed, this could be due to terms not included in our model for monolayer graphene, such as next-nearest neighbour hopping. We note that non-zero $u$ needs to be included in our theoretical model in order to match the experimental data.

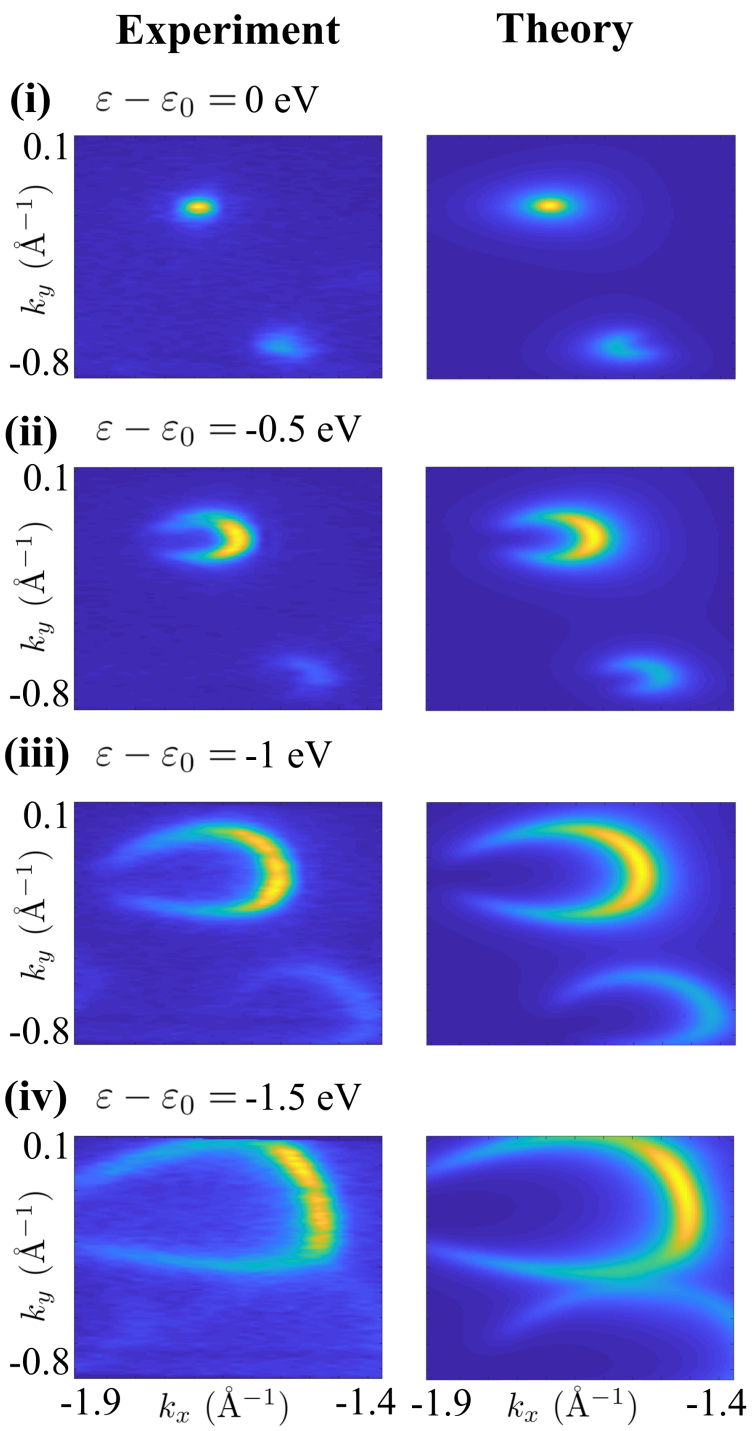


**Figure 5.8:** (Colour Online) The left column shows the experimental ARPES spectra at constant energies for twisted bilayer graphene at twist angle 19.1°: (i) $\varepsilon - \varepsilon_0 = 0$ eV, (ii) $\varepsilon - \varepsilon_0 = -0.5$ eV, (iii) $\varepsilon - \varepsilon_0 = -1$ eV, (iv) $\varepsilon - \varepsilon_0 = -1.5$ eV. The intensities are normalised in each row. The right column shows the corresponding normalised theoretical ARPES spectrum where $\gamma = 0.17$ eV and decay of $\alpha = 0.2$. The difference between the on-site energies of the two layers was estimated to be 0.2 eV.

# Chapter 6

# Negative differential resistance in van der Waals heterostructures

*Parts of this chapter were published in our articles*:

- *Negative Differential Resistance in van der Waals Heterostructures Due to Moiré-Induced Spectral Reconstruction*, D.J Leech, J.J.P.Thompson, M.Mucha-Kruczyński, Phys. Rev. Appl. **10**, 034014 (2018) [1].
- *Valley-polarized tunnelling currents in bilayer graphene tunnelling transistors*, J.J.P.Thompson, D.J. Leech, M.Mucha-Kruczyński, Phys. Rev. B **99**, 085420 (2019) [2].

*Some of the work presented in this chapter was done in collaboration with D.J. Leech who was responsible for the implementation of the MATLAB code in the case of hBN (Section 6.4) and twisted bilayer (Section 6.5). Therefore, some results presented in this chapter (in particular Section 6.4 and 6.5) have already been submitted for examination for the award of Doctor of Philosophy by D. J. Leech, awarded in 2018. My contribution involved derivation of the electrostatic and tunnelling models, code debugging, the calculation and implementation of the* $\alpha - In_2Te_2$ *tunnelling current (Section 6.6) as well as the general interpretation of results.*

## 6.1 Introduction

The phenomenon of negative differential resistance (NDR) is a striking example of nonlinearities in physics — within a certain region of the current/voltage characteristic of a device, increase of applied voltage leads to decrease of the output current. In the first solid state device displaying NDR, the Esaki diode [127], this effect arises because increasing bias voltage modifies alignment of the occupied and empty electronic states in the source and drain electrodes separated by a tunnelling barrier. At zero and large bias, either due to the lack of occupied states at the source or empty states at the drain, this alignment prohibits flow of current. In contrast, within a certain bias window in between these two cases, the positioning of energy levels allows electrons to tunnel through the barrier.

We present a plot of the current-voltage characteristics of the Esaki diode in Fig. 6.1, where it is clear that after increasing the bias voltage, $V_b$, above some critical voltage, $V_C$, the current begins to decrease. We present schematics of the Esaki diode at different voltage in panels (i)-(iii) of Fig. 6.1. The Esaki diode consists of an $n$-type and $p$-type semiconductor separated by some tunnelling barrier. At zero bias, Fig. 6.1 (i), the two Fermi levels, $\mu_n$ and $\mu_p$, are aligned such that no electrons can tunnel. As the bias voltage increases, a capacitance shifts

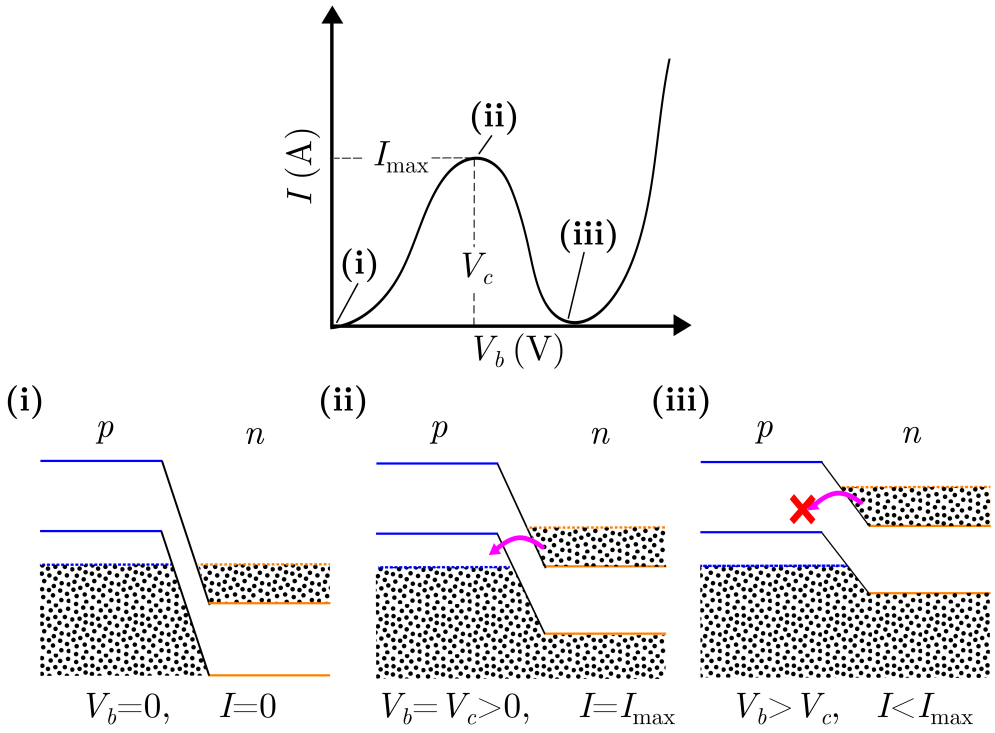


**Figure 6.1:** (Top) Typical current voltage statistics for an Esaki diode. For the points (i) to (iii), labelled on the curve, we plot a schematic of the energy bands in the $p$-$n$ tunnel junction. The band edges of the $p$-type ($n$-type) semiconductors are shown with solid blue (orange) lines while the dashed lines in blue (orange) represent the Fermi energy in the respective electrode. Black dots indicate filled electronic states. As the bias voltage is increased from (i) to (ii), electrons can tunnel across the barrier, shown with the pink arrow. At (iii), the absence of states to tunnel into is expressed with the red cross.

the $n$-type band structure up in energy relative to the $p$-type semiconductor, misaligning their Fermi levels such that occupied states in the $n$-type electrode can tunnel across the barrier into empty states in the $p$-type electrode, leading to positive current. This is presented in Fig. 6.1 (ii). However, increasing the bias voltage further shifts these bands so much that the filled states in the $n$-type semiconductor are at the same energy as the band gap in the $p$-type semiconductor, as shown in Fig 6.1(iii) . This lack of available unoccupied states leads to a decrease in the tunnelling current, despite an increased bias voltage.

Negative differential resistance has many practical applications within circuits. In particular, NDR enables the conversion of DC power into an amplification in AC signals suggesting uses in both amplifiers and oscillators [127, 128, 129]. This naturally follows from the expression for power loss, $P_{\text{Loss}}$, for an AC current

tuned to the negative differential resistance region

$$P_{\text{Loss}} = \Delta V \Delta I = \Delta R |\Delta I|^2 < 0 \tag{6.1}$$

The negative sign of $P_{\text{Loss}}$ suggests that for a small voltage increase, $\Delta V$, the decrease in resistance, $\Delta R$, leads to a small power gain within this region of the circuit and hence an amplification of the output AC circuit (this power comes from the rest of the circuit).

More recently, negative differential resistance was observed in van der Waals heterostructures of two-dimensional atomic crystals as a result of momentum-conserving electron tunnelling through an atomically thin barrier [78, 130, 131, 132, 133, 134]. Due to the high quality of the crystals produced by mechanical exfoliation and the atomically sharp interfaces in the assembled VdW-coupled stack [135], the requirement to match both energy and momentum of the initial and final states leads to a peak in the tunnelling current as applied voltages tune the source and drain to a particular band alignment. However, exfoliation, while providing state-of-the-art materials and devices, is not a scalable fabrication method. At the same time, materials produced by other methods such as chemical vapour deposition do not achieve the quality necessary to observe momentum-conserving tunnelling and seemingly NDR [136, 137].

Here, we show theoretically that NDR can be achieved in VdW heterostructures without momentum-conserving tunnelling. Instead, we exploit modifications of the electronic band structure of such heterostructures due to the interplay between lattice constants as well as misalignment of the crystallographic axes of two neighbouring layers, which lead to the formation of a superlattice at the interface. This superlattice is commonly referred to as the moiré pattern and is unique to VdW heterostructures in which, due to the van der Waals coupling between different materials, lattice matching is not necessary for the whole structure to be stable. Crucially, formation of the moiré superlattice is often accompanied by the modification of the electronic band structure as the moiré periodicity folds the dispersion into minibands. This results in opening of mini gaps at the boundary of the superlattice Brillouin zone and appearance of Van Hove singularities in the electronic density of states [28, 32, 54, 58, 60, 63, 64, 84, 89, 138, 139, 140]. We simulate the tunnelling current in two common VdW heterostructures in which the source electrode is either (1) monolayer graphene highly aligned with underlying hexagonal boron nitride (hBN) or (2) twisted bilayer graphene and show that moiré-induced spectral changes can result in negative differential resistance. We then study a more complex device with both the source and drain electrodes

made of a moiré-forming stack. We show that in the case of graphene/$\alpha - In_2Te_2$ electrodes, NDR an order of magnitude larger than for the two previous architectures is possible, suggesting that design of new van der Waals interfaces can provide a way to engineer current characteristics of tunnelling junctions, including NDR.

## 6.2 Vertical tunnelling in two-dimensional heterostructures

Electron tunnelling through a potential barrier is one of the most widely known physical consequences of quantum mechanics, responsible for effects as varied as nuclear fusion in stars, radioactive decay or spontaneous DNA mutation [141]. In particular, the probability of successful tunnelling decays exponentially with the width of the barrier, an effect best visualized in scanning transmission microscopy where moving the conducting tip away from the sample leads to rapidly decaying tunnelling currents, hence allowing for imaging of the corrugation of the sample surface [142]. In order to find the tunnelling current through a van der Waals heterostructure, we use Bardeen's formalism [143, 144, 145, 146, 147, 148], which utilises the wave functions of the source and drain electrodes to model the tunnelling probability. The matrix element, $M(\varepsilon)$, associated with the probability of an electron with energy $\varepsilon$ tunnelling through the barrier (which we take to lie in the $xy$-plane), is calculated (up to some constant prefactor with dimension of energy $\times$ distance) as

$$M \propto \int \left[ \Psi_{\mathrm{s}}(\boldsymbol{r}, \varepsilon) \frac{\partial \Psi_{\mathrm{d}}^*(\boldsymbol{r}, \varepsilon)}{\partial z} - \Psi_{\mathrm{d}}(\boldsymbol{r}, \varepsilon) \frac{\partial \Psi_{\mathrm{s}}^*(\boldsymbol{r}, \varepsilon)}{\partial z} \right] dV, \tag{6.2}$$

where $\Psi_{\mathrm{s}}$ ($\Psi_{\mathrm{d}}$) describes the wave function on the source (drain) electrode and the integration is over the volume of the tunnelling junction.

We model the transverse component of the wave functions, $\phi_{\mathrm{s}}(z, \varepsilon)$, as exponentially decaying,

$$\phi_{\mathrm{s}}(z, \varepsilon) \propto e^{-c(\varepsilon)(|z - z_{\mathrm{s}}|)}, \tag{6.3}$$

where $c(\varepsilon)$ is the decay constant associated with $p_z$ orbital decay through the tunnelling medium and $z_{\mathrm{s}}$ is the $z$-position of the source electrode[1]. We do not

[1] Although the normalisation of this wavefunction is not explicitly stated, it varies as $\sqrt{c(\varepsilon)}$, much more slowly than the exponent $e^{-c(\varepsilon)(|z - z_s|)}$.

seek to model the exact magnitudes of tunnelling currents, but rather relative magnitudes. A schematic of the tunnelling setup is presented in Fig. 6.2 with the transverse component of the source and drain electrodes shown in blue and orange respectively.

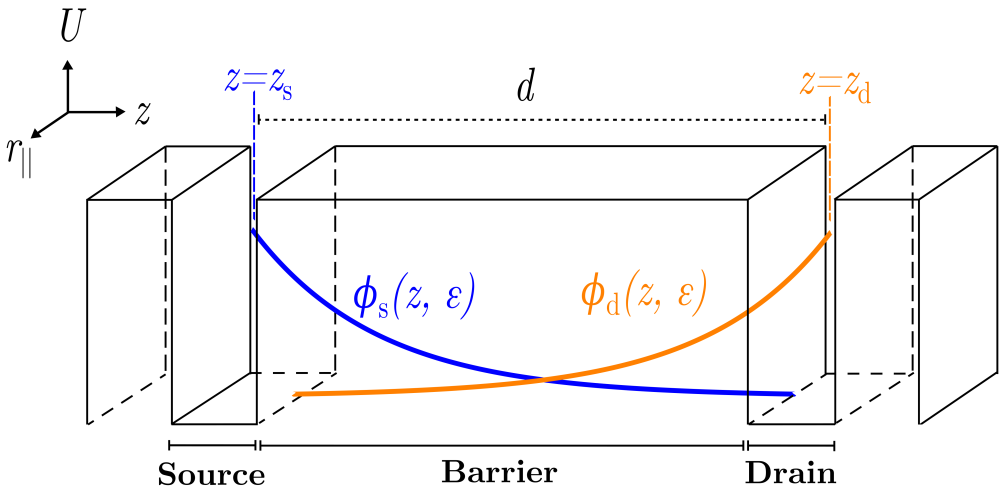


**Figure 6.2:** Tunnelling wave functions for the source (blue) and drain (orange) electrodes on a three-dimensional energy landscape, magnitude $U$, with the axis shown in the top left. The source and drain wave functions decay exponentially along the $z$-axis and are centred on $z_s$ and $z_d$ respectively. The electrodes are separated by distance $d$, the length of the tunnel barrier. $\boldsymbol{r}_{||}$ is a one-dimensional representation of the $xy$-plane.

The density of states (DOS) of a material determines the number of electronic states per unit energy, with flat energy bands generating strong peaks in the density of states forming Van Hove singularities (as alluded to in previous sections). The current $I$ across the tunnel barrier is sensitive to the source and drain density of states [149], $\rho_s$ and $\rho_d$, respectively,

$$I = \frac{2g\pi e}{\hbar}\int M(\varepsilon)\rho_s(\varepsilon)\rho_d(\varepsilon-\Delta) \times [f(\varepsilon-\mu_s)-f(\varepsilon-\Delta-\mu_d)]d\varepsilon, \tag{6.4}$$

where the energy $\epsilon$ is measured from the source charge neutrality point, $\mu_s$ and $\mu_d$ determine the energy distance between the chemical potential and the charge neutrality points in the source and drain electrode, respectively, $\Delta$ is the shift between the source and drain neutrality points so that $\mu_s$ and $\mu_d + \Delta$ are the chemical potentials in the corresponding electrodes, $M$ is the matrix element, $f(\epsilon)$ is the Fermi-Dirac distribution (here, we take the low-temperature limit) and $g$

takes into account additional degeneracies of the electronic states (here, spin and valley). In this chapter, we ignore the in plane contribution of the wavefunctions to the matrix element $M(\varepsilon)$ due to the absence of momentum-conserving tunnelling - this might be the case for devices of insufficient quality or large misalignments between the crystallographic directions of the electrodes. Note that, if the momentum-conserving tunnelling processes become important, their contribution cannot be larger than the currents discussed here, because ultimately the number of tunnelling electrons is set by the corresponding DOS whereas momentum conservation adds an additional constraint that is only sometimes fulfilled. In Chapter 7 we shall discuss another application of van der Waals tunnelling transistors where strong momentum conservation is crucial.

### 6.2.1 hBN as a tunnel barrier

A typical van der Waals tunnel barrier will consist of a few layers of hBN [131, 133, 143, 144, 150]. Although this layered structure implies some periodic barrier height, previous work has shown [143] that a layered structure can be modelled as if it were a continuous tunnelling barrier and we thus treat it as an isotropic potential step with barrier height $\Phi_0 = -1.5$ eV, corresponding to experimental measurements of the valence band maximum (VBM) of hBN [143, 151]. The hBN energy dispersion around the VBM is roughly parabolic in $k_z$ and this allows us to write [146]

$$c(\varepsilon) = \mathrm{Im}\frac{\sqrt{2m^*\Phi(\varepsilon)}}{\hbar} = \mathrm{Im}\frac{\sqrt{2m^*(\Phi_0 - \varepsilon)}}{\hbar}, \tag{6.5}$$

where $m^* \approx 0.5m_0$ is the effective mass [16, 143, 151]. Notably, this relation predicts weak electron-hole asymmetry in tunnelling current as observed in experiment [143, 152]. For hBN, experimental works [134, 136, 137, 143, 144, 150] suggest a value of the decay constant $c(0) \approx 5$ nm$^{-1}$. Throughout this thesis, we assume that the hBN comprising the tunnel barrier is sufficiently misaligned from the two-dimensional electrodes, such that the moiré effects, discussed in Chapter 3, are negligible. In general, the variation in the electronic energy is small relative to the band gap in hBN such that the decay constant remains roughly constant in our calculations. However, in this chapter we shall include such variations in the decay constant for completeness.

## 6.3 Electrostatic model for van der Waals tunnelling transistors

In this section, we derive a general electrostatic model describing the relationship between the tuneable voltages in a typical device and the macroscopic parameters of the constituent electrodes, in particular the chemical potentials and offset between the neutrality points. The device modelled in this chapter is shown in Fig. 6.3 and is similar to previous experimental devices [131, 143, 144].

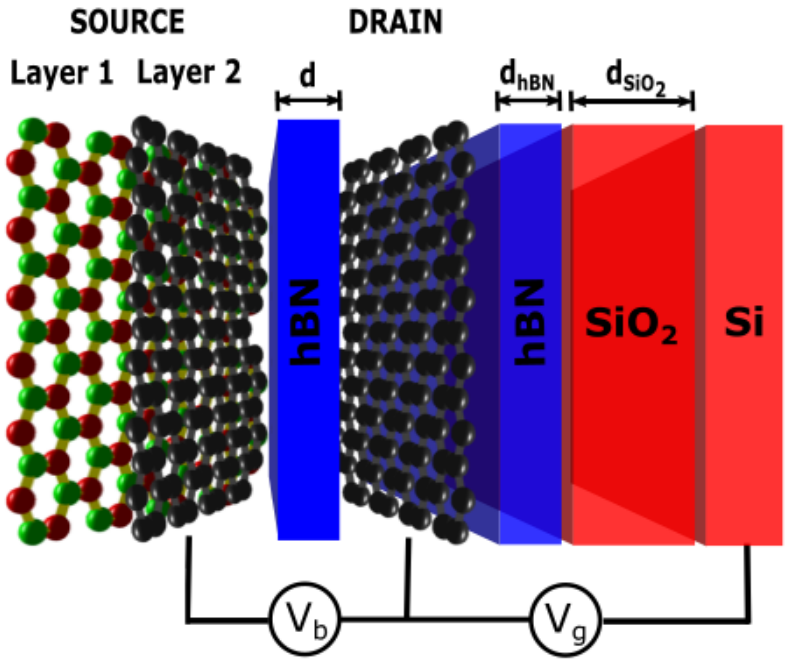


**Figure 6.3:** Schematic of the tunnelling device with a source made of an aligned graphene/hBN heterostructure. Also shown is the barrier width, $d$ and width of the substrates, $d_{\mathrm{hBN}}$ and $d_{\mathrm{SiO_2}}$ as well as contacts for the voltages $V_b$ and $V_g$. This figure was published in Physical Review Applied [1].

Electrodes, labelled the source and drain, sit either side of a three-layer hBN tunnel barrier, with a bias voltage, $V_b$ applied between them. The source electrode consists of two layers with layer 1 (the layer furthest from the barrier) generating a long-wavelength periodic potential for electrons in layer 2. In this section, we assume that layer 2 will always be a graphene monolayer while the choice of material for layer 1 discussed in this chapter are primarily those discussed in Chapter 3: twisted graphene, aligned hBN and aligned $\alpha - \mathrm{In_2Te_2}$. The hBN in the tunnel barrier is sufficiently misaligned so as to avoid additional superlattice

effects between it and the source/drain electrodes. The drain electrode consists of a single graphene layer. A thick hBN layer of length $d_{\mathrm{hBN}} = 30$ nm lies underneath the drain electrode to ensure the electronic quality of graphene [17]. A silicon back gate, separated by a $SiO_2$ substrate of thickness $d_{\mathrm{SiO_2}} = 150$ nm, is placed beneath the thick hBN layer. A gate voltage, $V_g$ applied between the back gate and the drain electrode, enables the tuning of the total charge density on the device. The bias voltage $V_b$ and gate voltage $V_g$ control the local Fermi levels, $\mu_S$ and $\mu_D$, in the source and drain respectively, as well as the shift between the neutrality points, $\Delta$. In the case of a tBLG electrode, the applied voltages induce an interlayer asymmetry, $u$. The Fermi levels and vertical shift of the energy bands would be controlled via a bias $V_b$ and gate voltage $V_g$ in an experimental setup. We use a four-plate capacitor model to express the electric fields between the gates and consecutive graphene layers (we treat hBN and $SiO_2$ as homogeneous insulators with dielectric constants $\epsilon_{\mathrm{hBN}}$ and $\epsilon_{\mathrm{SiO_2}}$, respectively). The charge densities per graphene layer on the source ($j = \mathrm{s}$) or MLG drain ($j = \mathrm{d}$) electrodes can be expressed as

$$n_j(\mu_j) = \int D_j(\varepsilon) f(\varepsilon, \mu_j, T) d\varepsilon, \tag{6.6}$$

where $f(\varepsilon, \mu_j, T)$ is the Fermi-Dirac distribution at temperature T. At low temperature the Fermi-Dirac distribution can be approximated as a step, meaning the bounds for integration become

$$n_j(\mu_j) = \int_0^{\mu_j} D_j(\varepsilon) d\varepsilon, \qquad T \to 0\,\mathrm{K}. \tag{6.7}$$

Through charge conservation, for each combination of $\mu_{\mathrm{s}}$, $\mu_{\mathrm{d}}$ and $u$, we obtain corresponding bias and back gate potentials. Furthermore, the charge build up on the bilayer sheet acts as a capacitance leading to a difference in neutrality points of the two spectra

$$\Delta = \varepsilon_0^{\mathrm{s}} - \varepsilon_0^{\mathrm{d}}. \tag{6.8}$$

For simplicity we set $\varepsilon_0^{\mathrm{s}} = 0$ and therefore, using Gauss's law, the position of the charge neutrality point in monolayer is related to the number of excess charge carriers in the bilayer graphene by relation

$$E_0^{\mathrm{d}} = \Delta = \frac{e^2 d}{\epsilon_0 \epsilon_{\mathrm{hBN}}} \left( n_d(\mu_d) + n_{\mathrm{Si}} \right), \tag{6.9}$$

where $e$ is the electronic charge, $\epsilon_0$ is the permitivitty of free space, $\epsilon_{\mathrm{hBN}} = 3.9$ is

the relative permitivitty of hBN and $n_{\mathrm{Si}}$ is the carrier density on the silicon back gate. The voltages of the system can therefore be expressed as

$$\begin{aligned} V_b &= \frac{1}{e}\left(\mu_s - \mu_d - \Delta\right), \\ V_g &= -\frac{e(n_d(\mu_d)+n_s(\mu_s,u))(d_{\mathrm{SiO_2}}\epsilon_{\mathrm{hBN}}+d_{\mathrm{hBN}}\epsilon_{\mathrm{SiO_2}})}{\epsilon_{\mathrm{hBN}}\epsilon_{\mathrm{SiO_2}}\epsilon_0}, \end{aligned} \tag{6.10}$$

where $\epsilon_{\mathrm{SiO_2}}$ is the relative permitivitty of $SiO_2$. In the case of a bilayer graphene source electrode, the induced gap leads to the modulation of the density of states and thus the charge density. We calculate the gap self-consistently, using the following expression

$$u = \frac{e^2 d_0}{\varepsilon_0}\left(n(\mu_d) + \frac{1}{2}n(\mu_s,u) + n_{\mathrm{Si}}\right), \tag{6.11}$$

where $d_0$ is the interlayer distance in bilayer graphene. We assume that the distribution on the two layers is roughly equal at the voltages given[2].

## 6.4 Graphene on hBN

We first investigate the possibility of superlattice-induced NDR for a source electrode composed of hBN (layer 1) and monolayer graphene (layer 2). As the perturbing effect of hBN on graphene electrons decreases with increasing misalignment between the two crystals [33, 54], we assume their crystalline axes are highly aligned. In such a case, the conical dispersion of graphene in the vicinity of the Brillouin zone (BZ) corner (valley) is folded into minibands with the valence band undergoing a more significant spectral modification than the conduction band [57], including the appearance of a Van Hove singularity (VHS) in the DOS [32, 57, 153]. Using the perturbation Hamiltonian, Eq. (3.25), the change in density of states is presented in Fig. 6.4 where we show that under the effect of a moiré perturbation, the flat band forming leads to the generation of a peak in the density of states. The sharp peak in the DOS arising as a result of this perturbation is highlighted in red in Fig. 6.4 over a small window in $V_b$.

In Fig. 6.5, we present our simulation of the tunnelling current between the graphene/hBN source and graphene drain as a function of the voltages $V_b$ and $V_g$ for the device setup presented in Fig. 6.3. The appearance of NDR can be seen in the top right quarter of Fig. 6.5 (a) where the tunnelling current decreases with

[2]We will show in the next chapter that, in the presence of a magnetic field, non-zero $u$ leads to strong symmetry breaking in the density of states of the two layers, meaning a more thorough calculation is required.

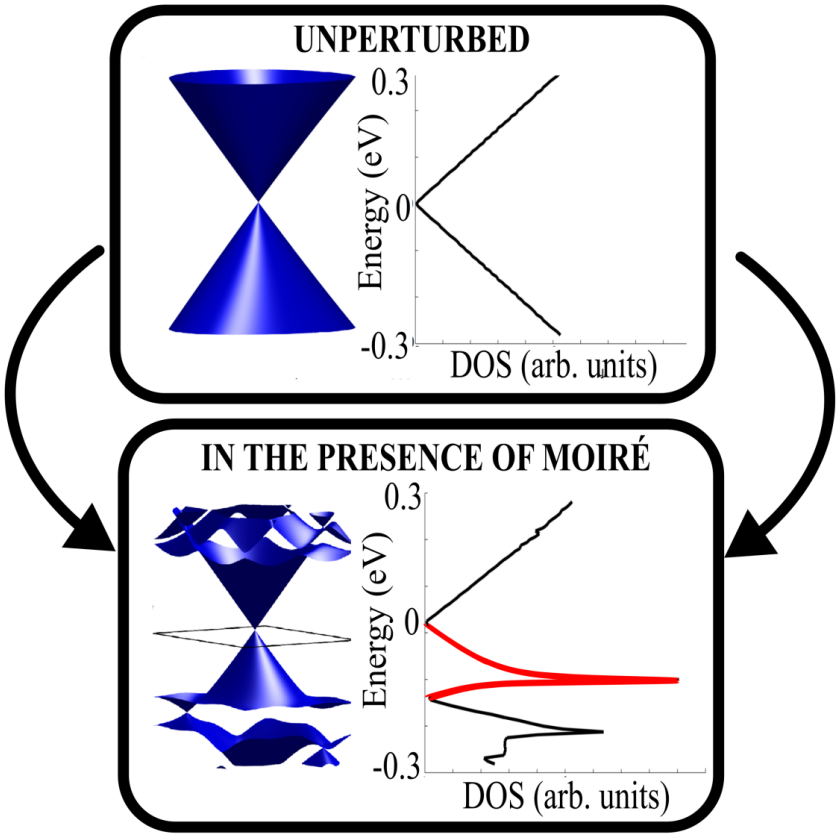


**Figure 6.4:** The conical bands and density of states of unperturbed monolayer graphene (top) and corresponding graphene minibands and density of states of an aligned graphene/hBN heterostructure (bottom). In the miniband spectrum, the black lines indicate the boundaries of a rhombic superlattice Brillouin zone. The perturbation is modelled using the Hamiltonian and parameter set outlined in Chapter 3. The Van Hove singularity in the density of states of the heterostructure is highlighted in red. This figure was published in Physical Review Applied [1].

increasing bias voltage. We show selected cuts through that region for various constant values of $V_g$ in Fig. 6.5 (b).

For $V_b = V_g = 0$ V, the chemical potentials in the source and drain are located at the respective neutrality points which are aligned with each other, as in diagram (I) in Fig. 6.5 (c), hence leading to an absence of tunnelling current. Applying the bias voltage introduces a relative shift between the source and drain chemical potentials $\mu_s$ and $\mu_d + \Delta$, respectively. As a result, an increase in $V_b$ for $V_g = 0$ V (corresponding to following the orange dashed line in Fig. 6.5 (a) and 6.5 (b)) leads to an increasing current as electrons from the valence band in the source can tunnel into the empty conduction band states of the drain. For $V_b$ slightly above 0.2 V, $\mu_d + \Delta$ moves past the moiré-induced VHS in the source

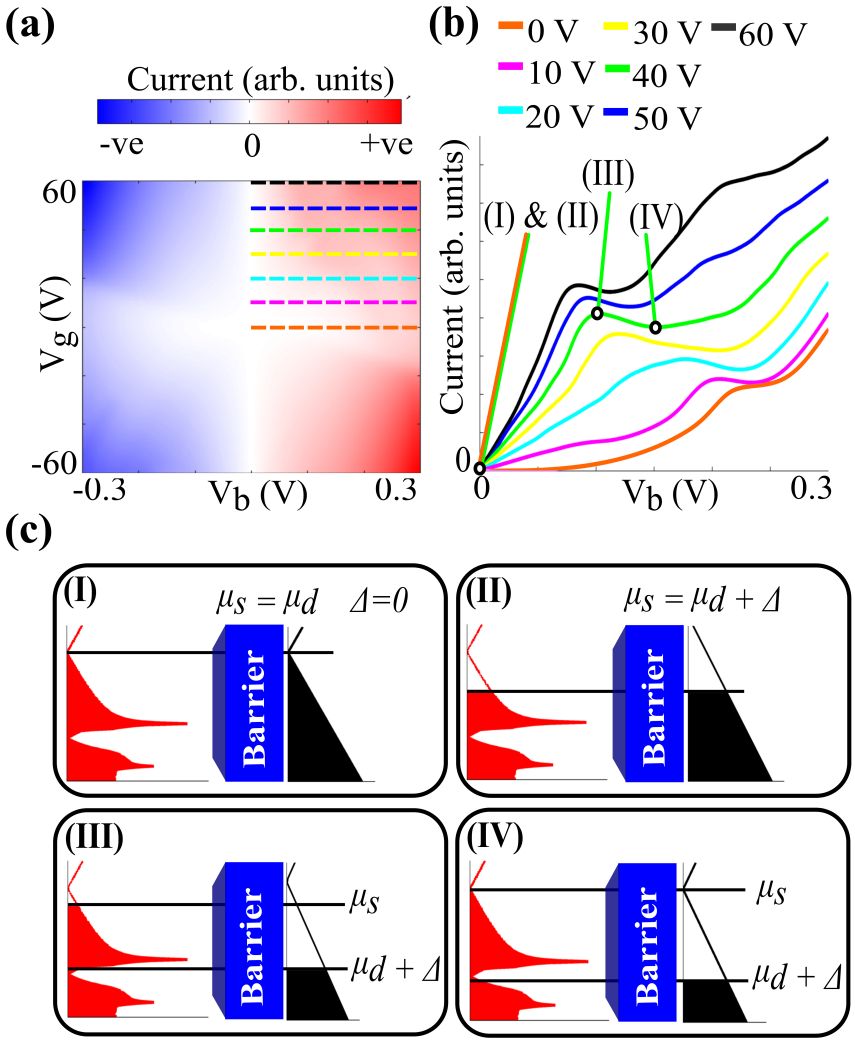


**Figure 6.5:** (a) Calculated tunnelling current for a device from Fig. 6.3 as a function of voltages $V_g$ and $V_b$. (b) Tunnelling current as a function of $V_b$ for constant $V_g$ from 0 V (orange) to 60 V (black) in steps of 10 V, with labels above. The cuts in $(V_g, V_b)$ space corresponding to current curves in (b) are shown with dashed lines in (a). (c) Diagrams showing alignment of source and drain density of states as well as the positions of chemical potentials $\mu_s$ and $\mu_d + \Delta$ for points in $(V_g, V_b)$ space corresponding to tunnelling currents marked in (I), (II), (III) and (IV) in (b). This figure was published in Physical Review Applied [1].

valence band which leads to a shoulder-like feature in the orange curve in Fig. 6.5 (b).

In contrast, applying the gate voltage $V_g$ at constant $V_b$ dopes source and drain without affecting the energy difference between the chemical potentials, $\mu_s$ and $\mu_d + \Delta$. As shown in diagram (II) in Fig. 6.5 (c), for $V_g = 40$ V and $V_b = 0$ V no current flows through the structure because the chemical potentials are aligned, as in (I). Again, the current increases with increasing bias (as demonstrated by the

green curve in Fig. 6.5 (b)) until it reaches a peak when the occupied states in the moiré-induced VHS are aligned with empty states in the drain valence band, as in diagram (III). Because the VHS in the source DOS is followed by a dip, increasing $V_b$ further does not lead to more occupied electronic states contributing to the tunnelling. However, because changing $V_b$ affects the energy shift $\Delta$ between the Dirac points of the source and drain through Eq. (6.10), the number of empty states aligned with the VHS actually decreases with increasing $V_b$, as seen by comparing diagrams (III) and (IV). This results in a decrease of the current and NDR. Increasing $V_b$ further leads to an even larger tunnelling energy window such that, eventually, the current begins to increase again.

## 6.5 Twisted bilayer graphene

To demonstrate the generality of our idea, we now discuss the existence of NDR in a twisted bilayer graphene/hBN/monolayer graphene van der Waals tunnelling transistor.

For our modelling of the tunnelling between tBLG and graphene across a hBN multilayer, we choose the misalignment angle 2°, corresponding to the low-energy band structure in the vicinity of a single valley and density of states as shown in Fig. 6.6 (a). All the other geometrical parameters of the device are as used in the case of the graphene/hBN source electrode. The calculated current as a function of the bias and gate voltages $V_b$ and $V_g$ is shown in Fig. 6.6 (b) and selected cuts for constant $V_g$ are presented in Fig. 6.6 (c). Similarly to the case of the graphene/hBN electrode, superlattice-induced changes in the energy spectrum, in particular the presence of sharp VHSs followed by a dip, leads to NDR for a range of gate voltages.

Because the VHS is a robust feature in the density of states of tBLG for a large range of misalignment angles [58], the behaviour of the tunnelling current should also be similar for different $\theta$ (although note that greater misalignment angle requires higher $V_g$ to dope the source past the singularity). Since the density of states of tBLG is electron-hole symmetric, in contrast to the aligned graphene/hBN heterostructure, the graph in Fig. 6.6 (b) is inversion-symmetric with respect to the point $V_b = V_g = 0$ V.

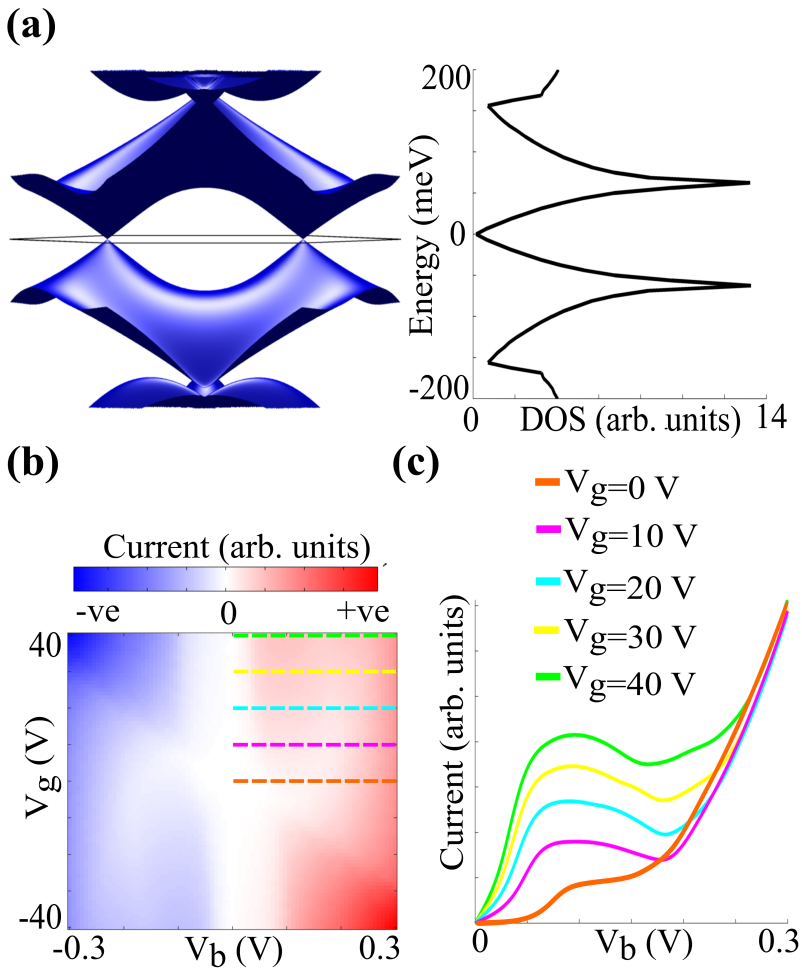


**Figure 6.6:** (a) Low-energy band structure and density of states for twisted bilayer graphene with a misalignment angle of 2°. Note that both the position and height of the VHS change with misalignment angle. The black line indicates the superlattice Brillouin zone edge. (b) Tunnelling current from tBLG to graphene across a hBN barrier as a function of gate and bias voltages $V_g$ and $V_b$. (c) Tunnelling current as a function of $V_b$ for constant $V_g$ from 0 V (orange) to 40 V (green) in steps of 10 V. The cuts in $(V_b, V_g)$ space corresponding to the current curves in (c) are shown with dashed lines in (b). This figure was published in Physical Review Applied [1].

## 6.6 Graphene on $\alpha - In_2Te_2$

While the architectures discussed in Section 6.4 and 6.5 demonstrate the principle of moiré-induced NDR and are feasible experimentally, the calculated NDR peak-to-valley ratio is only of order 1. It can be increased by choosing a different VdW heterostructure as an electrode, in particular, one with a moiré reconstructed density of states in which a bandgap between minigaps is close to a Van Hove singularity. Moreover, designing superlattices to modulate the densities of

states of both the electrodes as opposed to using monolayer graphene with its linear DOS as a drain like in the two examples earlier, will also increase NDR.

Hence, in this section, we investigate current characteristics of a VdW tunnelling transistor with both electrodes made of graphene on $\alpha - In_2Te_2$. Since $\alpha - In_2Te_2$ is an insulator and monolayer, the addition of this extra layer has negligible effect on the electrostatic calculation, other than altering the DOS. The corresponding DOS is shown in Fig. 6.7 (b), containing Van Hove singularities next to a window of zero density of states, features attractive for an increased NDR. In Fig. 6.7 (c), we present the current calculated as a function of the gate and bias voltages for a VdW tunnelling transistor incorporating the graphene/$\alpha - In_2Te_2$ heterostructures as both source and drain (all other parameters of the device are kept the same as in Section 6.4 and 6.5). Current curves for selected constant gate voltages and changing bias are shown in Fig. 6.7 (d) (region of positive $V_g$ and $V_b$) and Fig. 6.7 (e) (region of negative $V_g$ and $V_b$). For easier comparison with other figures in this paper, we have reversed the current and bias voltage axes in Fig. 6.7 (e). Moreover the current scale in Fig. 6.7 (d) has been scaled by a factor of 3 as compared to Fig. 6.7 (e).

All of the I-V characteristics in Fig. 6.7 (d) and 6.7 (e) show NDR peak-to-valley ratios ranging from 2 to 10, depending on the choice of gate voltage. The largest NDR of around 10 is that for $V_g = 0$ V (orange curve) in Fig. 6.7 (d). This peak-to-valley ratio is competitive when compared to commonly used NDR devices, typically in the range of 3-35 [154, 155]. In our device, this NDR results from the presence of two Van Hove singularities in the DOS around zero energy (see Fig. 6.7 (b)) and their movement on the energy scale in the source/drain electrodes as a function of $V_b$.

## 6.7 Summary

In summary, we demonstrated theoretically for three different architectures that the modifications of the electronic density of states due to the formation of moiré superlattices of van der Waals crystals can lead to negative differential resistance when the moiré heterostructure is employed as an electrode in a vertical tunnelling transistor. This is achieved without the requirement of momentum-conserving tunnelling, which has only been observed in the highest quality, closely-aligned, devices, made of mechanically exfoliated crystals. For this reason, our idea might be useful for materials produced by other methods like chemical vapour deposition, where clear moiré-induced spectral modification

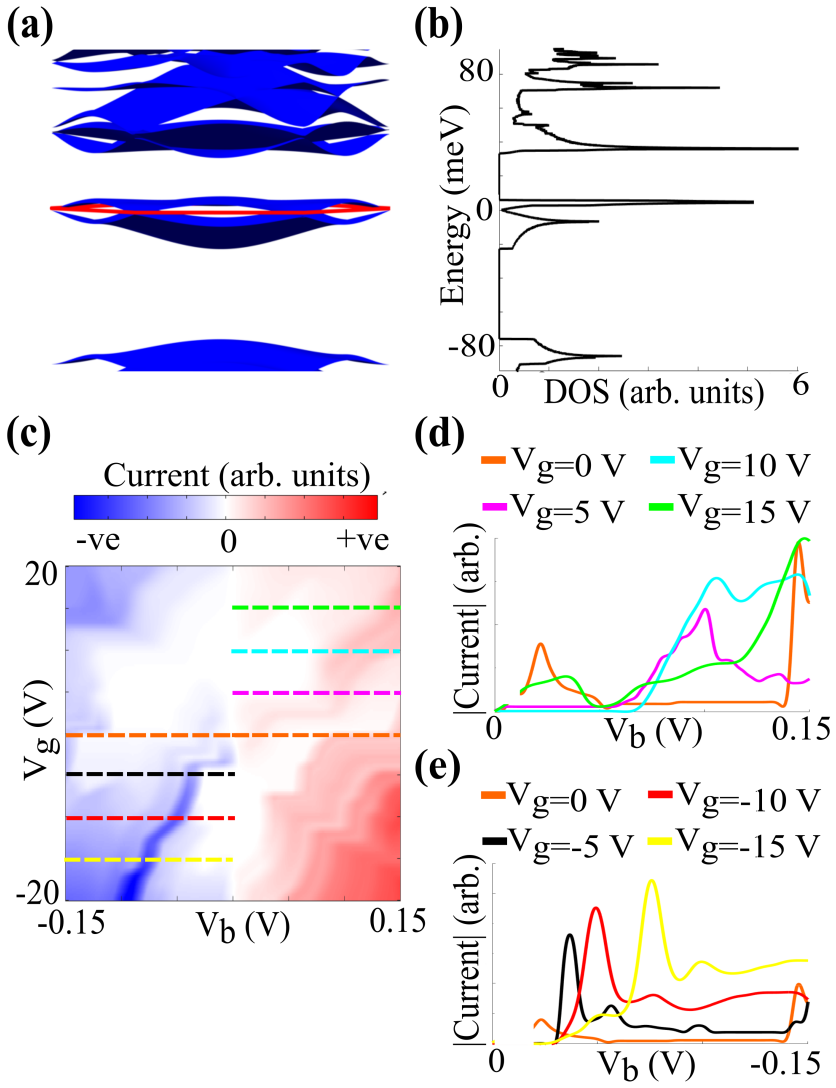


**Figure 6.7:** (a) Low-energy band structure of graphene on aligned $\alpha - In_2Te_2$. The outline of the superlattice Brillouin zone is shown in red for clarity. (b) Corresponding density of states. (c) Tunnelling current between two graphene on aligned $\alpha - In_2Te_2$ electrodes across a hBN barrier as a function of gate and bias voltages $V_g$ and $V_b$. (d) Absolute tunnelling current as a function of $V_b$ for constant $V_g$ from 0 V (orange) to 15 V (green) in steps of 5 V. The cuts in $(V_b, V_g)$ space corresponding to the current curves in (d) are shown with dashed lines in (c). The current lines in (d) are scaled to highlight NDR features. (e) Same as (d) except for negative gate and bias voltages with steps of -5 V from 0 V (orange) to -15 V (yellow). This figure was published in Physical Review Applied [1].

has been observed [28, 156] but no momentum-conserving tunnelling has been reported. While the moiré superlattices used in the first two examples, graphene on hBN and twisted bilayer graphene, have been realised experimentally, the last one, graphene on $\alpha - In_2Te_2$, has not. However, superlattice effects have been observed or predicted for a variety of different heterostructures and interfaces

[35, 157, 158, 159], so that significant NDR peak-to-valley ratio might indeed be possible for certain architectures, as suggested in Section 6.6. Importantly, in contrast to artificial superlattices, our idea avoids the need to process any of the two-dimensional crystals after they are grown, as the superlattice is provided by an interface between neighbouring layers. This, in turn, limits disorder and degradation of the components, especially important if the starting materials were not obtained by mechanical exfoliation. In contrast to many other NDR setups, our idea is, by design, easy to integrate in more complicated devices based on two-dimensional crystals and VdW interfaces. It can also be coupled with artificial patterning of dielectric substrates underneath 2D materials on length scales comparable to moiré wavelengths [160].

# Chapter 7

# Valley-polarised tunnelling currents in bilayer graphene tunnelling transistors

*Parts of this chapter were published in our articles*:

- *Valley-polarized tunnelling currents in bilayer graphene tunnelling transistors*, J.J.P.Thompson, D.J. Leech, M.Mucha-Kruczyński, Phys. Rev. B **99**, 085420 (2019) [2].

*Some of the work presented in this chapter was done in collaboration with D.J. Leech who was responsible for implementation of MATLAB code, in particular the procedure for obtaining the chemical potentials from the applied voltages. Therefore, some results presented in this chapter, in particular Section 7.3, have already been submitted for examination for the award of Doctor of Philosophy by D. J. Leech. My contribution involved derivation of the electrostatic and tunnelling models, the derivation of the Landau levels wavefunctions and the resulting tunnelling matrix element, MATLAB debugging, implementation of the results presented in Section 7.4 and data analysis.*

## 7.1 Introduction

Exploiting alternative degrees of freedom of an electron, rather than just the electronic charge, allows novel methods of storing, transferring and manipulating information. Spintronics [161, 162] is one example of this, where the up and down spins encode binary information. Another, more recent example of encoding information is known as "valleytronics" [163], where information is defined based on the discrete region near band extrema in reciprocal space (valley) from where the electron hails. As introduced in Chapter 2, graphene has two distinct sets of valley points, labelled $\boldsymbol{K}_+$ and $\boldsymbol{K}_-$, which are occupied by low energy electrons, such that the relative population of both these valleys could be used to encode information. In this chapter, we show that by placing a van der Waals tunnelling transistor, similar to that discussed previously, in a perpendicular magnetic field, significant valley polarisation can be generated. Van der Waals tunnelling transistors with ultra-high quality interfaces display momentum-conserving tunnelling leading to negative differential resistance [130, 131, 132, 133, 144, 164] and valley polarization due to an in-plane magnetic field [134]. It was also shown that electron tunnelling in vdW heterostructures can be accompanied by excitation of various quasiparticles, for example, phonons [165] or magnons [166] and influenced by defects in the tunnel barrier [167, 168].

Here, we study theoretically the tunnelling current flowing between bilayer graphene (BLG) and monolayer graphene (MLG) electrodes through a hBN barrier, in the presence of a magnetic field perpendicular to the atomic layers. The

impact of the applied magnetic field is two-fold: firstly, the electronic density of states is modified due to Landau quantisation and second, layer polarisation of the low-energy Landau levels in BLG [23] leads to the efficient generation of valley polarisation [163, 169]. We show here that valley polarisation of order unity is possible, in magnetic fields as low as $\sim 1$ T, and that choice of the valley quantum number of the tunnelling current can be made electronically without reversing or changing the magnitude of the magnetic field. While the largest valley polarisation can be achieved in high quality devices in which tunnelling electrons conserve both energy and momentum, our results suggest that even in the absence of momentum conservation, polarisation $\sim 80\%$ can be achieved at $B = 1$ T.

## 7.2 Device description and tunnelling matrix element

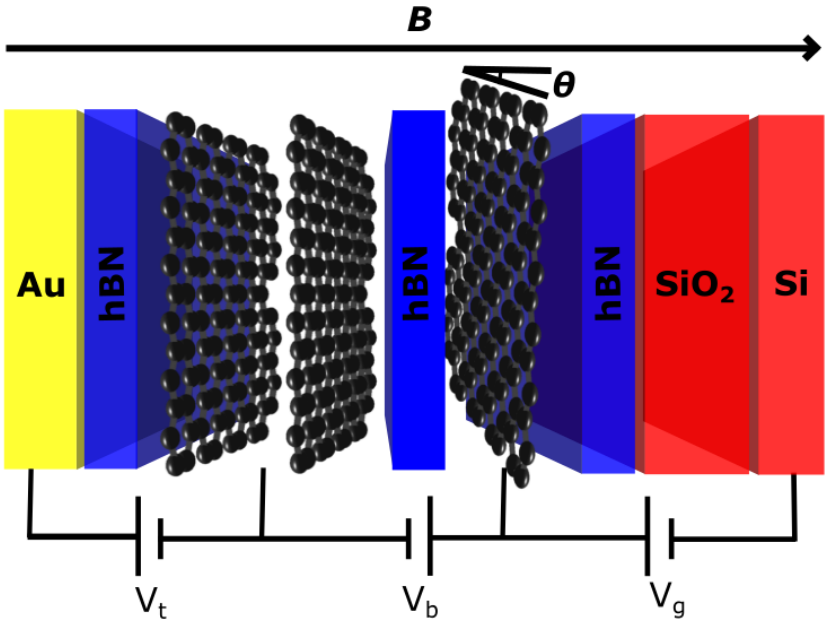


**Figure 7.1:** (Color online) Schematic of the tunnelling device discussed here. Also shown are the tuning potentials $V_b$, $V_g$ and $V_t$ and direction of the applied magnetic field $B$. This figure was published in Physical Review B [2].

The schematic of the device we study is shown in Fig. 7.1 with the assumed direction of the magnetic field, $B$. The device is similar to that used in Chapter 6 with a few changes. First, the source electrode consists of Bernal bilayer graphene, while the drain electrode is comprised of monolayer graphene. Second,

the thickness of the $SiO_2$ is increased to $d_{SiO_2} = 300$ nm, allowing finer control over the doping[1]. Additionally, a gold top gate is attached to the source electrode, to allow further control over electrostatic parameters. This top gate is separated from the source electrode by $d_{\text{Top}} = 30$ nm of hBN, with a voltage, $V_t$ applied between them[2]. The BLG and MLG electrodes can be rotationally misaligned so that their crystallographic directions are rotated by an angle $\theta$ [139]. Following experimental device architectures [17, 131, 134], we assume that both MLG and BLG are encapsulated with hBN. We additionally assume that the misalignment between graphene electrodes and hBN (both the barrier as well as the top and bottom encapsulating layers) is large so that moiré effects like miniband formation [54] or lattice relaxation [31], important for highly-aligned interfaces [33], can be neglected.

The tunnelling matrix element can be modelled using Eq. (6.2). In a multilayer electrode, such as bilayer graphene, the overall wave function can be described as a linear combination of the wave functions on the constituent layers. Therefore, in the case of an $N$-layer source electrode we can write

$$\Psi_{\text{s}}(\boldsymbol{r}, \varepsilon) = \sum_{i=1}^{N} n_i \psi_{\text{s},i}(\boldsymbol{r}, \varepsilon), \tag{7.1}$$

where $\psi_{\text{s},i}$ is the electronic wave function of the $i$-th layer of the source electrode and $|n_i|^2$ describes the relative occupation of the $i$th layer by an electron in state $\Psi_{\text{s}}$.

Assuming a clean sample, all $\Psi_{\text{s}}(\boldsymbol{r}, \varepsilon)$ are separable into the in-plane and perpendicular components, $\Psi_{\text{s}}(\boldsymbol{r}, \varepsilon) = \varphi_{\text{s}}(x, y, \varepsilon)\phi_{\text{s}}(z, \varepsilon)$. This enables us to decompose the matrix element, Eq. (6.2), into transverse, $z$, and in-plane, $x, y$, components. We model the transverse components using an exponential decay, as discussed in Eq. (6.3), only with certain caveats. In our case, there are two materials to consider: hBN, comprising the tunnelling barrier, and graphene. We assign to them decay constants $c(\varepsilon)$ and $c'(\varepsilon)$, respectively (the decay constants vary as a function of the tunnelling state energy $\varepsilon$ [146]). With these assumptions, we integrate the expression in Eq. (6.2) in the direction transverse to the barrier. For our BLG source electrode which consists of two graphene layers, the electrons from the layer closest to the barrier tunnel directly to the drain, pass-

[1]The carrier density in a capacitor is less sensitive to the voltage if the insulator thickness is larger.

[2]Both gold and silicon, separated from the electrodes by an insulating layer are effective gating materials, however the results presented in this chapter are unaffected by the materials used assuming they are first, not insulators and second, the carrier density of these materials is much larger than in the source and drain electrodes.

ing only through one material, hBN. However, the electrons in the layer further from the barrier have to travel an increased distance. Since there are no available states on the other graphene layer the electrons have to pass through, it can be effectively treated as an insulator and so the only mechanism for transport is tunnelling. Integrating over the total width of the barrier [3] for these electrons, defined as the sum of the hBN barrier width, $d = 13$ Åand the interlayer separation of graphene, $d_0 = 3.3$ Å, we obtain an expression depending only on the in-plane components of the wave function and energy,

$$M(n_1, n_2, \varepsilon) \propto e^{-c(\varepsilon)d}\Bigg[\int \varphi_{\mathrm{D}}^{*}(x, y, \varepsilon) \cdot \begin{pmatrix} n_1 & n_2 e^{-c'(\varepsilon)d_0} \end{pmatrix} \cdot \begin{pmatrix} \varphi_{\mathrm{S},1}(x, y, \varepsilon) \\ \varphi_{\mathrm{S},2}(x, y, \varepsilon) \end{pmatrix} dA\Bigg], \tag{7.2}$$

where we have absorbed all normalisation factors into $\varphi_{\mathrm{s},i}(x, y, \varepsilon)$ and used the fact that in our device the drain electrode is built of only one layer and the source of two layers. Note that the expression in Eq. (7.2) conserves the in-plane electron momentum in the tunnelling process, as is the case in experiments performed on the highest quality devices [130, 131, 144, 164]. This momentum conservation is encoded in the real space integration over the in-plane harmonic oscillator states, $\varphi_{\mathrm{S,D}}$ on the source and drain electrode respectively which manifests in a Landau level index and rotational misalignment angle dependence in the matrix element (outlined later in Fig. 7.2).

While the argument above can be extended to any number of layers in both the source and drain electrodes, the exponential dependence of tunnelling probability on the barrier width means that only tunnelling from/into the first few layers next to the barrier is measurable. As discussed in the previous chapter, experimental works [134, 136, 137, 143, 144, 150] suggest a value of the decay constant $c(0) \approx 5$ nm$^{-1}$. In the case of graphene, studies of its role as a barrier in magnetic tunnel junctions [170, 171, 172] and between metal contacts [173, 174] showed that it behaves as a strong out-of-plane insulator. In fact, in experiments conducted in the absence of a magnetic field and in the presence of a field parallel to the graphene layers, the measured tunnelling current has been well described by assuming that all tunnelling from the further BLG layer is suppressed

[3] In Eq. (6.2) care must be taken to describe the wave functions of the $p_z$ orbitals in graphene within regions of different materials, which, based on experiment, leads to different decay constants. Therefore, the integration becomes a sum of integrals over these different regions (in our case hBN and graphene).

[134, 164]. For this reason, here, we take the limit $c' = c$, corresponding to the decay through graphene being significant and similar to that through hexagonal boron nitride. However our conclusions hold for notably smaller $c'$ (we discuss what happens for differing estimates of $c'$ in Appendix 7.A).

In both MLG and BLG, the wave functions are distributed asymmetrically between the two sublattices concerned ($A$, $B$ in MLG and $A1$, $B2$ in BLG). In particular, the electrons in the $n = 0$ MLG level and $m = 0, 1$ BLG states occupy only one of the sublattices[4]. For the case of BLG, this results in two states that in the $\boldsymbol{K}_+$ valley are located only on layer 1 and in the $\boldsymbol{K}_-$ valley only on layer 2. We define layer 1 (2) in BLG as the layer closer (further) to the tunnelling barrier such that, in the vertical tunnelling transistor geometry like in Fig. 7.1, we expect electrons from layer 2 to have a smaller chance of tunnelling through the barrier than electrons from layer 1, due to the additional effective barrier thickness. As a result, more electrons from BLG $\boldsymbol{K}_+$ valley will tunnel through than from the $\boldsymbol{K}_-$ valley, leading to valley-polarized current arriving in the MLG drain electrode.

In order to quantify valley polarisation of the tunnelling current, we use the wave functions from Eq. (2.41) and (2.38) to compute the tunnelling matrix element, Eq. (7.2). The Landau level wave functions of BLG are already written so that their components correspond to different layers and we can identify the states in Eq. (2.41) with $(\varphi_{\mathrm{S},1}(x, y, \varepsilon),\ \varphi_{\mathrm{S},2}(x, y, \varepsilon))^T$ in Eq. (7.2). However, although the MLG wave functions are also written as spinors in Eq. (2.38), both of their components correspond to wave function amplitudes on sublattices in the same layer. Hence, for a given Landau level state we take $\varphi_D = \chi_A + \chi_B$, where $(\chi_A,\ \chi_B)^T$ is the corresponding spinor in Eq. (2.38).

In a system containing both monolayer and bilayer graphene in the presence of a magnetic field, the theoretical description presented in the previous subsections is sufficient. However, when one of these elements is rotated about the $z$-axis relative to the other, keeping to a fixed frame of reference means modification of the Hamiltonian is required to accurately describe the resulting electronic wavefunctions.

We consider a monolayer graphene electrode misaligned compared to the origin axis (in this case a bilayer graphene electrode). A small anticlockwise rotation of the MLG sheet about the $z$-axis by angle $\theta$, leads to an identical rotation between the corresponding Brillouin zones. As a result of this rota-

[4]The single-sublattice occupation of the $n = 1$ BLG Landau level is not preserved beyond the low-energy two-band model we use here [175]. However, it remains a good approximation for the magnetic fields considered here.

tion, the position of MLG valley centres is offset from that of BLG by a vector $\boldsymbol{\Delta K_\xi} = \left(\Delta K_\xi^x, \Delta K_\xi^y\right) = (\hat{\mathbf{1}} - \hat{\boldsymbol{R}}_{\boldsymbol{\theta}})\boldsymbol{K_\xi}$, where $\hat{\boldsymbol{R}}_{\boldsymbol{\theta}}$ is the anti-clockwise rotation operator. Taking into account this shift as well as the rotation between the two materials, electrons in the MLG electrode are described by a Hamiltonian

$$\hat{\boldsymbol{\mathcal{H}}}_{\text{Rot,MLG}} = v \begin{pmatrix} 0 & (\hat{\boldsymbol{\pi}}^\dagger + \widetilde{\hat{\boldsymbol{\pi}}}^\dagger)e^{-i\theta} \\ (\hat{\boldsymbol{\pi}} + \widetilde{\hat{\boldsymbol{\pi}}})e^{i\theta} & 0 \end{pmatrix}, \tag{7.3}$$

where $\widetilde{\hat{\boldsymbol{\pi}}} = \hbar(\Delta K_\xi^x + i\Delta K_\xi^y)$. Furthermore the displacement of the momentum-origin changes the unrotated harmonic oscillator state, Eq. (2.36), into $\tilde{\phi}_n(x)$,

$$\begin{aligned} \tilde{\phi}_n(x) = A_n \exp\left[-\frac{1}{2\lambda_B^2}(x-\tilde{X})^2 - i\Delta K_\xi^x(x-\tilde{X})\right] \\ \times \mathcal{H}_n\left(\frac{1}{\lambda_B}(x-\tilde{X})\right), \end{aligned} \tag{7.4}$$

and shifts the cyclotron orbits to $\tilde{X} = \lambda_B^2(k_y + \Delta K_\xi^y)$. Therefore, the wave function corresponding to the $n$-th Landau level in rotated MLG can be written as

$$\begin{aligned} \tilde{\psi}_0 &= \begin{pmatrix} \tilde{\phi}_0 \\ 0 \end{pmatrix} e^{ik_y y}, \\ \tilde{\psi}_{n,s'} &= \frac{1}{\sqrt{2}} \begin{pmatrix} \tilde{\phi}_n \\ -s' i e^{i\theta}\tilde{\phi}_{n-1} \end{pmatrix} e^{ik_y \cdot y}, \qquad n \geq 1. \end{aligned} \tag{7.5}$$

The matrix element determining the tunnelling between the BLG and MLG electrodes depends on the Landau level indices, $n, m$, as well as the magnetic field, $B$, and misalignment angle between the two sheets, $\theta$. For the $\boldsymbol{K}_+$ valley, it can be written as

$$\begin{aligned} M^{s',s}_{n,m,K_+}(\varepsilon) = \frac{V_0 P_{n,m}}{\sqrt{2}} e^{-c(\varepsilon)d} \\ \times \Big[ C_1 \Lambda^\xi_{n,m} - s' i e^{i\theta} C_1 \Lambda^\xi_{n-1,m} \\ + e^{-c'(\varepsilon)d_0} \left( C_2 \Lambda^\xi_{n,m-2} - s' i e^{i\theta} C_2 \Lambda^\xi_{n-1,m-2} \right) \Big], \end{aligned} \tag{7.6}$$

whereas, for the $\boldsymbol{K}_-$ valley, we obtain

$$M^{s',s}_{n,m,K_-}(\varepsilon) = \frac{V_0 P_{n,m}}{\sqrt{2}} e^{-c(\varepsilon)d} \times \Bigg[ C_2 \Lambda^{\xi}_{n,|m|-2} + s' i e^{-i\theta} C_2 \Lambda^{\xi}_{n-1,m-2} + e^{-c'(\varepsilon)d_0} \left( C_1 \Lambda^{\xi}_{n,m} + s' i e^{-i\theta} C_1 \Lambda^{\xi}_{n-1,m} \right) \Bigg]. \tag{7.7}$$

In both cases we define

$$C_1 = \begin{cases} \dfrac{\varepsilon^0_m}{\sqrt{C}} & m \neq 0, 1 \\ 1 & m = 0, 1 \end{cases},$$

$$C_2 = \begin{cases} \dfrac{\left[\varepsilon_{m,s,\xi} - \xi\frac{u}{2} + \xi u m \eta^2\right]}{\sqrt{C}} & m \neq 0, 1 \\ 0 & m = 0, 1 \end{cases},$$

$$\Lambda^{\xi}_{n,m} = N_{n,m} 2^{\max\{n,m\}} (\min\{n,m\})! e^{i\frac{1}{2}\Delta K^x_\xi \Delta K^y_\xi \lambda_B^2} \times \left( \mathrm{sgn}(n-m)\frac{1}{2}\lambda_B \Delta K^y_\xi - i\frac{1}{2}\lambda_B \Delta K^x_\xi) \right)^{|n-m|} \times e^{-\frac{\boldsymbol{\Delta K}^2_{\boldsymbol{\xi}} \lambda_B^2}{4}} \mathcal{L}^{|n-m|}_{\min\{n,m\}} \left( \frac{\boldsymbol{\Delta K}^2_{\boldsymbol{\xi}} \lambda_B^2}{2} \right), \tag{7.8}$$

where $N_{n,m}$ and $P_{n,m} = \sqrt{(1+\delta_{n,0})}$ are normalisation constants and $\mathcal{L}^{\beta}_{\alpha}(x)$ are generalised Laguerre polynomials. The strength of the coupling at the $\boldsymbol{K}_+$ valley, $|M^{s',s}_{n,m,K_+}|^2$, is shown for $B = 1$ T and as a function of Landau level, $n, m$, and band indices, $s, s'$, in Fig. 7.2(a) and (b) at misalignment angles $\theta = 0.25°$ and $\theta = 0.5°$ respectively.

For zero misalignment angle, the matrix element is simply a linear combination of Kronecker deltas (each expressing orthonormality of the harmonic oscillator states), suggesting only transitions between certain Landau states are allowed. However, as shown in Fig. 7.2 (a), increasing misalignment redistributes the coupling strength amongst other transitions (in particular, for any non-zero $\theta$, transitions between any two oscillator states are in principle allowed). Interestingly, changing the misalignment angle also changes the preferred transition (the one with the largest coupling strength). However, because the matrix element depends on products of the type $\boldsymbol{\Delta K}^2_{\boldsymbol{\xi}} \lambda_B^2$, a change of angle (which determines $\boldsymbol{\Delta K_\xi}$) can be to some extent counterbalanced by changing the magnetic field (and hence $\lambda_B$).

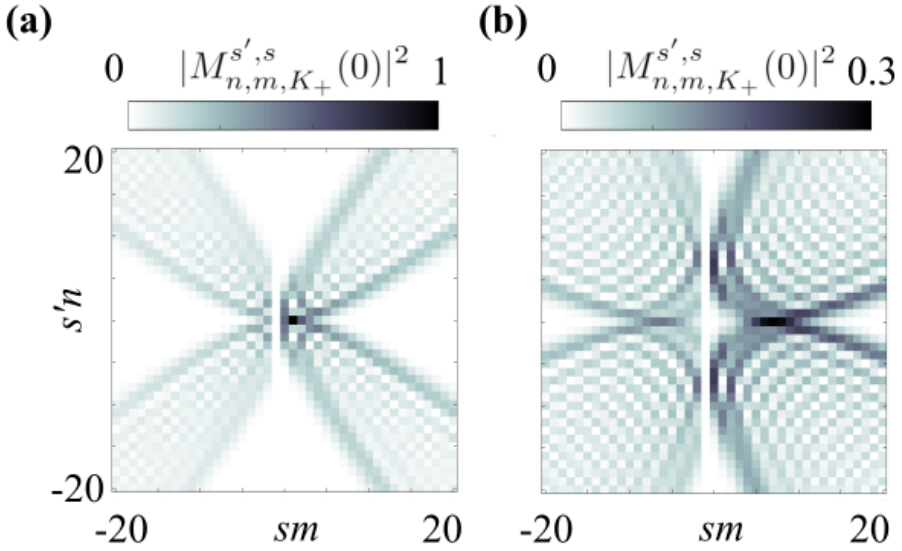


**Figure 7.2:** (Color online) Colour map of the tunnelling matrix element $|M^{s,s'}_{n,m,K_+}(0)|^2$ between Landau levels of MLG (with indices $s'n$) and gapless BLG (indices $sm$) for $B = 1$ T and (a) $\theta = 0.25°$ and (b) $\theta = 0.5°$. All values are normalised to the maximum value in (a). This figure was published in Physical Review B [2].

In clean samples, with a small misalignment angle between the source and drain electrodes the shift $\boldsymbol{\Delta K_\xi}$ is small and for all the dominant processes the valley quantum number is conserved in the tunnelling process [134, 144]. Therefore, as in Eq. (6.4), we use Fermi's golden rule to relate the tunnelling matrix element to the current of electrons originating from the $\boldsymbol{K_\xi}$ valley of BLG,

$$I_\xi = \frac{4\pi e}{\hbar} \sum_{n,m,s',s} \int_{\mu_{\rm BLG}}^{\mu_{\rm MLG}+\Delta} |M^{s,s'}_{n,m,\xi}(\varepsilon)|^2 \times D_{\rm BLG}(\varepsilon, \varepsilon_{m,s,\xi}) D_{\rm MLG}(\varepsilon - \Delta, \varepsilon_{n,s}) d\varepsilon, \tag{7.9}$$

where we have already taken the spin degeneracy into account. We measure the energy $\varepsilon$ from the charge neutrality point of the BLG electrode while $\mu_{\rm BLG}$ and $\mu_{\rm MLG}$ represent the distance in energy between the charge neutrality point and the chemical potential in the BLG and MLG electrode, respectively. An example of this is shown in Fig. 7.3, where the blue (orange) dashed line corresponds to $\mu_{\rm MLG}$ ($\mu_{\rm BLG}$). Finally, we define $\Delta$ as the shift between the source and drain neutrality points, marked with the dotted lines in Fig. 7.3, such that, in the low temperature limit, the local chemical potentials in the source and drain electrodes, $\mu_{\rm BLG}$ and $\mu_{\rm MLG} + \Delta$ respectively, determine the energy window within which tunnelling

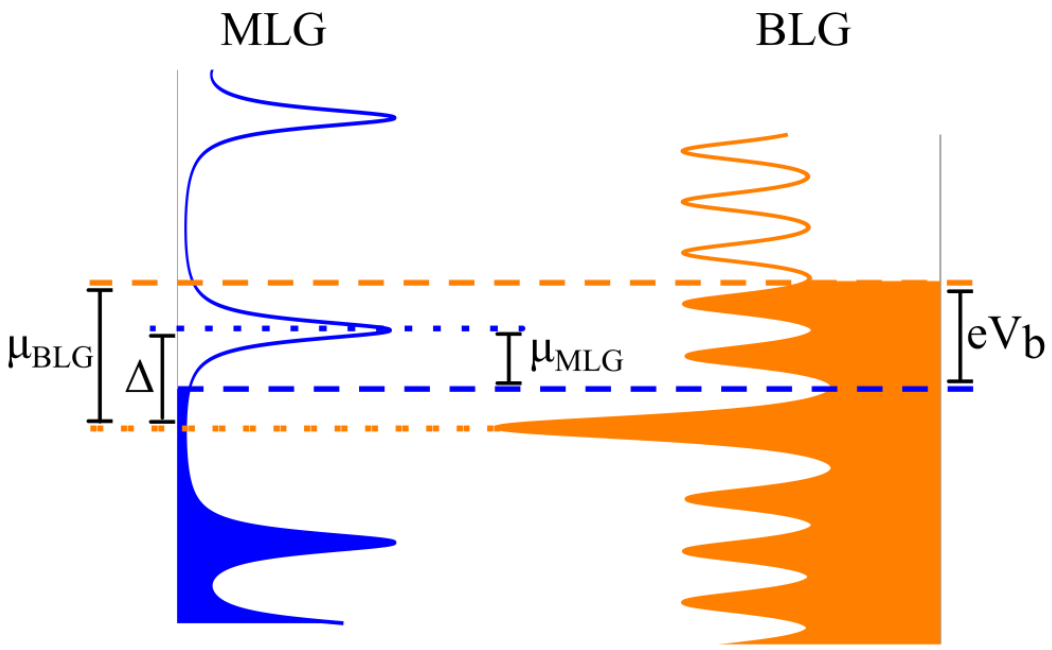


**Figure 7.3:** Illustration of the DOS of the monolayer graphene (blue) and bilayer graphene (orange) electrodes. Also indicated are the chemical potentials $\mu_{\mathrm{MLG}}$ (blue dashed line) and $\mu_{\mathrm{BLG}}$ (orange dashed line) with filled states below these values indicated by the filled DOS curves. The neutrality points are indicated by the dotted lines, with the separation between them marked by $\Delta$. The bias voltage $V_b$ is also indicated.

processes can occur, while the number of initial and final states at a given energy is provided by the densities of states $D_{\mathrm{MLG}}$ and $D_{\mathrm{BLG}}$ in the monolayer and bilayer graphene, respectively. In a device with high quality layers, free from defects and in a quantizing external magnetic field, these densities of states consist of a series of sharp peaks at the energies of the Landau levels. We model the latter using a Lorentzian shape with the same full width at half maximum for all Landau levels, 2 meV and 4 meV for $B = 1$ T and $B = 4$ T, respectively, following previous experimental works [144, 176] and theoretical considerations [177].

Finally, we define the valley polarisation, $P$, of the tunnelling current,

$$P = \frac{I_+ - I_-}{I_+ + I_-}. \tag{7.10}$$

Because our tunnelling matrix element, Eq. (6.2), is defined up to a proportionality constant, values of tunnelling current in this chapter are given in arbitrary units. Polarisation, however, as a ratio of currents, does not depend on that constant itself.

In the same way as in Chapter 4, we can relate the energies $\varepsilon$, $\mu_{\mathrm{BLG}}$ and $\mu_{\mathrm{MLG}}$

to the applied voltages $V_t$, $V_b$ and $V_g$ (see Fig. 7.1), through the electrostatic equations,

$$\begin{aligned} V_b &= \frac{1}{e}\left[\mu_{\mathrm{BLG}} - \mu_{\mathrm{MLG}} - \Delta\right], \\ V_g &= -\frac{e(n_{\mathrm{MLG}} + n_{\mathrm{BLG},u} + n_{\mathrm{Au}})(d_{\mathrm{SiO_2}}\epsilon_{\mathrm{hBN}} + d_{\mathrm{hBN}}\epsilon_{\mathrm{SiO_2}})}{\epsilon_{\mathrm{hBN}}\epsilon_{\mathrm{SiO_2}}\epsilon_0}, \\ V_t &= \frac{-en_{\mathrm{Au}}d_{\mathrm{Top}}}{\epsilon_0\epsilon_{\mathrm{hBN}}}. \end{aligned} \tag{7.11}$$

We define $n_{\mathrm{MLG}}, n_{\mathrm{BLG}}$ and $n_{\mathrm{Au}}$ as the carrier densities on the MLG, BLG and gold electrodes respectively. The distance between the gold top gate and BLG, $d_{\mathrm{Top}}$, is set as 30 nm in our numerical calculations. Furthermore, $d_{\mathrm{hBN}}$ and $d_{\mathrm{SiO_2}}$ represent the thicknesses of the hBN and $SiO_2$ substrates, which, following previous experimental works [131, 134], we set as 30 nm and 300 nm respectively. Finally, $\epsilon_0$ is the permittivity of free space while $\epsilon_{\mathrm{hBN}} \approx 3$ and $\epsilon_{\mathrm{SiO_2}} \approx 3.9$ are the relative permittivities of hBN and $SiO_2$. We also take into account that the electric field between the graphene layers of BLG induces the interlayer asymmetry $u$ which we compute self-consistently,

$$u = -\frac{e^2 d_0(n_{\mathrm{Au}} + n_{\mathrm{BLG},2}(u))}{\epsilon_0}, \tag{7.12}$$

where $n_{\mathrm{BLG},i}(u)$ is the carrier density on the $i$-th layer of BLG. For a given interlayer asymmetry, we compute the electronic wave functions for all Landau levels included in the calculation and their distributions on the atomic sites (while the number of Landau levels considered depended on the magnetic field and applied voltage range, we checked the convergence of our results in all cases). For each Landau level, we use the square of the wave function amplitude on the site $B2$ to obtain the contribution to $n_{\mathrm{BLG},2}$ from that level. We then determine the unique value of $u$ for which Eq. (7.12) is fulfilled.

## 7.3 Momentum-conserving tunnelling

### 7.3.1 Total tunnelling current at $B = 1$ T

Our simulation of the total tunnelling current, $I = I_+ + I_-$, between the BLG and MLG electrodes, produced using Eq. (7.9), is shown in Fig. 7.4. For momentum-conserving tunnelling, the strength of the coupling is dictated by the magnitude of the applied magnetic field, relative orientation of the electrodes and Landau level indices of the involved electronic states.

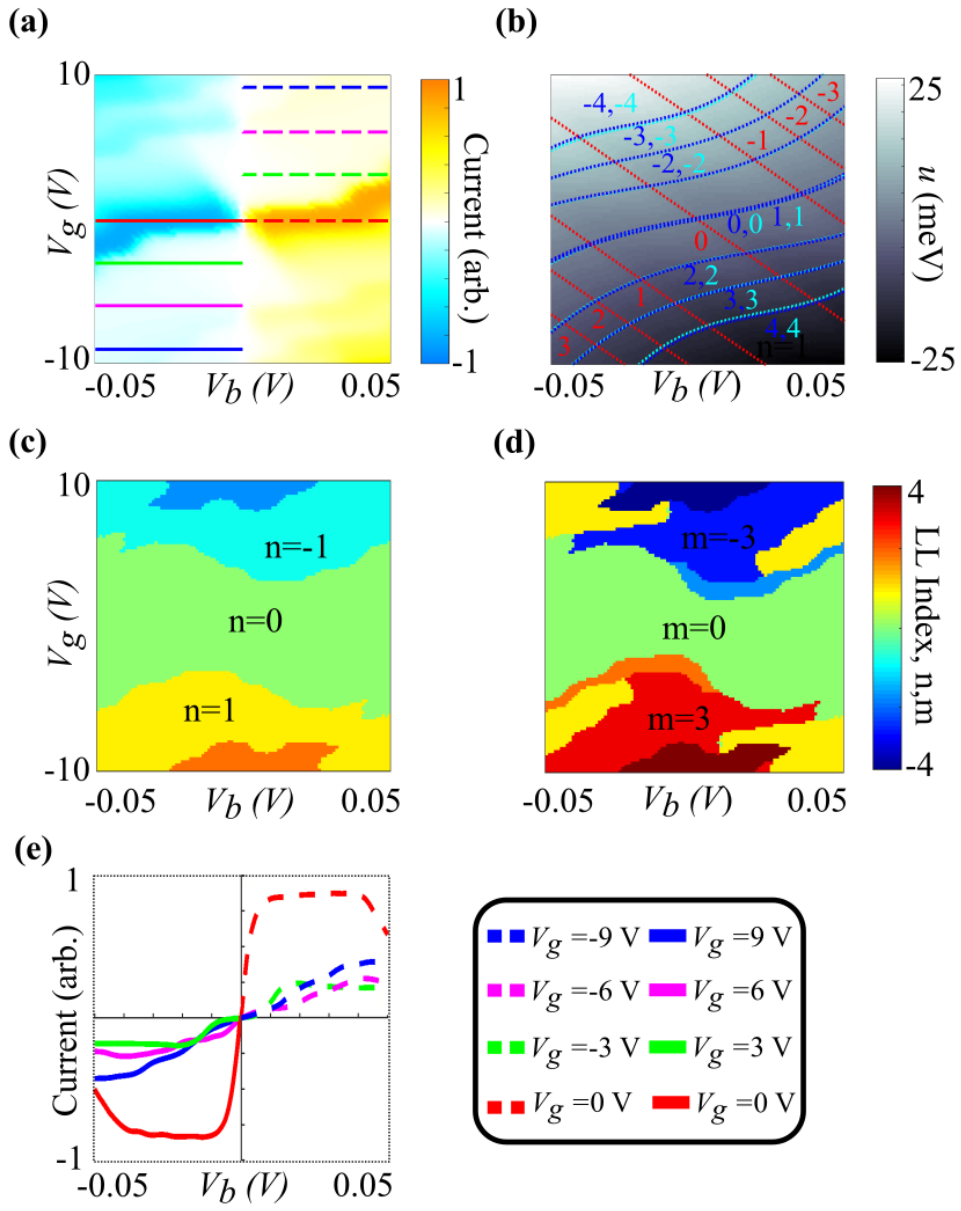


**Figure 7.4:** (Color online) Total tunnelling current at $B = 1$ T as a function of the bias and gate voltages, $V_b$ and $V_g$ for $\theta = 0°$ and $V_t = 0$ V is shown in (a). The interlayer asymmetry is plotted as a function of bias and gate voltages in (b). Red lines and labels in (b) indicate the points where $\mu_{\rm MLG}$ lies at the centre of a MLG Landau level. Blue (cyan) lines and labels in (b) indicate the points where $\mu_{\rm BLG}$ lies at the centre of a BLG Landau level in the $\boldsymbol{K}_+$ ($\boldsymbol{K}_-$) valley. The Landau levels, $n$ and $m$ providing the dominant contribution to the tunnelling current in (a) are shown in (c) and (d) respectively. Panel (e) shows current curves corresponding to the lines marked in (a), with changing $V_b$ and constant $V_g$ from -9 V to 9 V in steps of 3 V. Part of this figure was published in Physical Review B [2].

In panel (a), we show the current for $V_t = 0$ V and ideally aligned electrodes, $\theta = 0°$. For $V_g = V_b = V_t = 0$ V, the chemical potentials in the BLG and MLG electrodes, $\mu_{\rm BLG}$ and $\mu_{\rm MLG} + \Delta$, are located at their respective neutrality points, which are at the same energy, resulting in zero tunnelling current. As the bias voltage is increased, a shift between the local chemical potentials in the two electrodes is induced. This opens an energy window, within which electrons occupying states in one electrode can tunnel into empty states at the same energy in the other electrode, thus leading to a non-zero tunnelling current. The coupling strength between the initial and final states in the tunnelling process is set by $|M^{s,s'}_{n,m,\xi}(\varepsilon)|^2$ which, because of the spinorial nature of the MLG and BLG wave functions, is expressed as a sum of four terms, each of which contains an integral $\int \tilde{\phi}^*_n \phi_m dA$ of two oscillator states $\tilde{\phi}_n$ and $\phi_m$. For ideal alignment of the electrodes, $\theta = 0°$, the set $\{\tilde{\phi}_n\}$ is equivalent to $\{\phi_m\}$ and the integrals express orthonormality of functions with different indices, $\int \phi^*_n \phi_m dA = \delta_{n,m}$. As a result, tunnelling only occurs if one of the four conditions is fulfilled: i) $n = m$, ii) $n-1 = m$, iii) $n = m-2$ or iv) $n-1 = m-2$. Hence, the central region of large current in Fig. 7.4(a), for $V_g = 0$ V and non-zero $V_b$ (finger-like features between the blue (cyan) $m = 0, 1$ and $m = 2$ $(-2)$ lines in Fig. 7.4 (b)), corresponds to the coupling between $m = 0$ and $n = 0$ Landau levels in BLG and MLG respectively, as demonstrated by the Landau level maps in Fig. 7.4 (c) and (d). Although at low voltages the $m = 0$ and $m = 1$ Landau levels in BLG are degenerate, transitions between the $m = 1$ and $n = 0$ level in MLG are forbidden. Moreover, although increasing $V_b$ increases the size of the tunnelling energy window to include higher Landau levels, due to the selection rules for $\theta = 0°$, these do not contribute to the tunnelling current.

Setting non-zero $V_g$, at constant $V_b$ dopes the graphene electrodes, shifting the two chemical potentials together such that the difference between them remains unchanged. At small $V_b$ and zero $V_g$ in Fig. 7.4 (a), clear current is observed. However, as $V_g$ is increased (decreased), the electrodes become hole-doped (electron-doped). As a result, the tunnelling energy window, set by $V_b$, moves away from the positions of the $m = 0$ and $n = 0$ Landau levels and the current decreases. Additionally, $V_b$ and $V_g$ induce an electric field between the graphene layers in BLG which leads to non-zero interlayer asymmetry $u$. This opens a band gap in the electronic spectrum of BLG [23] and hence affects the current characteristics of the device. Within the voltage window shown in panel (a), $u$ is the largest in the top right/bottom left corners of the $(V_b, V_g)$ diagram and reaches a magnitude of $\sim 20$ meV.

Finally, the current diagram as shown in panel (a) of Fig. 7.4 seems to have

inversion antisymmetry with respect to the point $(V_b, V_g) = (0, 0)$, $I(V_b, V_g) = -I(-V_b, -V_g)$. In fact, within the voltage window presented in Fig. 7.4 (a), this antisymmetry is only weakly broken by the energy dependence of the decay coefficient $c(\varepsilon)$ (see also Appendix 7.A) - a feature also observed experimentally [143, 150]. We investigate this symmetry in more detail in panel (e) where we present current plots for changing $V_b$ and constant $V_g$ from -9 V to 9 V in steps of 3 V corresponding to solid/dashed lines marked in (a). We show with solid lines current for negative $V_g$ and $V_b$ and, with dashed lines, current for positive $V_b$ and $V_g$. The same colour is used for curves with the same magnitude of $V_g$ and, for all $V_g$, we have $I(V_g, V_b)$ almost equal to $-I(-V_g, -V_b)$.

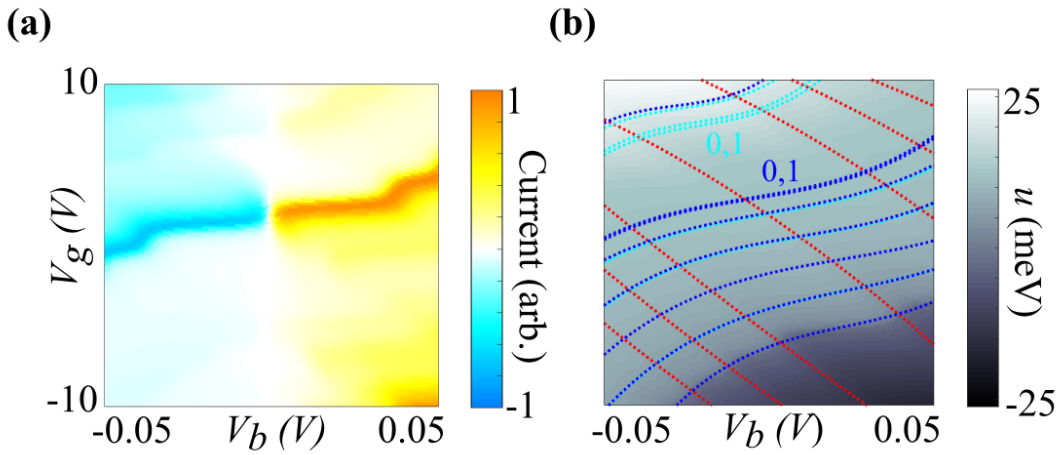


**Figure 7.5:** (Color online) Total tunnelling current at $B = 1$ T as a function of the bias and gate voltages, $V_b$ and $V_g$, for $\theta = 0°$ and $V_t = 0.5$ V is shown in (a). The interlayer asymmetry is plotted as a function of bias and gate voltages in (b). Red lines and labels in (b) indicate the points where $\mu_{\mathrm{MLG}}$ lies at the centre of a MLG Landau level. Blue (cyan) lines and labels in (b) indicate the points where $\mu_{\mathrm{BLG}}$ lies at the centre of a BLG Landau level in the $\boldsymbol{K}_+$ ($\boldsymbol{K}_-$) valley. Part of this figure was published in Physical Review B [2].

In Fig. 7.5 (a), we show the tunnelling current as a function of $V_b$ and $V_g$ for $V_t = 0.5$ V. Non-zero $V_t$ induces interlayer asymmetry, $u$, even for $V_b = V_g = 0$ V while also introducing a shift between the MLG and BLG neutrality points, $\Delta$. The former leads to valley splitting resulting in the separation of the $m = 0, 1$ lines in the two valleys in Fig. 7.5 (b), while the latter leads to energy misalignment of the $m = n = 0$ Landau levels. However, because in BLG the position of the $m = 0$ Landau level depends linearly on $u$ (see Eq. (2.40)), the impact of $V_t$ can be counterbalanced by choosing $V_g$ such that the overall $u$ shifts the $m = 0$ BLG Landau level in the $\boldsymbol{K}_+$ valley back into alignment with the $n = 0$ Landau level in MLG. This restores the finger-like feature in panel (a), visible for some

positive $V_g$.

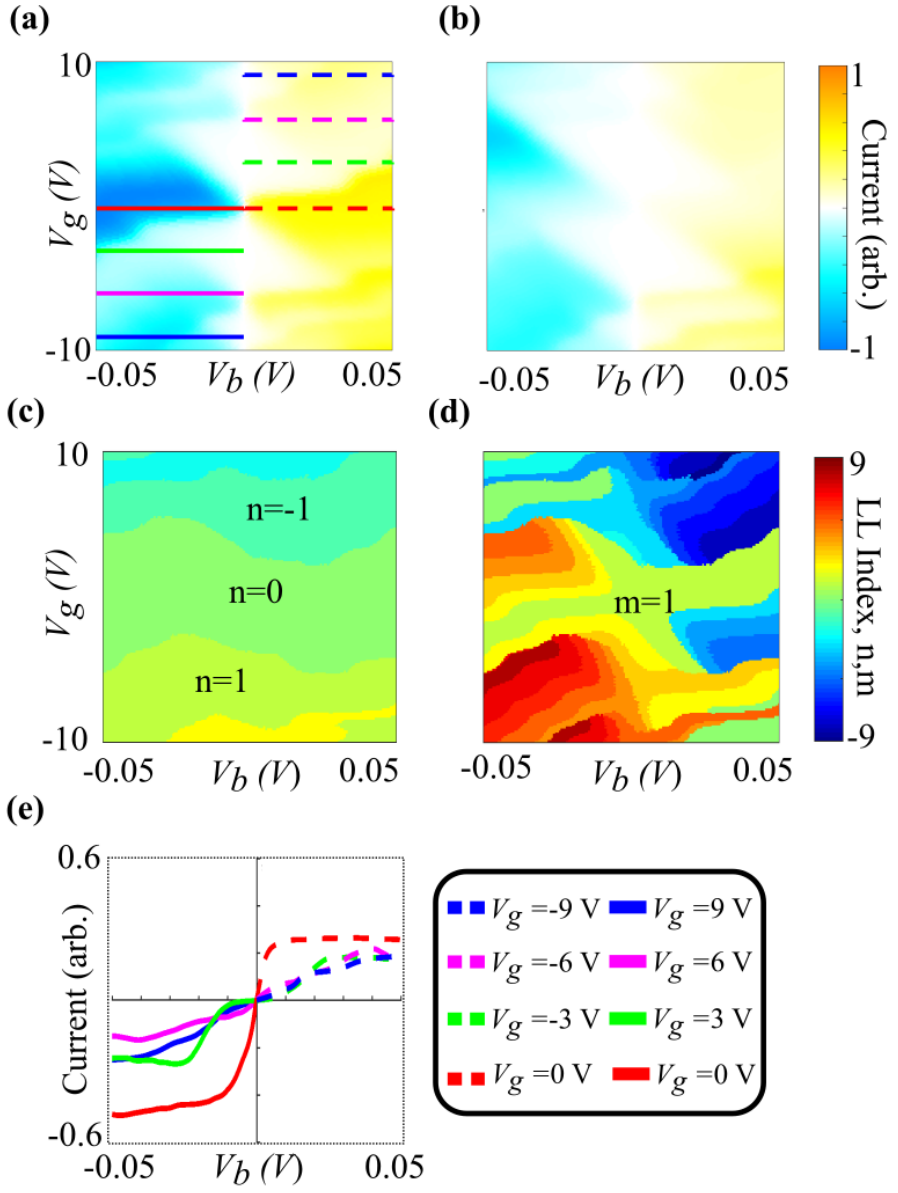


**Figure 7.6:** (Color online) Total tunnelling current at $B = 1$ T as a function of the bias and gate voltages, $V_b$ and $V_g$ for (a) $\theta = 0.25°$ and $V_t = 0$ V (b) $\theta = 0.5°$ and $V_t = 0$ V. The interlayer asymmetry is plotted as a function of bias and gate voltages in (b). Red lines and labels in (b) indicate the points where $\mu_{\mathrm{MLG}}$ lies at the centre of a MLG Landau level. Blue (cyan) lines and labels in (b) indicate the points where $\mu_{\mathrm{BLG}}$ lies at the centre of a BLG Landau level in the $\boldsymbol{K}_+$ ($\boldsymbol{K}_-$) valley. The Landau levels, $n$ and $m$ with dominant contribution to the tunnelling current in (a) are shown in (c) and (d) respectively. Panel (e) shows current curves corresponding to the lines marked in (a), with changing $V_b$ and constant $V_g$ from -9 V to 9 V in steps of 3 V. Part of this figure was published in Physical Review B [2].

In Fig. 7.6 (a) and (b), we show the impact of misalignment $\theta = 0.25°$ and $\theta = 0.5°$, respectively, between the two electrodes on the tunnelling current. For non-zero $\theta$, the oscillator functions $\tilde{\phi}_n$ and $\phi_m$ are no longer orthonormal and transitions between any pair of states are allowed. This can be observed in Fig. 7.6 (c) and (d) where we show, respectively, the $n$ and $m$ with the strongest contribution to the current in (a). Therefore, in panels (a) and (b), the finger-like feature present in Fig. 7.4 and 7.5 becomes increasingly smeared out with increasing $\theta$ and the tunnelling current also decreases as compared to Fig. 7.4 and 7.5. Furthermore, due to the misalignment angle, this finger-like region is predominantly as a result of tunnelling transitions between the $n = 0$ level in MLG and a range of levels in BLG (rather than just $n = 0$ and $m = 0$ as in Fig. 7.4). Additionally, misalignment between the electrodes breaks the approximate inversion antisymmetry of the current diagram in Fig. 7.4. In the presence of $\theta \neq 0°$, each of the four terms of the kind $\int \tilde{\phi}_n \phi_m dA$ appearing in the calculation of the matrix element $M^{s,s'}_{n,m,\xi}(\varepsilon)$ (see also Eqs. (7.6) and (7.7) ) comes with a prefactor that depends on the MLG and BLG band indices $s'$ and $s$ ($s'$ and $C_2$ in particular). Upon inversion from $I(V_g, V_b)$ to $I(-V_g, -V_b)$, the interference between these terms leads to different results depending on whether the initial and final states originate in the conduction or valence band. As a consequence, the approximate inversion antisymmetry about $(V_g, V_b) = (0, 0)$, present in Fig. 7.4 is strongly broken in both Fig. 7.6 (a) and (b). This is demonstrated in more detail in Fig. 7.6 (e), where we show similar current curves as in Fig. 7.4 (e) (changing $V_b$ for constant $V_g$ from -9 V to 9 V in steps of 3 V with the same colour scheme) produced for $\theta = 0.25°$ (the cuts are also indicated in panel (a)). In particular, the magnitude of the current for $V_g = 0$ V is much larger for $V_b < 0$ V than $V_b > 0$ V.

### 7.3.2 Valley polarisation at $B = 1$ T

As the Landau level wave functions of BLG are not distributed equally between its two constituent graphene layers and this distribution is reversed between the valleys, tunnelling in the device shown in Fig. 7.1 can be used to produce unequal electron occupations in the MLG drain electrode. Such an effect can be characterised by the valley polarisation, $P$, of the tunnelling current, introduced in Eq. (7.10), which we plot in Fig. 7.7 as a function of the gate voltages $V_g$ and $V_b$ for $B = 1$ T. Panels (a)-(d) in this figure correspond to the same parameters for which we presented total tunnelling current (Fig. 7.4 (a), Fig. 7.5 (a), Fig. 7.6 (a) and Fig. 7.6 (b) respectively).

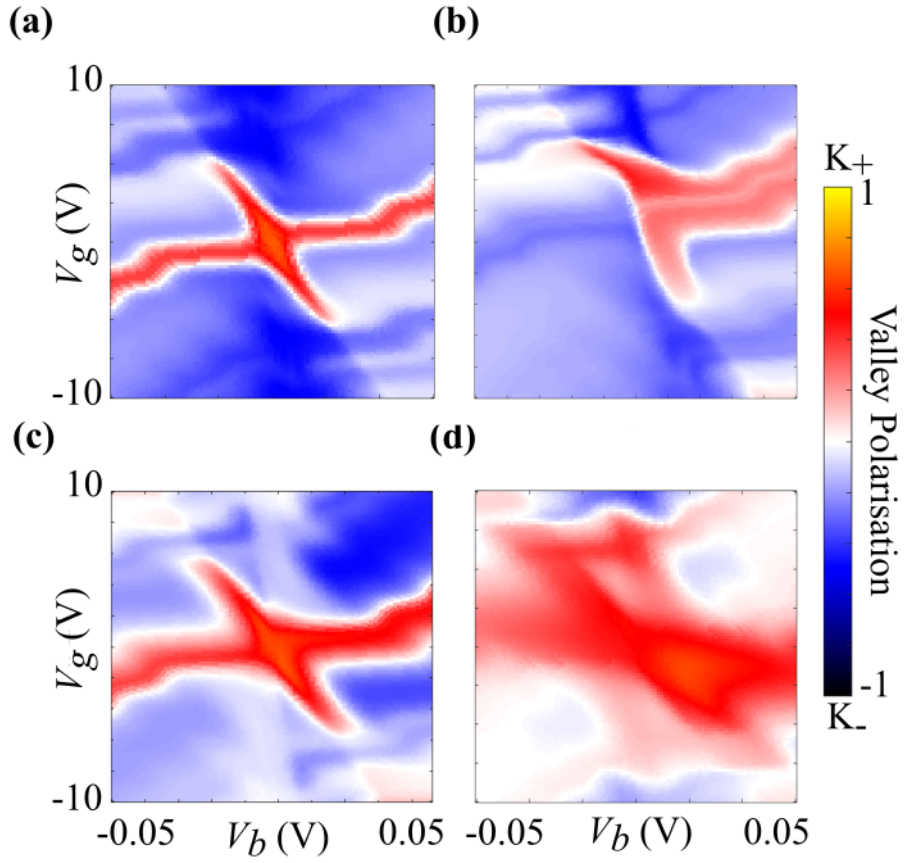


**Figure 7.7:** (Color online) Valley polarisation of the tunnellling current at $B = 1$ T, as a function of the bias and gate voltages $V_b$ and $V_g$. Each of the panels (a)-(d) corresponds to a total current plot shown in the previous section: (a) $\theta = 0°$ and $V_t = 0$ V (b) $\theta = 0°$ and $V_t = 0.5$ V, (c) $\theta = 0.25°$ and $V_t = 0$ V and (d) $\theta = 0.5°$ and $V_t = 0$ V. Positive (negative) polarisation indicates current favouring the $\boldsymbol{K}_+$ ($\boldsymbol{K}_-$) valley. Part of this figure was published in Physical Review B [2].

In panel (a), we show the case of $\theta = 0°$ and $V_t = 0$ V. The polarisation diagram has inversion symmetry with respect to $(V_b, V_g) = (0, 0)$. A bright red cross-like feature corresponds to $P \sim 50\%$ with a region of $P \sim 80\%$ in the centre of the diagram. This high valley polarisation is due to the tunnelling between the $m = 0$ BLG and $n = 0$ MLG Landau levels. In the BLG $\boldsymbol{K}_+$ valley, electrons in the $m = 0$ state occupy exclusively the layer closer to the barrier, whereas in the $\boldsymbol{K}_-$ valley all of them sit on the layer further from the barrier. Consequently, the current in the $\boldsymbol{K}_+$ valley is significantly larger than in the $\boldsymbol{K}_-$ valley.

As $V_g$ is increased, the $m = 0$ and $n = 0$ Landau levels move out of alignment and the dominant source of tunnelling current becomes the $m = 2$ to $n = 0$ transition. From Eq. (2.41), the BLG $m = 2$ wave function is $\psi^{\xi}_{2,s} \propto (C_1\phi_2, C_2\phi_0)^T$, where $C_1$ and $C_2$ are complex numbers, and the first and second components of

$\psi^{\xi}_{2,s}$ are located respectively on layer 1 (layer 2) and layer 2 (layer 1) in valley $\boldsymbol{K}_+$ ($\boldsymbol{K}_-$). For the MLG $n = 0$, $\tilde{\psi} = (\tilde{\phi}_0, 0)$, so that for $\theta = 0°$, tunnelling in $\boldsymbol{K}_+$ is only possible for BLG electrons from layer 2, further from the barrier, while in $\boldsymbol{K}_-$ it is the electrons from layer 1 that can tunnel into MLG. As a result, the overall current has negative ($\boldsymbol{K}_-$) polarization as shown by dark blue regions above and below the central red cross in Fig.7.7 (a). Similar arguments can be used to explain other regions of the polarisation diagram.

For non-zero top gate voltage, as shown in Fig. 7.7 (b) for $V_t = 0.5$ V, the polarisation map is modified as a result of the shift between the neutrality points, $\Delta$, as well as non-zero interlayer asymmetry, $u$, at $(V_b, V_g)$=(0,0). The latter lifts the valley degeneracy of the BLG $m = 0$ Landau level. Alignment of the $\boldsymbol{K}_+$ BLG $m = 0$ and MLG $n = 0$ states, responsible for the red cross-like feature in (a), now requires compensating with positive gate voltage. However, for negative $V_b$ it is not possible to both align these two states and position the BLG and MLG chemical potentials such that the aligned states contribute to the current. As a result, the left arm of the red cross disappears and the $m = 2$ to $n = 0$ transitions lead to negative polarisation in this region.

In Fig. 7.7 (c) and (d), we show valley polarisation as a function of $V_b$ and $V_g$ for increasing misalignment between the electrodes, $\theta = 0.25°$ and $\theta = 0.5°$ corresponding to total current plots in Fig. 7.6 (a) and (b). Similar to the current features, when the graphene electrodes are misaligned, individual polarisation features become smeared out and the variation of polarisation throughout the $(V_b, V_g)$-space becomes more gradual. The oscillator states $\phi_m$ and $\tilde{\phi}_n$ are not orthonormal for $\theta \neq 0°$ so that many different transitions contribute to the overall polarisation for given $(V_b, V_g)$. Importantly, interference of electronic states tunnelling between any of the BLG layers and any of the MLG sublattices which leads to different outcomes for conduction band-conduction band and valence band-valence band transitions, strongly breaks the inversion symmetry of polarisation present in Fig. 7.7 (a) for $\theta = 0°$. This symmetry breaking grows with increasing $\theta$.

### 7.3.3 Tunnelling at $B = 4$ T

The Landau level structures in BLG and MLG depend on the strength of the magnetic field differently, hence the tunnelling current and polarisation features in the $(V_b, V_g)$ diagrams depend on $B$. For this reason, to contrast our results for $B = 1$ T presented in Fig. 7.4 - 7.7 with the case of stronger magnetic field, in Fig. 7.8 we show the tunnelling current and its valley polarisation for $B = 4$

T, $\theta = 0°$ and $V_t = 0$ V. Due to the increased electron density per Landau level at $B = 4$ T, it is necessary to increase the voltage range in order to compare features arising from similar electronic tunnelling transitions. In a similar way to the $B = 1$ T case, a finger-like structure can be observed in Fig. 7.8 (a). In fact, it is more pronounced because the separation between the $m = n = 0$ Landau levels and the rest of the electronic spectra in the corresponding materials is increased. Consequently, the central cross-like region of $\boldsymbol{K}_+$-polarised current is also sharper, including polarisation of $P \sim 90\%$ in the vicinity of $(V_b, V_g) = (0, 0)$. The maximum $\boldsymbol{K}_-$ polarisation in the blue region dominated by $m = 2$ to $n = 0$ tunnelling is also increased.

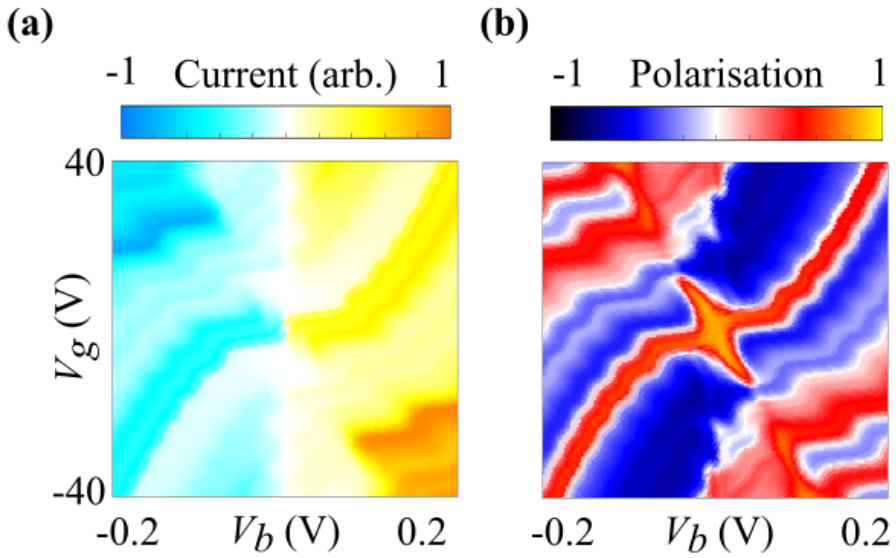


**Figure 7.8:** (Color online) Total tunnelling current (a) and valley polarisation (b) as a function of the bias and gate voltages $V_b$ and $V_g$ for magnetic field $B = 4$ T, $\theta = 0°$ and $V_t = 0$ V. The maximum polarisation observed is as much as 90% in favour of the $\boldsymbol{K}_+$ valley. Part of this figure was published in Physical Review B [2].

## 7.4 Tunnelling with strong momentum scattering

In the presence of a poor interface between the electrodes and the hBN barrier, the scattering length-scale becomes very small such that the momentum resolution of the tunnelling electron becomes lost. In this limit, the momentum-nature of the initial and final state has no effect on the magnitude and valley polari-

sation of the current across the device. Instead, the tunnelling current depends only on the density of states of the source and drain electrode. As a consequence, we expect the valley polarisation of the tunnelling current to arise purely due to differences in valley occupations of the two BLG layers. We model this regime by setting each harmonic oscillator integral, $\int \tilde{\phi}_n \phi_m dA$, equal to 1 for all the transitions independently of their initial and final states[5] and present our results for $\theta = 0^\circ$ and $V_t = 0$ V in Fig. 7.9.

In panels (a) and (b), we show the tunnelling current for $B = 1$ T and $B = 4$ T, respectively. Because, in the limit of relaxed momentum conservation, all of the transitions are now allowed, the graphs look similar to that in Fig. 7.7 (b), corresponding to $\theta = 0.5^\circ$. In (b), the increased magnitude of the magnetic field leads to larger spacing between the Landau levels so that, as compared to (a), a larger voltage window is necessary to capture features due to transitions between the same pair of Landau levels.

In Fig. 7.9 (c) and (d), we present valley polarisation of the currents shown in Fig. 7.9 (a) and (b), respectively. The relaxation of the selection rules discussed in the previous section results in polarisation maps which are heavily weighted in favour of the $\boldsymbol{K}_+$ valley. In particular, the maximum valley polarisation occurs at low voltages, where the participating Landau levels are those with low index (in particular $m = 0$ and $m = 1$). This is because, for the $m = 0$ and $m = 1$ BLG Landau levels, the valley and layer degrees of freedom are coupled. Furthermore, the interlayer asymmetry, $u$, generates a layer population difference in the $m \geq 2$ Landau levels in BLG, which is opposite in the two valleys. This induced interlayer asymmetry is responsible for small regions of minor $\boldsymbol{K}_-$ polarisation which occur at higher voltages. These two principles are responsible for all polarisation features observed in Fig. 7.9 (c) and (d).

The relative misalignment of the graphene electrodes has no effect on the tunnelling probability in this limit. Similarly to the case of momentum-conserving tunnelling between misaligned electrodes, where $\theta \neq 0^\circ$, the lack of restrictions on allowed transitions leads to chiral interference. This interference results in the asymmetry in inversion about the origin that is observed in Fig. 7.9. We expect momentum non-conserving tunnelling to be the dominant mechanism when the misalignment angle between the graphene electrodes is large. This is because, while increasing misalignment angle decreases the magnitude of the momentum-conserving current, it should have no effect on the transitions involving scattering.

[5]This limit is equivalent to setting the scattering length much smaller than the magnetic length ($\sigma \ll \lambda_B$) in the theoretical model employed in Ref. [144]

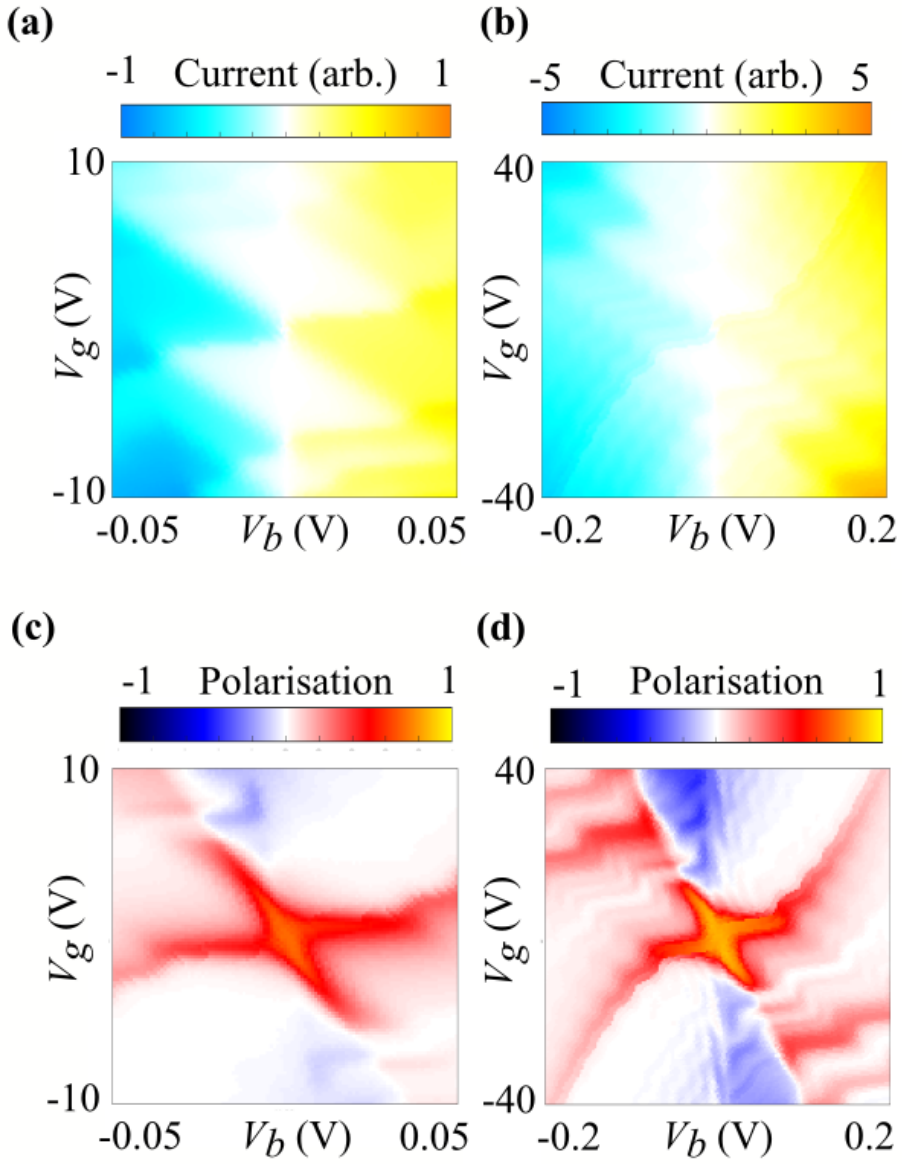


**Figure 7.9:** (Color online) Electron transport through the proposed device in the absence of momentum conservation and as a function of the bias and gate voltages $V_b$ and $V_g$ with $V_t = 0$. Panels (a) and (b) show the total tunnelling current for $\theta$=0° and (a) $B = 1$ T, (b) $B = 4$ T. Panels (c) and (d) present valley polarisation of the current shown in (a) and (b), respectively. Part of this figure was published in Physical Review B [2].

## 7.5 Summary

We have explored the tunnelling characteristics of a vertical field effect transistor comprising monolayer and bilayer graphene electrodes, in the presence of a perpendicular magnetic field. The coupled layer and valley polarisation in the Landau levels of bilayer graphene gives rise to a valley-polarised tunnelling

current through the device resulting in unequal valley populations in monolayer graphene. Our result is due to the difference in effective tunnelling barrier widths for electrons in the two layers of the BLG electrode. As such, valley polarisation should persist in the presence of small local variations of the tunnelling rates (and hence effective tunnelling decay lengths). Importantly, this valley polarisation can be tuned solely by electrostatic means without the need to reverse the direction of the magnetic field. Our modelling suggests that $P \sim \pm 80\%$ is possible in high quality devices in homogeneous fields of $B = 1$ T. Fields of such magnitude could be in principle generated by placing ferromagnets on top of the device [178]. While the homogeneity of the field distribution across the device would then depend on the size of the ferromagnet, thickness of the tunnelling junction and distance between the two, valley polarisation might still be possible in such a setup. The relatively low magnetic fields required suggest possible valleytronic applications.

In both the momentum-conserving and non-conserving regimes, the most persistent feature in valley polarisation plots is the cross-like region of $\boldsymbol{K}_+$-polarised current around $(V_g, V_b) = (0, 0)$. In the same voltage region, the total tunnelling current forms a finger-like pattern. Both originate in tunnelling current from $m = 0$ ($m = 0, 1$ in the absence of momentum conservation) to $n = 0$, so that observing the finger-like features in the current should indicate a region of considerable valley polarisation. In order to detect the valley polarisation produced using the proposed device directly, two stacks could be connected in series: the first one to produce unequal valley populations and the second to act as a detector. Alternatively, the produced valley polarisation can be measured using optical means [179].

## 7.A Changing the decay constant of graphene

In the main text, we take the decay constant $c'(\varepsilon)$ characterising tunnelling through monolayer graphene to be equivalent to the decay constant $c(\varepsilon)$ corresponding to tunnelling through hBN. Here we discuss the effect of changing the decay constant $c'(\varepsilon)$, on our results.

In our work, we use the expression in Eq. (A1) to obtain the decay constant $c'(\varepsilon) = c(\varepsilon)$ for the tunnelling of BLG electrons from the layer further from the barrier across the graphene layer closer to the barrier. While both the barrier height and the effective mass would be different for graphene as compared to hBN our main conclusions are quite insensitive to the numerical values of $c'(\varepsilon)$

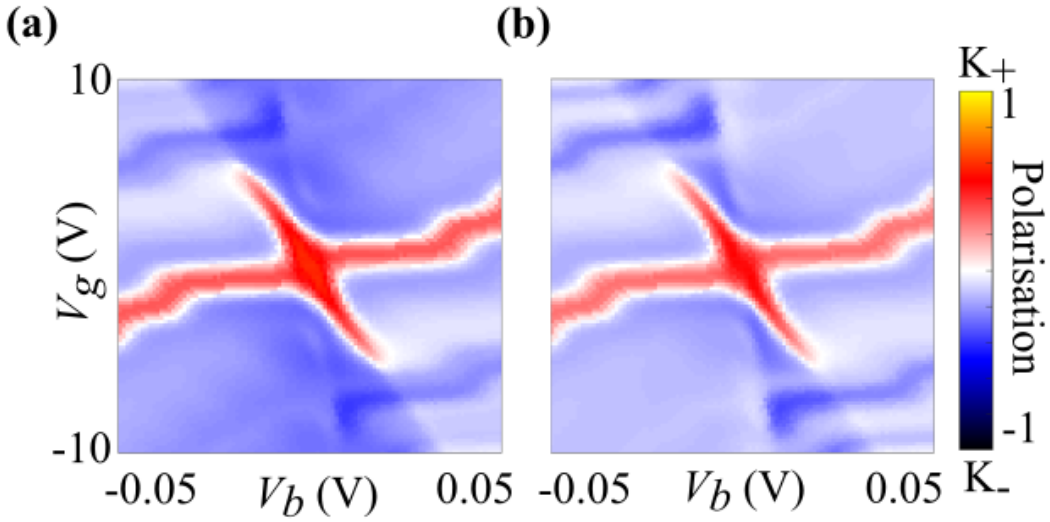


**Figure 7.10:** (Color online) Valley polarisation for momentum-conserving tunnelling between perfectly-aligned electrodes ($\theta = 0°$) and for $B = 1$ T as a function of $V_b$ and $V_g$ with $V_t = 0$ V. In contrast to the polarisation shown in Fig. 7.7 (a), the plots here are obtained using the decay constant decreased by a factor (a) $\frac{1}{\sqrt{2}}$ and (b) $\frac{1}{2}$ (compared to in the main text). This figure was published in Physical Review B [2].

and $c(\varepsilon)$. In fact, the latter impacts both the electrons tunnelling from the top and bottom BLG layers in the same way and hence leads to an identical numerical coefficient for all tunnelling processes for given applied voltages. The physics we describe arises primarily due to the additional exponential factor, $\exp(-c'(\varepsilon)d_0)$, in tunnelling from the bottom layer as compared to the top one.

In Fig. 7.10, we demonstrate the valley polarisation at $B = 1$ T and $\theta = 0°$ for effective graphene decay constant, $c'(\varepsilon)$, scaled by a factor of (a) $\frac{1}{\sqrt{2}}$ and (b) $\frac{1}{2}$ as compared to the hBN value provided by Eq. (A1). While the asymmetry between $P(V_b, V_g)$ and $P(-V_b, -V_g)$ increases slightly for smaller decay constant, qualitative features of the valley polarisation graphs remain the same. Also, the maximum valley polarisations are still significant, 58% and 48% respectively, compared to 80% in Fig. 7.7 (a). Increasing $c'(\varepsilon)$ (making graphene more insulating) increases the valley polarisation of the tunnelling current.

# Chapter 8

# Summary

In this thesis, we have explored the theoretical electronic properties of stacked two-dimensional atomic crystals. In particular, we demonstrate that the electronic properties of the resulting van der Waals heterostructures differ notably from the constituent layers. We pay particular attention to the relative alignment of the constituent layers, where the twist angle between their crystallographic axis becomes crucial in determining the resulting electronic behaviour.

In Chapter 2, we described the basic electronic properties of monolayer and bilayer graphene using the familiar tight-binding descriptions. Furthermore, we derived expressions for the resulting Landau level spectra in these materials as a result of applying a strong magnetic field perpendicular to the layer plane. We shifted our attention to moiré superlattice structures incorporating graphene in Chapter 3. We introduced the basic geometry of these moiré superlattices as well as the concept of commensuration before deriving theoretical models for twisted bilayer graphene, graphene on hBN and graphene on $\alpha - In_2Te_2$. We then considered the effect of a magnetic field on the moiré superlattice in graphene on hBN and demonstrated theoretically that the Landau level spectrum undergoes significant changes forming Hofstadter's butterfly.

We introduced electronic Raman scattering in Chapter 4, where we showed that it can be used to characterise the misalignment angle in twisted bilayer graphene. Furthermore, the sensitivity of the dominant Raman peak to the twist angle suggested that electronic Raman scattering can be used to accurately determine whether the misalignment in a bilayer sample is close to the magic angle. We observed that the spectral profile and position of the peaks allowed the dominant excitation to be described. Importantly, by comparison to monolayer graphene (on which experimental electronic Raman has been carried out [102]), we demonstrated that the Raman peaks observed in the electronic Raman spectrum of twisted bilayer graphene should be measureable at low angles, where these strong peaks occur at Raman wavelengths far away from the large phonon modes.

In Chapter 5, we proposed a unique parameter set which self-consistently describes the interlayer coupling between twisted graphene layers. In particular, we proposed that twisted trilayer graphene is the smallest system where parts can be simultaneously described using the real space tight-binding model and the reciprocal space continuum model, hence allowing the self-consistency of our model to be accurately probed. By modelling angle-resolved photoemission spectroscopy, we can verify this description by comparison to experimental data.

In Chapter 6, we introduced the concept of van der Waals tunnelling transistors comprised of graphene electrodes separated by a hBN tunnelling barrier. By placing either another misaligned graphene layer, or another type of almost

commensurate two-dimensional atomic crystal such as hBN or $\alpha - In_2Te_2$, in the source/drain electrode, the electronic band structures become strongly modified leading to non-linear tunnelling current characteristics. In particular, we demonstrated that this leads to negative differential resistance in the absence of momentum conserving tunnelling. In the case of electrodes comprised of graphene on $\alpha - In_2Te_2$, a peak-to-valley ratio of the order of $\sim 10$ was obtained suggesting practical applications.

Finally, in Chapter 7, we demonstrated that in a van der Waals tunnelling transistor comprising a bilayer graphene source electrode and monolayer drain electrode, all in the presence of a perpendicular magnetic field, a strongly valley polarised current can be generated as a function of applied voltages. The polarisation and current properties of the device depend strongly on the twist angle between the source and drain electrode as well as the magnetic field strength. In this case, the interplay between the tunnelling matrix element and the quantised density of states, as well as the coupled layer and valley degrees of freedom lead to this valley polarisation. Furthermore, we explained that these coupled layer and valley degrees of freedom lead to valley polarisation even in the absence of momentum conservation. Valley polarisation as large as 80% was found at $B = 1$ T which suggests that the proposed setup could be used as a valleytronic device.

## 8.1 Future work

In this section, we will describe possible avenues for future work related to the content described in this thesis. We demonstrated that electronic Raman scattering could be used as an effective probe of the twist angle in Chapter 4, however improvements to this model could be made. Firstly at low twist angles, including around the magic angle, in an effort to minimise its energy, the crystal structure of twisted bilayer becomes strained. This strain would need to be included to improve the accuracy of our model. Second, we could, although unlikely to be important, include higher order processes in the electronic Raman calculation, including the contact interaction. Extending this theory to twisted trilayer or including in-plane magnetic fields could be interesting while including a strong out-of plane magnetic field would lead to Landau quantisation and Hofstadter's butterfly, a system in which electronic Raman scattering has not been calculated. In this case, we believe selection rules between the fractal magnetic minibands could lead to a unique electronic Raman spectrum

In Chapter 5 we focused on using the ARPES spectra of twisted trilayer

graphene to determine the interlayer coupling in twisted graphene layers. Ideally, in order to strengthen the arguments of this work, we should compare the theoretical and experimental ARPES spectra for a wider range of angles. Moreover, a few natural continuations of this work exist. First, we focused primarily on twisted trilayers of the form $(\theta - 0 - 0)$ and a natural next step would be to look at the ARPES spectra of trilayer with two or more relative rotations (between each pair of layers). Second, it would be interesting to look at special misalignment angles in twisted bilayer graphene, in particular 30°. At this twist angle, it has been demonstrated [77], that Dirac cone replicas in the ARPES spectra are significantly more intense than at other angles. This arises as a result of the multiple scattering paths projecting onto the same point in reciprocal space. The authors of this work [77], use a parameter set, $\tilde{t}(\boldsymbol{q}, d_0)$ with a much sharper drop off than used in this thesis, which appears to be in contradiction with the ARPES experiment. Since the ARPES intensity of Dirac cone replicas is dependent on the interlayer coupling at large $\boldsymbol{q}$, we suggest that our more slowly diminishing $\tilde{t}(\boldsymbol{q}, d_0)$ could explain this discrepancy. We could also try extending the continuum model to try and capture more terms in the electronic Hamiltonian of twisted bilayer graphene in the zero-angle limit, in particular reproducing terms corresponding to $\gamma_3$ and $\gamma_4$ in Chapter 2.

The results presented in Chapter 6 are very general with many degrees of freedom in the construction of the van der Waals tunnelling transistor. By changing the materials in the source and drain electrodes, as well as changing the twist angle, it may be possible to generate an NDR even larger than those discussed in this thesis such as combinations of magic-angle twisted bilayer graphene and graphene on other almost-commensurate substrates.

The valley polarisation generated by the van der Waals tunnelling transistor proposed in Chapter 7 could have practical applications as a valleytronic device, however the difficulty is measuring this valley polarisation. Future work could include modelling a way to probe this valley polarisation by either placing two devices in series, or by optical means. The application of a large perpendicular magnetic field could lead to spin splitting via the Zeeman effect. Furthermore, as the magnetic field increases, the magnetic length decreases, confining the electrons and leading to stronger electron-electron interactions. These two effects can lift the degeneracy of the Landau levels, possibly altering the valley polarisation and current characteristics.

This thesis has focused on graphene-based heterostructures, however other materials such as transition metal dichalcogenides could be used in its place, for example $MoS_2$. The continuum model described in Chapter 3 can be extended

to twisted bilayers/trilayers of TMDs and it would be interesting to see whether phenomena such as Van Hove singularities and flat bands are observed. Furthermore, valley polarisation is of particular interest in TMD materials, where circularly polarised light can be utilised to generate/probe valley polarisation [163]. As such, probing the valley polarisation using a setup similar to that in Chapter 7 could be used in tandem with optical methods.

# Chapter 9

# Bibliography

[1] Leech, D. J., Thompson, J. J. P., and Mucha-Kruczyński, M. *Physical Review Applied* **10**(3), 034014 (2018).

[2] Thompson, J. J. P., Leech, D. J., and Mucha-Kruczyński, M. *Physical Review B* **99**(8), 085420 (2019).

[3] Chalmers, A. *The Scientist's Atom and the Philosopher's Stone: How Science Succeeded and Philosophy Failed to Gain Knowledge of Atoms (Boston Studies in the Philosophy and History of Science Book 279).* Springer, (2009).

[4] Novoselov, K. S., Geim, A. K., Morozov, S. V., Jiang, D., Zhang, Y., Dubonos, S. V., Grigorieva, I. V., and Firsov, A. A. *Science* **306**, 666–669 (2004).

[5] Mermin, N. D. *Phys. Rev.* **176**, 250–254 (1968).

[6] Novoselov, K. S., Geim, A. K., Morozov, S. V., Jiang, D., Katsnelson, M. I., Grigorieva, I. V., Dubonos, S. V., and Firsov, A. A. *Nature* **438**, 197 (2005).

[7] Katsnelson, M. I., Novoselov, K. S., and Geim, A. K. *Nat. Phys.* **2**, 620 (2006).

[8] Morozov, S. V., Novoselov, K. S., Katsnelson, M. I., Schedin, F., Ponomarenko, L. A., Jiang, D., and Geim, A. K. *Phys. Rev. Lett.* **97**, 016801 (2006).

[9] McCann, E., Kechedzhi, K., Fal'ko, V. I., Suzuura, H., Ando, T., and Altshuler, B. L. *Phys. Rev. Lett.* **97**, 146805 (2006).

[10] Nair, R. R., Blake, P., Grigorenko, A. N., Novoselov, K. S., Booth, T. J., Stauber, T., Peres, N. M. R., and Geim, A. K. *Science* **320**, 1308 (2008).

[11] Kuzmenko, A. B., Crassee, I., van der Marel, D., Blake, P., and Novoselov, K. S. *Phys. Rev. B* **80**, 165406 (2009).

[12] Lee, C., Wei, X., Kysar, J. W., and Hone, J. *Science* **321**, 385 (2008).

[13] Mattevi, C., Kim, H., and Chhowalla, M. *Journal of Materials Chemistry* **21**, 3324–3334 (2011).

[14] Strupinski, W., Grodecki, K., Wysmolek, A., Stepniewski, R., Szkopek, T., Gaskell, P. E., Grüneis, A., Haberer, D., Bozek, R., Krupka, J., and Baranowski, J. M. *Nano Lett.* **11**, 1786–1791 (2011).

[15] Park, J., Mitchel, W. C., Grazulis, L., Smith, H. E., Eyink, K. G., Boeckl, J. J., Tomich, D. H., Pacley, S. D., and Hoelscher, J. E. *Advanced Materials* **22**, 4140–4145 (2010).

[16] Ribeiro, R. M. and Peres, N. M. R. *Phys. Rev. B* **83**, 235312 (2011).

[17] Dean, C. R., Young, A. F., Meric, I., Lee, C., Wang, L., Sorgenfrei, S., Watanabe, K., Taniguchi, T., Kim, P., Shepard, K. L., and Hone, J. *Nat. Nano.* **5**, 722 (2010).

[18] Zhang, Y., Chang, T.-R., Zhou, B., Cui, Y.-T., Yan, H., Liu, Z., Schmitt, F., Lee, J., Moore, R., Chen, Y., et al. *Nat. Nano.* **9**, 111–115 (2014).

[19] Nakata, Y., Yoshizawa, T., Sugawara, K., Umemoto, Y., Takahashi, T., and Sato, T. *ACS Appl. Nano Mater.* **1**, 1456–1460 (2018).

[20] Sugawara, K., Nakata, Y., Shimizu, R., Han, P., Hitosugi, T., Sato, T., and Takahashi, T. *ACS nano* **10**, 1341–1345 (2015).

[21] Miller, D. C., Mahanti, S. D., and Duxbury, P. M. *Phys. Rev. B* **97**, 045133 (2018).

[22] Shi, W., Ye, J., Zhang, Y., Suzuki, R., Yoshida, M., Miyazaki, J., Inoue, N., Saito, Y., and Iwasa, Y. *Scientific reports* **5**, 12534 (2015).

[23] McCann, E. and Fal'ko, V. I. *Phys. Rev. Lett.* **96**, 086805 (2006).

[24] Schwierz, F. *Nat. Nano.* **5**, 487 (2010).

[25] McCann, E. *Phys. Rev. B* **74**, 161403 (2006).

[26] Geim, A. K. and Grigorieva, I. V. *Nature* **499**, 419 (2013).

[27] Novoselov, K. S., Mishchenko, A., Carvalho, A., and Castro Neto, A. H. *Science* **353** (2016).

[28] Li, G., Luican, A., Lopes dos Santos, J. M. B., Castro Neto, A. H., Reina, A., Kong, J., and Andrei, E. Y. *Nat. Phys.* **6**, 109 (2009).

[29] Cao, Y., Fatemi, V., Demir, A., Fang, S., Tomarken, S. L., Luo, J. Y., Sanchez-Yamagishi, J. D., Watanabe, K., Taniguchi, T., Kaxiras, E., Ashoori, R. C., and Jarillo-Herrero, P. *Nature* **556**, 80 (2018).

[30] Cao, Y., Fatemi, V., Fang, S., Watanabe, K., Taniguchi, T., Kaxiras, E., and Jarillo-Herrero, P. *Nature* **556**, 43 (2018).

[31] Woods, C. R., Britnell, L., Eckmann, A., Ma, R. S., Lu, J. C., Guo, H. M., Lin, X., Yu, G. L., Cao, Y., Gorbachev, R. . V., Kretinin, A. V., Park, J., Ponomarenko, L. A., Katsnelson, M. I., Gornostyrev, Y. N., Watanabe, K., Taniguchi, T., Casiraghi, C., Gao, H.-J., Geim, A. K., and Novoselov, K. . S. *Nat. Phys.* **10**, 451 (2014).

[32] Wang, E., Lu, X., Ding, S., Yao, W., Yan, M., Wan, G., Deng, K., Wang, S., Chen, G., Ma, L., Jung, J., Fedorov, A. V., Zhang, Y., Zhang, G., and Zhou, S. *Nat. Phys.* **12**, 1111 (2016).

[33] Jung, J., Laksono, E., DaSilva, A. M., MacDonald, A. H., Mucha-Kruczyński, M., and Adam, S. *Phys. Rev. B* **96**, 085442 (2017).

[34] Wallbank, J. R., Mucha-Kruczyński, M., and Fal'ko, V. I. *Phys. Rev. B* **88**, 155415 (2013).

[35] Leech, D. J. and Mucha-Kruczyński, M. *Phys. Rev. B* **94**, 165437 (2016).

[36] Sevik, C., Wallbank, J. R., Gülseren, O., Peeters, F. M., and Çakir, D. *2D Materials* **4**, 035025 (2017).

[37] Dean, C. R., Wang, L., Maher, P., Forsythe, C., Ghahari, F., Gao, Y., Katoch, J., Ishigami, M., Moon, P., Koshino, M., Taniguchi, T., Watanabe, K., Shepard, K. L., Hone, J., and Kim, P. *Nature* **497**, 598 (2013).

[38] Ponomarenko, L. A., Gorbachev, R. V., Yu, G. L., Elias, D. C., Jalil, R., Patel, A. A., Mishchenko, A., Mayorov, A. S., Woods, C. R., Wallbank, J. R., Mucha-Kruczynski, M., Piot, B. A., Potemski, M., Grigorieva, I. V.,

Novoselov, K. S., Guinea, F., Fal'ko, V. I., and Geim, A. K. *Nature* **497**, 594 (2013).

[39] Bistritzer, R. and MacDonald, A. *Phys. Rev. B* **84**, 035440 (2011).

[40] Krishna Kumar, R., Chen, X., Auton, G. H., Mishchenko, A., Bandurin, D. A., Morozov, S. V., Cao, Y., Khestanova, E., Ben Shalom, M., Kretinin, A. V., Novoselov, K. S., Eaves, L., Grigorieva, I. V., Ponomarenko, L. A., Fal'ko, V. I., and Geim, A. K. *Science* **357**, 181 (2017).

[41] Wallace, P. R. *Phys. Rev.* **71**, 622–634 (1947).

[42] Saito, R., Dresselhaus, G., and Dresselhaus, M. S. *Physical Properties of Carbon Nanotubes*. PUBLISHED BY IMPERIAL COLLEGE PRESS AND DISTRIBUTED BY WORLD SCIENTIFIC PUBLISHING CO., (1998).

[43] Novoselov, K. S., Morozov, S. V., Mohinddin, T. M. G., Ponomarenko, L. A., Elias, D. C., Yang, R., Barbolina, I. I., Blake, P., Booth, T. J., Jiang, D., Giesbers, J., Hill, E. W., and Geim, A. K. *physica status solidi (b)* **244**, 4106–4111 (2007).

[44] Castro Neto, A. H., Guinea, F., Peres, N. M. R., Novoselov, K. S., and Geim, A. K. *Rev. Mod. Phys.* **81**, 109–162 (2009).

[45] Slonczewski, J. C. and Weiss, P. R. *Phys. Rev.* **109**, 272–279 (1958).

[46] Charlier, J.-C., Michenaud, J.-P., Gonze, X., and Vigneron, J.-P. *Phys. Rev. B* **44**, 13237–13249 (1991).

[47] McCann, E. *Electronic Properties of Monolayer and Bilayer Graphene*, 237–275. Springer Berlin Heidelberg, Berlin, Heidelberg (2012).

[48] Reich, S., Maultzsch, J., Thomsen, C., and Ordejón, P. *Phys. Rev. B* **66**, 035412 (2002).

[49] Novoselov, K. S., McCann, E., Morozov, S. V., Fal'ko, V. I., Katsnelson, M. I., Zeitler, U., Jiang, D., Schedin, F., and Geim, A. K. *Nat. Phys.* **2**, 177 (2006).

[50] McCann, E. and Koshino, M. *Reports on Progress in Physics* **76**, 056503 (2013).

[51] Rozhkov, A. V., Sboychakov, A. O., Rakhmanov, A. L., and Nori, F. *Physics Reports* **648**, 1–104 (2016).

[52] Mucha-Kruczynski, M. *Theory of Bilayer Graphene Spectroscopy.* Springer Berlin Heidelberg, Berlin, Heidelberg, (2013).

[53] Hofstadter, D. R. *Phys. Rev. B* **14**, 2239–2249 (1976).

[54] Yankowitz, M., Xue, J., Cormode, D., Sanchez-Yamagishi, J., Watanabe, K., Taniguchi, T., Jarillo-Herrero, P., Jacquod, P., and Leroy, B. *Nat. Phys.* **8**, 382–386 (2012).

[55] Xue, J., Sanchez-Yamagishi, J., Bulmash, D., Jacquod, P., Deshpande, A., Watanabe, K., Taniguchi, T., Jarillo-Herrero, P., and LeRoy, B. J. *Nat. Mater.* **10**, 282 (2011).

[56] Decker, R., Wang, Y., Brar, V. W., Regan, W., Tsai, H.-Z., Wu, Q., Gannett, W., Zettl, A., and Crommie, M. F. *Nano Lett.* **11**, 2291–2295 (2011).

[57] Wallbank, J. R., Patel, A. A., Mucha-Kruczyński, M., Geim, A. K., and Fal'ko, V. I. *Phys. Rev. B* **87**, 245408 (2013).

[58] Brihuega, I., Mallet, P., González-Herrero, H., Trambly de Laissardière, G., Ugeda, M. M., Magaud, L., Gómez-Rodríguez, J. M., Ynduráin, F., and Veuillen, J.-Y. *Phys. Rev. Lett.* **109**, 196802 (2012).

[59] Ohta, T., Robinson, J. T., Feibelman, P. J., Bostwick, A., Rotenberg, E., and Beechem, T. E. *Phys. Rev. Lett.* **109**, 186807 (2012).

[60] Yan, W., Liu, M., Dou, R.-F., Meng, L., Feng, L., Chu, Z.-D., Zhang, Y., Liu, Z., Nie, J.-C., and He, L. *Phys. Rev. Lett.* **109**, 126801 (2012).

[61] Kim, K., Coh, S., Tan, L. Z., Regan, W., Yuk, J. M., Chatterjee, E., Crommie, M. F., Cohen, M. L., Louie, S. G., and Zettl, A. *Phys. Rev. Lett.* **108**, 246103 (2012).

[62] Robinson, J. T., Schmucker, S. W., Diaconescu, C. B., Long, J. P., Culbertson, J. C., Ohta, T., Friedman, A. L., and Beechem, T. E. *ACS Nano* **7**, 637–644 (2013).

[63] Tan, Z., Yin, J., Chen, C., Wang, H., Lin, L., Sun, L., Wu, J., Sun, X., Yang, H., Chen, Y., Peng, H., and Liu, Z. *ACS Nano* **10**, 6725–6730 (2016).

[64] Koren, E., Leven, I., Lörtscher, E., Knoll, A., Hod, O., and Duerig, U. *Nat. Nano.* **11**, 752 (2016).

[65] Li, S.-Y., Liu, K.-Q., Yin, L.-J., Wang, W.-X., Yan, W., Yang, X.-Q., Yang, J.-K., Liu, H., Jiang, H., and He, L. *Phys. Rev. B* **96**, 155416 (2017).

[66] Lopes dos Santos, J. M. B., Peres, N. M. R., and Castro Neto, A. H. *Phys. Rev. Lett.* **99**, 256802 (2007).

[67] Lopes dos Santos, J. M. B., Peres, N. M. R., and Castro Neto, A. H. *Phys. Rev. B* **86**, 155449 (2012).

[68] Mele, E. J. *Phys. Rev. B* **81**, 161405 (2010).

[69] Suárez Morell, E., Correa, J. D., Vargas, P., Pacheco, M., and Barticevic, Z. *Phys. Rev. B* **82**, 121407 (2010).

[70] Trambly de Laissardière, G., Mayou, D., and Magaud, L. *Nano Lett.* **10**, 804–808 (2010).

[71] Koshino, M. *New J. Phys.* **17**, 015014 (2015).

[72] Moon, P. and Koshino, M. *Phys. Rev. B* **87**, 205404 (2013).

[73] Bistritzer, R. and MacDonald, A. H. *PNAS* **108**, 12233–12237 (2011).

[74] Tang, M. S., Wang, C. Z., Chan, C. T., and Ho, K. M. *Phys. Rev. B* **53**, 979–982 (1996).

[75] Sboychakov, A. O., Rakhmanov, A. L., Rozhkov, A. V., and Nori, F. *Phys. Rev. B* **92**, 075402 (2015).

[76] Stauber, T., Low, T., and Gmez-Santos, G. (2018).

[77] Ahn, S. J., Moon, P., Kim, T.-H., Kim, H.-W., Shin, H.-C., Kim, E. H., Cha, H. W., Kahng, S.-J., Kim, P., Koshino, M., et al. *Science* **361**, 782–786 (2018).

[78] Kim, K., Yankowitz, M., Fallahazad, B., Kang, S., Movva, H. C. P., Huang, S., Larentis, S., Corbet, C. M., Taniguchi, T., Watanabe, K., Banerjee, S. K., LeRoy, B. J., and Tutuc, E. *Nano Lett.* **16**, 1989–1995 (2016). PMID: 26859527.

[79] Wang, H., Taychatanapat, T., Hsu, A., Watanabe, K., Taniguchi, T., Jarillo-Herrero, P., and Palacios, T. *IEEE Elec. Dev. Lett.* **32**, 1209–1211 (2011).

[80] Chen, J.-H., Jang, C., Xiao, S., Ishigami, M., and Fuhrer, M. S. *Nat. Nano.* **3**, 206 (2008).

[81] Aleiner, I. L. and Efetov, K. B. *Phys. Rev. Lett.* **97**, 236801 (2006).

[82] Landau, L. and Lifshitz, E. *Quantum Mechanics: Non-Relativistic Theory.* Course of Theoretical Physics. Elsevier Science, (1981).

[83] Ni, G. X., Wang, H., Wu, J. S., Fei, Z., Goldflam, M. D., Keilmann, F., Özyilmaz, B., Castro Neto, A. H., Xie, X. M., Fogler, M. M., and Basov, D. N. *Nat. Mater.* **14**, 1217 (2015).

[84] Lee, M., Wallbank, J. R., Gallagher, P., Watanabe, K., Taniguchi, T., Fal'ko, V. I., and Goldhaber-Gordon, D. *Science* **353**, 1526–1529 (2016).

[85] Moon, P. and Koshino, M. *Phys. Rev. B* **90**, 155406 (2014).

[86] Zólyomi, V., Drummond, N. D., and Fal'ko, V. I. *Phys. Rev. B* **89**, 205416 (2014).

[87] Giovannetti, G., Capone, M., van den Brink, J., and Ortix, C. *Phys. Rev. B* **91**, 121417 (2015).

[88] Gomes, K. K., Mar, W., Ko, W., Guinea, F., and Manoharan, H. C. *Nature* **483**, 306 (2012).

[89] Yang, W., Lu, X., Chen, G., Wu, S., Xie, G., Cheng, M., Wang, D., Yang, R., Shi, D., Watanabe, K., Taniguchi, T., Voisin, C., Plaçais, B., Zhang, Y., and Zhang, G. *Nano Lett.* **16**, 2387–2392 (2016).

[90] Chen, X., Wallbank, J., Patel, A. A., Mucha-Kruczyński, M., McCann, E., and Fal'ko, V. *Phys. Rev. B* **89**, 075401 (2014).

[91] Kindermann, M., Uchoa, B., and Miller, D. L. *Phys. Rev. B* **86**, 115415 (2012).

[92] Bednorz, J. G. and Muller, K. A. *Zeitschrift fur Physik B Condensed Matter* **64**, 189–193 (1986).

[93] Jorio, A. and Cançado, L. G. *Solid State Communications* **175-176**, 3–12 (2013).

[94] Ramnani, P., Neupane, M. R., Ge, S., Balandin, A. A., Lake, R. K., and Mulchandani, A. *Carbon* **123**, 302–306 (2017).

[95] Ferrari, A. C., Meyer, J. C., Scardaci, V., Casiraghi, C., Lazzeri, M., Mauri, F., Piscanec, S., Jiang, D., Novoselov, K. S., Roth, S., and Geim, A. K. *Phys. Rev. Lett.* **97**, 187401 (2006).

[96] Malard, L. M., Pimenta, M. A., Dresselhaus, G., and Dresselhaus, M. S. *Physics Reports* **473**, 51–87 (2009).

[97] Cardona, M. *Light Scattering in Solids I : Introductory Concepts*. Springer Berlin Heidelberg, Berlin, Heidelberg, (1983).

[98] Kashuba, O. and Fal'ko, V. I. *Phys. Rev. B* **80**, 241404 (2009).

[99] Mucha-Kruczyński, M., Kashuba, O., and Fal'ko, V. I. *Phys. Rev. B* **82**, 045405 (2010).

[100] García-Ruiz, A., Mucha-Kruczyński, M., and Fal'ko, V. I. *Phys. Rev. B* **97**, 155405 (2018).

[101] Riccardi, E., Kashuba, O., Cazayous, M., Méasson, M.-A., Sacuto, A., and Gallais, Y. *Phys. Rev. Materials* **3**, 014002 (2019).

[102] Ponosov, Y. S., Ushakov, A. V., and Streltsov, S. V. *Phys. Rev. B* **91**, 195435 (2015).

[103] Carozo, V., Almeida, C. M., Ferreira, E. H. M., Cançado, L. G., Achete, C. A., and Jorio, A. *Nano Lett.* **11**, 4527–4534 (2011).

[104] Yang, H., Liang, A., Chen, C., Zhang, C., Schroeter, N. B. M., and Chen, Y. *Nat. Rev. Mater.* **3**, 341–353 (2018).

[105] Dudin, P., Lacovig, P., Fava, C., Nicolini, E., Bianco, A., Cautero, G., and Barinov, A. *J. Synchrotron Rad.* **17**, 445–450 (2010).

[106] Avila, J., Razado-Colambo, I., Lorcy, S., Lagarde, B., Giorgetta, J.-L., Polack, F., and Asensio, M. C. *J. Phys.: Conf. Ser.* **425**, 192023 (2013).

[107] Einstein, A. *Annalen der Physik* **322**, 132–148 (1905).

[108] Zhou, S. Y., Gweon, G.-H., Fedorov, A. V., First, P. N., de Heer, W. A., Lee, D.-H., Guinea, F., Castro Neto, A. H., and Lanzara, A. *Nat. Mater.* **6**, 770 (2007).

[109] Sprinkle, M., Siegel, D., Hu, Y., Hicks, J., Tejeda, A., Taleb-Ibrahimi, A., Le Fèvre, P., Bertran, F., Vizzini, S., Enriquez, H., Chiang, S., Soukiassian,

P., Berger, C., de Heer, W. A., Lanzara, A., and Conrad, E. H. *Phys. Rev. Lett.* **103**, 226803 (2009).

[110] Ohta, T., Bostwick, A., Seyller, T., Horn, K., and Rotenberg, E. *Science* **313**, 951–954 (2006).

[111] Sediri, H., Pierucci, D., Hajlaoui, M., Henck, H., Patriarche, G., Dappe, Y. J., Yuan, S., Toury, B., Belkhou, R., Silly, M. G., Sirotti, F., Boutchich, M., and Ouerghi, A. *Scientific Reports* **5**, 16465 (2015).

[112] Razado-Colambo, I., Avila, J., Nys, J.-P., Chen, C., Wallart, X., Asensio, M.-C., and Vignaud, D. *Scientific Reports* **6**, 27261 (2016).

[113] Peng, H., Schrter, N. B. M., Yin, J., Wang, H., Chung, T.-F., Yang, H., Ekahana, S., Liu, Z., Jiang, J., Yang, L., Zhang, T., Chen, C., Ni, H., Barinov, A., Chen, Y. P., Liu, Z., Peng, H., and Chen, Y. *Advanced Materials* **29**, 1606741 (2017).

[114] Damascelli, A. *Physica Scripta* **2004**, 61 (2004).

[115] Williams, P. M. *Il Nuovo Cimento B (1971-1996)* **38**, 216–225 (1977).

[116] Mucha-Kruczyński, M., Tsyplyatyev, O., Grishin, A., McCann, E., Fal'ko, V. I., Bostwick, A., and Rotenberg, E. *Phys. Rev. B* **77**, 195403 (2008).

[117] Puschnig, P. and Lftner, D. *Journal of Electron Spectroscopy and Related Phenomena* **200**, 193 – 208 (2015). Special Anniversary Issue: Volume 200.

[118] Amorim, B. *Phys. Rev. B* **97**, 165414 (2018).

[119] Gierz, I., Henk, J., Höchst, H., Ast, C. R., and Kern, K. *Phys. Rev. B* **83**, 121408 (2011).

[120] Shirley, E. L., Terminello, L. J., Santoni, A., and Himpsel, F. J. *Phys. Rev. B* **51**, 13614–13622 (1995).

[121] Bostwick, A., Ohta, T., Seyller, T., Horn, K., and Rotenberg, E. *Nat. Phys.* **3**, 36 (2006).

[122] Calandra, M. and Mauri, F. *Phys. Rev. B* **76**, 205411 (2007).

[123] Koshino, M. and McCann, E. *Phys. Rev. B* **80**, 165409 (2009).

[124] Koshino, M. and McCann, E. *Phys. Rev. B* **79**, 125443 (2009).

[125] Slater, J. C. and Koster, G. F. *Phys. Rev.* **94**, 1498–1524 (1954).

[126] Giovannetti, G., Khomyakov, P. A., Brocks, G., Karpan, V. M., van den Brink, J., and Kelly, P. J. *Phys. Rev. Lett.* **101**, 026803 (2008).

[127] Esaki, L. *Phys. Rev.* **109**, 603–604 (1958).

[128] Hines, M. *IEEE Transactions on Electron Devices* **17**(1), 1–8 (1970).

[129] Van Degrift, C. T. *Review of Scientific Instruments* **46**(5), 599–607 (1975).

[130] Britnell, L., Gorbachev, R. V., Geim, A. K., Ponomarenko, L. A., Mishchenko, A., Greenaway, M. T., Fromhold, T. M., Novoselov, K. S., and Eaves, L. *Nat. Comm.* **4**, 1794 (2013).

[131] Mishchenko, A., Tu, J. S., Cao, Y., Gorbachev, R. V., Wallbank, J. R., Greenaway, M. T., Morozov, V. E., Morozov, S. V., Zhu, M. J., Wong, S. L., Withers, F., Woods, C. R., Kim, Y.-J., Watanabe, K., Taniguchi, T., Vdovin, E. E., Makarovsky, O., Fromhold, T. M., Fal'ko, V. I., Geim, A. K., Eaves, L., and Novoselov, K. S. *Nat. Nano.* **9**, 808 (2014).

[132] Fallahazad, B., Lee, K., Kang, S., Xue, J., Larentis, S., Corbet, C., Kim, K., Movva, H. C. P., Taniguchi, T., Watanabe, K., Register, L. F., Banerjee, S. K., and Tutuc, E. *Nano Lett.* **15**, 428–433 (2015).

[133] Kang, S., Fallahazad, B., Lee, K., Movva, H., Kim, K., Corbet, C. M., Taniguchi, T., Watanabe, K., Colombo, L., Register, L. F., Tutuc, E., and Banerjee, S. K. *IEEE Elec. Dev. Lett.* **36**, 405–407 (2015).

[134] Wallbank, J. R., Ghazaryan, D., Misra, A., Cao, Y., Tu, J. S., Piot, B. A., Potemski, M., Pezzini, S., Wiedmann, S., Zeitler, U., Lane, T. L. M., Morozov, S. V., Greenaway, M. T., Eaves, L., Geim, A. K., Fal'ko, V. I., Novoselov, K. S., and Mishchenko, A. *Science* **353**, 575 (2016).

[135] Haigh, S. J., Gholinia, A., Jalil, R., Romani, S., Britnell, L., Elias, D. C., Novoselov, K. S., Ponomarenko, L. A., Geim, A. K., and Gorbachev, R. *Nat. Mater.* **11**, 764 (2012).

[136] Roy, T., Liu, L., de la Barrera, S., Chakrabarti, B., Hesabi, Z. R., Joiner, C. A., Feenstra, R. M., Gu, G., and Vogel, E. M. *Appl. Phys. Lett.* **104**, 123506 (2014).

[137] Hwan Lee, S., Sup Choi, M., Lee, J., Ho Ra, C., Liu, X., Hwang, E., Hee Choi, J., Zhong, J., Chen, W., and Jong Yoo, W. *Appl. Phys. Lett.* **104**, 053103 (2014).

[138] Shi, Z., Jin, C., Yang, W., Ju, L., Horng, J., Lu, X., Bechtel, H. A., Martin, M. C., Fu, D., Wu, J., Watanabe, K., Taniguchi, T., Zhang, Y., Bai, X., Wang, E., Zhang, G., and Wang, F. *Nat. Phys.* **10**, 743 (2014).

[139] Kim, Y., Herlinger, P., Moon, P., Koshino, M., Taniguchi, T., Watanabe, K., and Smet, J. H. *Nano Lett.* **16**, 5053–5059 (2016).

[140] Pierucci, D., Henck, H., Avila, J., Balan, A., Naylor, C. H., Patriarche, G., Dappe, Y. J., Silly, M. G., Sirotti, F., Johnson, A. T. C., Asensio, M. C., and Ouerghi, A. *Nano Lett.* **16**, 4054–4061 (2016).

[141] Trixler, F. *Current Organic Chemistry* **17**, 1758–1770 (2013).

[142] Binnig, G., Rohrer, H., Gerber, C., and Weibel, E. *Phys. Rev. Lett.* **49**, 57–61 (1982).

[143] Britnell, L., Gorbachev, R. V., Jalil, R., Belle, B. D., Schedin, F., Mishchenko, A., Georgiou, T., Katsnelson, M. I., Eaves, L., Morozov, S. V., Peres, N. M. R., Leist, J., Geim, A. K., Novoselov, K. S., and Ponomarenko, L. A. *Science* **335**, 947 (2012).

[144] Greenaway, M. . T., Vdovin, E. . E., Mishchenko, A., Makarovsky, O., Patanè, A., Wallbank, J. . R., Cao, Y., Kretinin, A. . V., Zhu, M. . J., Morozov, S. . V., Fal'ko, V. . I., Novoselov, K. . S., Geim, A. . K., Fromhold, T. . M., and Eaves, L. *Nat. Phys.* **11**, 1057 (2015).

[145] Bardeen, J. *Phys. Rev. Lett.* **6**, 57–59 (1961).

[146] Simmons, J. G. *J. Appl. Phys.* **34**, 1793–1803 (1963).

[147] Li, M. O., Esseni, D., Snider, G., Jena, D., and Grace Xing, H. *J. Appl. Phys.* **115**, 074508 (2014).

[148] Feenstra, R. M., Jena, D., and Gu, G. *J. Appl. Phys.* **111**, 043711 (2012).

[149] Moffatt, P. and Kim, E. H. *Appl. Phys. Lett.* **89**, 192117 (2006).

[150] Britnell, L., Gorbachev, R. V., Jalil, R., Belle, B. D., Schedin, F., Katsnelson, M. I., Eaves, L., Morozov, S. V., Mayorov, A. S., Peres, N. M. R., Castro Neto, A. H., Leist, J., Geim, A. K., Ponomarenko, L. A., and Novoselov, K. S. *Nano Lett.* **12**, 1707–1710 (2012).

[151] Xu, Y.-N. and Ching, W. Y. *Phys. Rev. B* **44**, 7787–7798 (1991).

[152] Georgiou, T., Jalil, R., Belle, B. D., Britnell, L., Gorbachev, R. V., Morozov, S. V., Kim, Y.-J., Gholinia, A., Haigh, S. J., Makarovsky, O., Eaves, L., Ponomarenko, L. A., Geim, A. K., Novoselov, K. S., and Mishchenko, A. *Nat. Nano.* **8**, 100 (2012).

[153] Mucha-Kruczyński, M., Wallbank, J. R., and Fal'ko, V. I. *Phys. Rev. B* **93**, 085409 (2016).

[154] Brown, E., Söderström, J., Parker, C., Mahoney, L., Molvar, K., and McGill, T. *Applied Physics Letters* **58**(20), 2291–2293 (1991).

[155] Sun, Z. Z., Wang, X., Zhang, R., and Lee, S. T. *Journal of Applied Physics* **103**(10), 103719 (2008).

[156] Wong, D., Wang, Y., Jung, J., Pezzini, S., DaSilva, A. M., Tsai, H.-Z., Jung, H. S., Khajeh, R., Kim, Y., Lee, J., Kahn, S., Tollabimazraehno, S., Rasool, H., Watanabe, K., Taniguchi, T., Zettl, A., Adam, S., MacDonald, A. H., and Crommie, M. F. *Phys. Rev. B* **92**, 155409 (2015).

[157] Tong, Q., Yu, H., Zhu, Q., Wang, Y., Xu, X., and Yao, W. *Nat. Phys.* **13**, 356 (2016).

[158] Zhang, C., Chuu, C.-P., Ren, X., Li, M.-Y., Li, L.-J., Jin, C., Chou, M.-Y., and Shih, C.-K. *Science Advances* (2017).

[159] Pan, Y., Fölsch, S., Nie, Y., Waters, D., Lin, Y.-C., Jariwala, B., Zhang, K., Cho, K., Robinson, J. A., and Feenstra, R. M. *Nano Lett.* **18**, 1849–1855 (2018).

[160] Forsythe, C., Zhou, X., Watanabe, K., Taniguchi, T., Pasupathy, A., Moon, P., Koshino, M., Kim, P., and Dean, C. R. *Nat. Nano.* **13**, 566–571 (2018).

[161] Baibich, M. N., Broto, J. M., Fert, A., Van Dau, F. N., Petroff, F., Etienne, P., Creuzet, G., Friederich, A., and Chazelas, J. *Phys. Rev. Lett.* **61**, 2472–2475 (1988).

[162] Žutić, I., Fabian, J., and Das Sarma, S. *Rev. Mod. Phys.* **76**, 323–410 (2004).

[163] Schaibley, J. R., Yu, H., Clark, G., Rivera, P., Ross, J. S., Seyler, K. L., Yao, W., and Xu, X. *Nat. Rev. Mater.* **1**, 16055 (2016).

[164] Lane, T. L. M., Wallbank, J. R., and Fal'ko, V. I. *Appl. Phys. Lett.* **107**, 203506 (2015).

[165] Vdovin, E. E., Mishchenko, A., Greenaway, M. T., Zhu, M. J., Ghazaryan, D., Misra, A., Cao, Y., Morozov, S. V., Makarovsky, O., Fromhold, T. M., Patanè, A., Slotman, G. J., Katsnelson, M. I., Geim, A. K., Novoselov, K. S., and Eaves, L. *Phys. Rev. Lett.* **116**, 186603 (2016).

[166] Ghazaryan, D., Greenaway, M. T., Wang, Z., Guarochico-Moreira, V. H., Vera-Marun, I. J., Yin, J., Liao, Y., Morozov, S. V., Kristanovski, O., Lichtenstein, A. I., Katsnelson, M. I., Withers, F., Mishchenko, A., Eaves, L., Geim, A. K., Novoselov, K. S., and Misra, A. *Nat. Elec.* **1**, 344–349 (2018).

[167] Chandni, U., Watanabe, K., Taniguchi, T., and Eisenstein, J. P. *Nano Lett.* **15**, 7329–7333 (2015).

[168] Chandni, U., Watanabe, K., Taniguchi, T., and Eisenstein, J. P. *Nano Lett.* **16**, 7982–7987 (2016).

[169] Rycerz, A., Tworzydlo, J., and Beenakker, C. W. J. *Nat. Phys.* **3**, 172 (2007).

[170] Van't Erve, O., Friedman, A., Cobas, E., Li, C., Robinson, J., and Jonker, B. *Nat. Nano.* **7**, 737 (2012).

[171] Friedman, A. L., vant Erve, O. M., Li, C. H., Robinson, J. T., and Jonker, B. T. *Nat. Comm.* **5**, 3161 (2014).

[172] Friedman, A. L., van t Erve, O. M., Robinson, J. T., Whitener Jr, K. E., and Jonker, B. T. *AIP Advances* **6**, 056301 (2016).

[173] Kuroda, M. A., Tersoff, J., Newns, D. M., and Martyna, G. J. *Nano Lett.* **11**, 3629–3633 (2011).

[174] Zhong, X., Amorim, R. G., Rocha, A. R., and Pandey, R. *Nanotechnology* **25**, 345703 (2014).

[175] Mucha-Kruczynski, M., Abergel, D. S. L., McCann, E., and Fal'ko, V. I. *J. Phys.: Con. Matt.* **21**, 344206 (2009).

[176] Taychatanapat, T., Watanabe, K., Taniguchi, T., and Jarillo-Herrero, P. *Nat. Phys.* **7**, 621 (2011).

[177] Funk, H., Knorr, A., Wendler, F., and Malic, E. *Phys. Rev. B* **92**, 205428 (2015).

[178] Nogaret, A. *J. Phys.: Con. Matt.* **22**, 253201 (2010).

[179] Hipolito, F. and Pereira, V. M. *2D Mater.* **4**, 021027 (2017).